Dislocations and nanomechanics in Alumina using atomistic simulations

Qinqin Xu

N°d'ordre NNT : 2021LYSEI091

THESE de DOCTORAT DE L'UNIVERSITE DE LYON
opérée au sein de
L'Institut National des Sciences Appliquées de Lyon

Ecole Doctorale N° ED 34
Matériaux de Lyon

Spécialité de doctorat : Science des Matériaux

Soutenue publiquement le 14/12/2021, par :
Xu Qinqin

Dislocations and nanomechanics in Alumina using atomistic simulations

---

Devant le jury composé de :

Laurent Pizzagalli	Directeur de Recherche CNRS	Univ. Poitiers	Rapporteur
Philippe Carrez	Professeur	Univ. Lille	Rapporteur
Karine Masenelli-Varlot	Professeur	INSA-Lyon	Examinateur
Marie-Ingrid Richard	Ingénieur-chercheur	CEA Grenoble	Examinateur
Tristan Albaret	Maître de conférences	Univ. Lyon	Invité
Jérome Chevalier	Professeur	INSA-Lyon	Directeur de thèse
Jonathan Amodeo	Chargé de Recherche CNRS	INSA-Lyon	Co-directeur de thèse

Département FEDORA – INSA Lyon - Ecoles Doctorales – Quinquennal 2016-2020

SIGLE	ECOLE DOCTORALE	NOM ET COORDONNEES DU RESPONSABLE
CHIMIE	**CHIMIE DE LYON** http://www.edchimie-lyon.fr Sec. : Renée EL MELHEM Bât. Blaise PASCAL, 3e étage secretariat@edchimie-lyon.fr INSA : R. GOURDON	**M. Stéphane DANIELE** Institut de recherches sur la catalyse et l'environnement de Lyon IRCELYON-UMR 5256 Équipe CDFA 2 Avenue Albert EINSTEIN 69 626 Villeurbanne CEDEX directeur@edchimie-lyon.fr
E.E.A.	**ÉLECTRONIQUE, ÉLECTROTECHNIQUE, AUTOMATIQUE** http://edeea.ec-lyon.fr Sec. : M.C. HAVGOUDOUKIAN ecole-doctorale.eea@ec-lyon.fr	**M. Gérard SCORLETTI** École Centrale de Lyon 36 Avenue Guy DE COLLONGUE 69 134 Écully Tél : 04.72.18.60.97 Fax 04.78.43.37.17 gerard.scorletti@ec-lyon.fr
E2M2	**ÉVOLUTION, ÉCOSYSTÈME, MICROBIOLOGIE, MODÉLISATION** http://e2m2.universite-lyon.fr Sec. : Sylvie ROBERJOT Bât. Atrium, UCB Lyon 1 Tél : 04.72.44.83.62 INSA : H. CHARLES secretariat.e2m2@univ-lyon1.fr	**M. Philippe NORMAND** UMR 5557 Lab. d'Ecologie Microbienne Université Claude Bernard Lyon 1 Bâtiment Mendel 43, boulevard du 11 Novembre 1918 69 622 Villeurbanne CEDEX philippe.normand@univ-lyon1.fr
EDISS	**INTERDISCIPLINAIRE SCIENCES-SANTÉ** http://www.ediss-lyon.fr Sec. : Sylvie ROBERJOT Bât. Atrium, UCB Lyon 1 Tél : 04.72.44.83.62 INSA : M. LAGARDE secretariat.ediss@univ-lyon1.fr	**Mme Sylvie RICARD-BLUM** Institut de Chimie et Biochimie Moléculaires et Supramoléculaires (ICBMS) - UMR 5246 CNRS - Université Lyon 1 Bâtiment Curien - 3ème étage Nord 43 Boulevard du 11 novembre 1918 69622 Villeurbanne Cedex Tel : +33(0)4 72 44 82 32 sylvie.ricard-blum@univ-lyon1.fr
INFOMATHS	**INFORMATIQUE ET MATHÉMATIQUES** http://edinfomaths.universite-lyon.fr Sec. : Renée EL MELHEM Bât. Blaise PASCAL, 3e étage Tél : 04.72.43.80.46 infomaths@univ-lyon1.fr	**M. Hamamache KHEDDOUCI** Bât. Nautibus 43, Boulevard du 11 novembre 1918 69 622 Villeurbanne Cedex France Tel : 04.72.44.83.69 hamamache.kheddouci@univ-lyon1.fr
Matériaux	**MATÉRIAUX DE LYON** http://ed34.universite-lyon.fr Sec. : Stéphanie CAUVIN Tél : 04.72.43.71.70 Bât. Direction ed.materiaux@insa-lyon.fr	**M. Jean-Yves BUFFIÈRE** INSA de Lyon MATEIS - Bât. Saint-Exupéry 7 Avenue Jean CAPELLE 69 621 Villeurbanne CEDEX Tél : 04.72.43.71.70 Fax : 04.72.43.85.28 jean-yves.buffiere@insa-lyon.fr
MEGA	**MÉCANIQUE, ÉNERGÉTIQUE, GÉNIE CIVIL, ACOUSTIQUE** http://edmega.universite-lyon.fr Sec. : Stéphanie CAUVIN Tél : 04.72.43.71.70 Bât. Direction mega@insa-lyon.fr	**M. Jocelyn BONJOUR** INSA de Lyon Laboratoire CETHIL Bâtiment Sadi-Carnot 9, rue de la Physique 69 621 Villeurbanne CEDEX jocelyn.bonjour@insa-lyon.fr
ScSo	**ScSo*** http://ed483.univ-lyon2.fr Sec. : Véronique GUICHARD INSA : J.Y. TOUSSAINT Tél : 04.78.69.72.76 veronique.cervantes@univ-lyon2.fr	**M. Christian MONTES** Université Lyon 2 86 Rue Pasteur 69 365 Lyon CEDEX 07 christian.montes@univ-lyon2.fr

*ScSo : Histoire, Géographie, Aménagement, Urbanisme, Archéologie, Science politique, Sociologie, Anthropologie

Acknowledgement

First of all, I would like to thank Dr. Laurent Pizzagalli and Pr. Philippe Carrez who reviewed my thesis manuscript as well as acknowledge all the members of my PhD jury for their helpful advices.

Then, my deepest gratitude goes first and foremost to Dr. Jonathan Amodeo and Pr. Jérome Chevalier, my supervisors, for their constant encouragement and guidance. They got me through all the stages of the thesis especially for simulations and writing. Without their consistent and illuminating instruction, this thesis could not have reached its present form. During the whole PhD project, they made great efforts to help me to conduct and conclude the numerical studies and lead me into the world of ceramic material. I greatly appreciate them for all the help they gave to me.

I am also greatly obliged to all the professors, teachers and colleagues at the MATEIS laboratory. In particular, I would like to thank Pr. Eric Maire, Pr. Michel Perez, Dr. Zai Zengqiang, Dr. Marion Coffigniez, Dr. Lucile Magnier, Dr. Arnaud Junet, Dr. Quentin Saby, Javier-Antonio Gonzalez Joa, Marion Borde and Xiao Ce,who have instructed and helped me a lot in the past four years.

Thanks to my beloved girlfriend Dr. Zhong Li and our respective families for their loving considerations and great confidence. I also owe the more sincere gratitude to my friends who gave me their help during my time in France.

Finally, I would like to acknowledge the the Chinese Scholarship Council (CSC) who gave the opportunity to conduct this project.

Abstract

The study of nano-objects is of particular interest due to their outstanding mechanical properties. While metal nanocrystals are generally characterized by high yield strength and ductility under extreme compressive stress, very few is known about other classes of materials including ceramic or semi-conductors. Recently, it was shown that ceramic nanoparticles such as aluminum or magnesium oxides could plastically deform under high stress without cracking what might have significant implications for the sintering and compaction of nanocrystalline ceramics. However, only few evidences of the elementary deformation processes were addressed so far, especially in the case of α-Al_2O_3 nanocrystals.
In this study, we propose to investigate α-Al_2O_3 nanoparticle mechanics using molecular dynamics simulations. Firstly, several α-Al_2O_3 bulk properties as lattice and elastic constants, stacking-fault and surface energies as well as basal edge dislocation features as compared to existing experimental/numerical literature are investigated to test the transferability of various interatomic force fields to the nanomechanical field. Among all the tested parameterizations, the 2/3-body Vashishta interatomic potential has shown to be particularly adapted to the overall study. Secondly, nanoparticle compression tests are modeled as function of orientation and temperature including a detailed analysis of dislocation-based mechanisms for several sizes of α-Al_2O_3 nanoparticles. Results are discussed in the context of recent nanomechanics experiments as well as pioneer works performed on bulk alumina.

Résumé en français

Les nano-objets sont particulièrement intéressants pour leurs excellentes propriétés mécaniques. Alors que les nanocristaux métalliques sont généralement caractérisés par une limite d'élasticité accrue, une contrainte à la rupture augmentée tout comme par un accroissement global de leur ductilité en compression, très peu de choses sont connues pour les autres classes de matériaux comme les céramiques ou semi-conducteurs. Il a récemment été montré que des nanoparticules d'oxides de magnesium et d'aluminium pouvaient être déformées plastiquement à forte contrainte sans signe de rupture ce qui pourrait avoir des implications importantes dans le domaine de l'élaboration des matériaux céramiques (notamment lors de leur compaction). Néanmoins, les mécanismes de déformation ont été très peu caractérisés dans ces nanoparticules, notamment dans le cas des nanocristaux d'Al_2O_3.

Dans cette étude, nous proposons d'étudier les propriétés mécaniques et les mécanismes de déformation de nanoparticules d'alumine α par dynamique moléculaire. Tout d'abord, plusieurs propriétés du matériau massif sont calculées, étudiées et comparées à la littérature existante. Entre autres, les paramètres de maille, constantes élastiques, énergies de faute d'empilement et de surface ainsi que les caractéristiques de la dislocation coin dans le système de glissement basal sont simulés afin d'étudier la transférabilité de plusieurs formalismes à l'échelle atomique. Parmi les potentiels testés, le potentiel à trois corps de Vashishta a montré les meilleures aptitudes pour les applications visées dans la suite de l'étude. Ensuite, nous avons simulé en dynamique moléculaire des tests de compression sur des nanoparticules d'alumine en fonction de l'orientation de la sollication et de la température. Une analyse détaillée du comportement mécanique et des mécanismes de déformation a été réalisée pour plusieurs tailles de nanoparticules. Les résultats sont discutés au regard d'expériences de nanomécaniques récentes et de travaux pionniers réalisés dans l'alumine massive.

List of acronyms and abbreviations

a Prismatic *a*
AANT Anodic Alumina Nanotube
ATOMSK Atom/Molecule/Material Software Kit
BC Boundary Condition
BDT Brittle-to-Ductile Transition
c Basal
CA Compression Axis
CG Conjugate Gradient
DFT Density-Functional Theory
DXA Dislocation Extraction Algorithm
EAM Embedded Atom Model
ETM Electron Transport Material
FCC Face-Centered-Cubic
FEM Finite-Element Method
FIRE Fast Inertial Relaxation Engine
GB Grain Boundary
GSFE Generalised Stacking Fault Energy
GULP General Utility Lattice Program
HCP Hexagonal Close Packed
HFTN Hessian-Free Truncated Newton
HRTEM High-Resolution Transmission Electron Microscope
HT High Temperature
LAMMPS Large-scale Atomic/Molecular Massively Parallel Simulator
LT Low Temperature
m Prismatic *m*
MD Molecular Dynamics
MS Molecular Statics
MSM Multi-level Summation Method
n Pyramidal *n*
NAA Nanoporous Anodic Alumina
NP Nanoparticle
OVITO Open Visualization Tool
PBC Periodic Boundary Condition
R Rhombohedral
RDF Radial Distribution Function
RI Rigid Ion
RT Room Temperature
s Pyramidal *s*
SEM Scanning Electron Microscope
SFE Stacking Fault Energy
SMTB-Q Second-Moment Tight-Binding Qeq
sSFE Stable Stacking Fault Energy
T Temperature
TB Twin Boundary
TEM Transmission Electron Microscope
uSFE Unstable Stacking Fault Energy
v Pyramidal *v*
w Pyramidal *w*
Y-TZP Yttria Tetragonal Zirconia Polycrystal

Table of contents

Introduction

Micro- and nano-objects as pillars, wires, thin films and particles have recently drawn an intensive scientific attention due to their outstanding mechanical properties. They generally show very high yield strength and enhanced ductility when compared to their massive counterpart as well as a lack of failure when deformed under extreme compression at the nanoscale. While these size effects were widely studied in metals, few recent studies show that these original properties could also apply to other material families as ceramics, intermetallics or semi-conductors. In the case of nanoceramics, this would imply a real technological push forward in terms of processing capabilities and on-use mechanical properties. It was shown for example that ceramic nanopowders exhibit a Brittle-to-Ductile Transition (BDT) opening new doors for their process by plastic forming or for their use with a significant amount of plasticity reached before failure [CAL 12, ISS 15, ISS 18, ISS 21]. Such properties may have implications in several fields as *e.g.,* in modern surgery where the use of ceramics as biocompatible alternatives to metallic alloys continuously increases.

In addition to its main role as the most important aluminum precursor, α-alumina (α-Al_2O_3) is one of the top-known technical ceramics currently used for its excellent mechanical properties in various fields of applications such as abrasives [WAN 00b, NIE 02], catalysis [KNÖ 78, MAN 02] and medical engineering [WEB 00, CHE 09]. Since the pioneer work of Boutin, alumina is one of the main materials used for hip replacement due to its high bio-compatibility [BOU 77, HUL 93, NEV 01]. It is also commonly used for dental brackets and crowns [DEN 10, ALS 14]. However, its modest toughness generally enforces alumina compounds to be thick in order to satisfy the strength levels required. It is therefore often replaced by tougher ceramics as zirconia, or used as the matrix in a composite with reinforcing (zirconia) particles (*e.g.* zirconia-toughened alumina).
Various strategies are adopted to improve the mechanical properties of alumina-based materials. Al_2O_3 is now regularly combined to other metal oxides such as zirconia (ZrO_2), ceria (CeO_2) or titania (TiO_2) to build alloys and composites with significantly improved mechanical properties [GRE 82, TUA 02, YIL 07, CHE 09, HE 14, VER 17]. In particular, a significant attention has to be paid to refine the powder size toward the nanoscale and target alumina-based submicron ceramics [SHA 09]. Along that line and to improve the understanding of alumina mechanical properties at the nanoscale, Calvie *et*

al. performed *in situ* nanocompression tests of alumina NanoParticles (NPs) inside the Transmission Electron Microscope (TEM) [CAL 12, CAL 14]. In particular, the authors emphasize the unprecedented ductility reached by the individual alumina nanocrystals although they do not conclude about the elementary mechanisms responsible for such critical behaviour. Indeed, while reducing the size of single-crystalline ceramics deep in the sub-micron scale is known to promote the BDT and postpone (or inhibit) the fracture process [KOR 11a, KOR 11b, CAL 14, DU 15, ISS 15, AMO 18, ISS 21]. There are still questions about the plastic deformation mechanisms at the origin of such behaviour especially in the case of α-alumina.

To address such question at the atomic scale, Molecular Dynamics (MD) simulations are regularly used to supplement experimental studies at small-scales. In particular, these simulations are currently applied to investigate the deformation processes of single- and nanocrystalline structures [MOR 18, AMO 21].
Sarobol *et al.* have investigated the plasticity of defective and defect-scarce alumina small-scale particles using Room Temperature (RT) *in situ* compression tests within the TEM and MD simulations [SAR 16]. For single-crystalline NPs with Compression Axis (CA) along [0001], the authors have shown that plasticity was accommodated by the nucleation of dislocation within the rhombohedral slip system from the contact area between the indenter and the sample. Zhang *et al.* have studied the deformation mechanisms of α-alumina thin films using impact loading MD simulations [ZHA 08]. Analysis of inner impact faces show wild deformation patterns (just below the impact) with dislocations nucleation events induced by local stress concentration. Various slip systems and deformation processes typical of the Hexagonal Close Packed (HCP) crystalline structure were identified including pyramidal slip, prismatic slip, basal slip and twins as well as rhombohedral twining. A similarly complex plastic behaviour is emphasized by Nishimura *et al.* using nanoindentation MD simulations [NIS 08].
Overall, the elementary deformation processes believed to be responsible of nanoscale α-alumina deformation seem more extensive than those of the classical picture inferred from High-Temperature (HT) nanoindentation of polycrystalline alumina in which mostly basal, prismatic and rohmbohedral slip were characterized [CAS 81a, BIL 96, HEU 10]. However, conclusions have to be drawn with care when exclusively derived from MD simulations as those are known to be particularly dependent on the interatomic potential used. Indeed, interatomic potentials are at the roots of atomistic simulations *i.e.*, they integrate all the theoretical background and the physical hypothesis made to compute the energy and derive the interatomic forces of the investigated system. For each class of materials, specific frameworks either derived from the quantum theory or from more classical theories were developed to better reflect the physics of the atomic bond with more or less complexity. For example in metal oxides, one of the simplest and most used interatomic model is the Rigid Ion (RI) model [LEW 85]. The RI formulation assumes non-deformable ions

with fixed charges modelled by short range and coulombic interactions. This approach was first extended to the shell model in which the ion nucleus and the electron cloud are considered as two different entities bonded by an harmonic spring [DIC 58, MIT 93] and then to the breathing-shell model in which the electron shell is allowed to change shape [SCH 66]. These extended versions of the model allows to compute polarizability and improve lattice vibration calculations when compared to the RI original model. An other theoretical framework developed to model metal oxides is the 2/3-body potentials as developed by Vashishta *et al.* [VAS 90, VAS 07, BRA 09]. These potentials are inspired by the Stillinger-Weber formalism originally developed to model covalent materials as silicon [STI 85, VIN 01]. Indeed, the ionic *vs.* covalent ambivalence of the atomic bond in oxides is traduced in the MD literature by a competition between ionic RI and covalent Stillinger-Weber like potentials. Nevertheless, while these methods allow for large-scale simulations they sometimes suffer from their intrinsic simplicity what have led to the development of more complex formulation including variable charge models as COMB3 [SHA 10, LIA 14], ReaxFF [VAN 01a] or Second-Moment Tight-Binding Qeq (SMTB-Q) [SAL 16].

Most of the aforementioned formalisms were also derived for α-Al_2O_3 properties. In this study, after a reminder about the interatomic potential theoretical frameworks, we present an exhaustive set of tests and compare the transferability of RI, 2/3-body and variable charge potentials applied to α-Al_2O_3 material properties calculation. A special attention is paid to material properties important to be transferred in anticipation of modeling nanomechanical tests. This includes not only lattice properties but also surface and stacking-faut energies as well as dislocation properties. The pros and cons of each potential are discussed all along the study shading light on the best compromise to do to model nanomechanical tests.
Do we already have in the literature a physical model of α-Al_2O_2 precise enough to model NPs compression tests? Can we simulate α-Al_2O_2 NPs deform plastically under compression? If yes, what are the elementary deformation processes that govern plastic deformation? Do they change with temperature or orientation? Can the MD simulation of α-Al_2O_2 NPs compression test be used to interpret experiments?

Try to answer these questions, this Ph.D thesis is presented as follows. The starting chapter presents first a literature review of most-common ceramic materials and their applications. It is then followed by an introduction to mechanical properties at the nanoscale. This chapter ends with an introduction to alumina for which applications, lattice and deformation properties are presented. The second chapter focuses on atomistic simulations and interatomic potentials. First, an introduction about the atomic-scale methods used during the thesis is presented in the framework of the Large-scale Atomic/Molecular Massively Parallel Simulator (LAMMPS) code. Then, a detailed description of the interatomic potential we used is provided. Finally, simulation companion

tools as the Atom/Molecule/Material Software Kit (ATOMSK) and the Open Visualization Tool (OVITO) are presented. In the third chapter, we present an exhaustive set of calculations of various materials properties applied to α-Al_2O_3 using several interatomic potentials (RI, 2/3-body and SMTB-Q). The transferability of each potential to α-alumina nanomechanics is discussed in this chapter. The fourth chapter focuses on the *in silico* methods used or developed to build α-Al_2O_3 NPs. It also includes a detailed characterization of the samples later compressed in the Chapter V. Indeed, the fifth chapter presents nanocompression tests performed on α-Al_2O_3 NPs of various sizes. The mechanical behaviour of α-Al_2O_3 NPs as function of temperature and orientation is discussed and a detailed analysis of the plastic deformation processes is provided. These results are discussed and compared to experiments and simulations published in the literature at the end of the chapter. Finally, this manuscript ends with a general conclusion.

Chapter 1

Literature review

Ceramics are used in various fields of applications such as biomedical engineering, catalyst or electronics. In this chapter, we first propose a literature review about ceramic materials with a special focus on structural ceramics. We introduce main structural ceramics altogether with their related applications. Then, the pros and cons of small-scale ceramics will be addressed to head to a final subsection about alumina.

1.1 Ceramic materials and their applications

1.1.1 Ceramics for biomedical technologies

Ceramics are used for various biomedical engineering applications such as femoral heads and acetabular cups for total hip replacement, dental implants and restorations as well as bone fillers and scaffolds for tissue engineering [CHE 06]. Alumina- or zirconia-based ceramics as well as their composites are the most used biomedical ceramics for structural applications. They exhibit particularly interesting mechanical properties including high strength and toughness. In the 1970s, Garvie *et al.* were the first to describe the transformation toughening process in zirconia ceramics [ARE 19]. This now well-known process relies on the transformation at crack tips of metastable tetragonal crystallites into the monoclinic phase that is accompanied by a volumetric expansion and compressive stresses that impede crack propagation [CHE 09]. The use of zirconia has opened the way towards new implant designs that were not accessible with alumina which is known to be more brittle [CHE 07]. The combination of the several ceramic constituents can improve these mechanical properties. For example, Yttria-stabilized Tetragonal Zirconia Polycrystal (Y-TZP) ceramics can be used to make alumina matrix tougher. Y-TZP exhibits a strength of more than 1 GPa with a toughness of about 5–10 MPa.m$^{1/2}$. For comparison, pure alumina has a strength of $\sim$0.45 GPa and a toughness 4.6$\pm$0.3 MPa.m$^{1/2}$ [GUA 04, CHE 06, CHE 07]. Recently, new ultrafine ceramic composites were made out

of alumina and zirconia nanopowders [DAL 12]. These new ceramic composites target to improve the reliability and the mechanical properties of ceramic alloys, especially in the field of orthopaedic applications [ROU 10, NAG 13].

Silicon nitrides and carbides belong to an other category of ceramic materials highly considered for biomedical applications due to their high toughness and strength together with their good biocompatibility and wear resistance [MIT 95]. When compared to alumina and zirconia, silicon-based ceramics are less influenced by slow crack growth what improves the reliability of structural pieces that are generally characterized by a lower risk of delayed failure. Nevertheless, non-oxide ceramics require more processing and machining efforts. They might benefit of more applications in the future if combined with the development and progressive generalization of modern processing techniques such as nanopowder fast sintering routes [LUK 17, TON 20].

Calcium phosphate ceramics and bioactive glasses are also used when an healthy interaction with the human body is required (*e.g.* bone in-growth). Calcium phosphates nevertheless exhibit lower strengths than other aforementioned ceramics. The bone-bonding calcia phospohate silicate glass-ceramics were first proposed by Hench *et al.* in 1971 [HEN 71]. Scaffolds can be processed using submicron powder sintering with a final grain size about 1 µm [KAL 07]. Nano-structured calcium phosphate ceramics exhibit better fracture toughness and bioactivity than coarse crystals. Due to their ability to induce osteoblastic differentiation in progenitor cells, calcium phosphate ceramics are mostly used for bone tissue regeneration applications [SAM 13].

1.1.2 Ceramics for catalysts, automotive and electronic applications

Ceramics such as Al_2O_3, CaO and Si_3N_4 are used for catalysts as well as support materials (substrates) to anchor or disperse a variety of active metals [KEA 03]. Catalytic applications can be categorized among zeolite-based catalysts, catalytic converters and solid oxide fuel cells [ZHU 18].
Zeolites represent a commercially important branch of advanced catalysts ceramics. Aluminosilicate zeolithes are characterized by channels and cavities of molecular dimensions and their atomic structure is made of oxygen tetrahedrons supported by Si or Al atoms [VAS 20]. Synthesized zeolites are widely used in the chemical industry. They are able to absorb molecules due to their microstructure made of void spaces with high internal surface area. Due to their high size/sieving property, zeolites are often used for separation applications [ZHU 18].
Modern catalytic converters consist of either a ceramic honeycomb monolithic structure or ceramic beads coated with precious metals (Pt, Pd and Rh) [MUR 20]. Among them,

porous alumina ceramics are employed as catalysis support due to their high-surface area while zirconia- and ceria-based ceramics are used as oxygen storage promoters. Moreover, zirconia-based ceramics are used to make oxygen sensors designed to control the air–fuel ratio and increase exhaust gas purification rate [OKA 09]. $Pt/BaO/Al_2O_3$ based catalysts are used to absorb NO_x and react with hydrocarbons under oxidizing conditions [KWA 06].
Recently, several ceramic materials were employed as active solid oxide fuel cells components. For example, nickel/Y-TZP can be used for anodes while cathodes can be made from a mixed conducting perovskite *i.e.*, pure or with strontium-doped lanthanum manganite ($La_{1-x}Sr_xMnO_3$). Y-TZP can also be used as electrolyte while doped lanthanum chromite ($LaCrO_3$) is used as interconnect [ORM 03].
The recent rise of 3D-printing methodologies (stereolithography, selective laser sintering, electron beam melting, *etc.*) improved the design of hierarchical porous ceramics that are developed by direct ink writing and *in situ* growth of well-ordered metal–organic frameworks [LIU 20]. This process is illustrated in Figure 1.1. This method reduces the catalytic degradation rates of porous ceramics and improve their lasting degradation efficiency when compared to traditional processing routes. 3D-printed catalytic filters and impeller agitators are successfully manufactured using this method while spent residue catalysts are used as raw materials to product wear resistant ceramics.

In addition to their use as catalysts, ceramic materials enter the fabrication of several automotive constituents such as sensors or engine parts. For example, silicon nitrides are used to build turbochargers with reduced turbo-lag that enhance driving performances [BOC 10]. When compared to metal rotors, high-revolution speeds are shorten for ceramic rotors. Furthermore, piezo-electric ceramics are used as knock sensors that have the ability to detect slight vibrations and react before severe knocking [KIM 07]. Silicon carbide composites reinforced by carbon fibers enter the composition of brake discs 65% lighter than regular cast-iron brake discs [WU 19]. Those are more efficient as they maintain high-friction at more-elevated temperatures. Piezo-injector actuators are made of piezo-ceramic materials as $Pb(Ti,Zr)O_3$ which allows the needle valves to open and close. Finally, adiabatic turbo-compound diesel engines use silicon carbides with low thermal conductivity to enhance the thermal energy supplied to exhaust pipes and improve gasoline engine efficiency as well as reducing energy losses. Gas turbines can be equipped with silicon nitride based elastic supports and parts joined that use ceramic-based composite materials. These technical improvements can minimize the gas leaking at joints with relatively low contact stresses[OPI 03].

Ceramics materials are also widely used in the electronic industry with applications in telecommunication, transport, computers and consumer sectors for product miniaturization. In particular, materials with high thermal conductivity are of interest for the

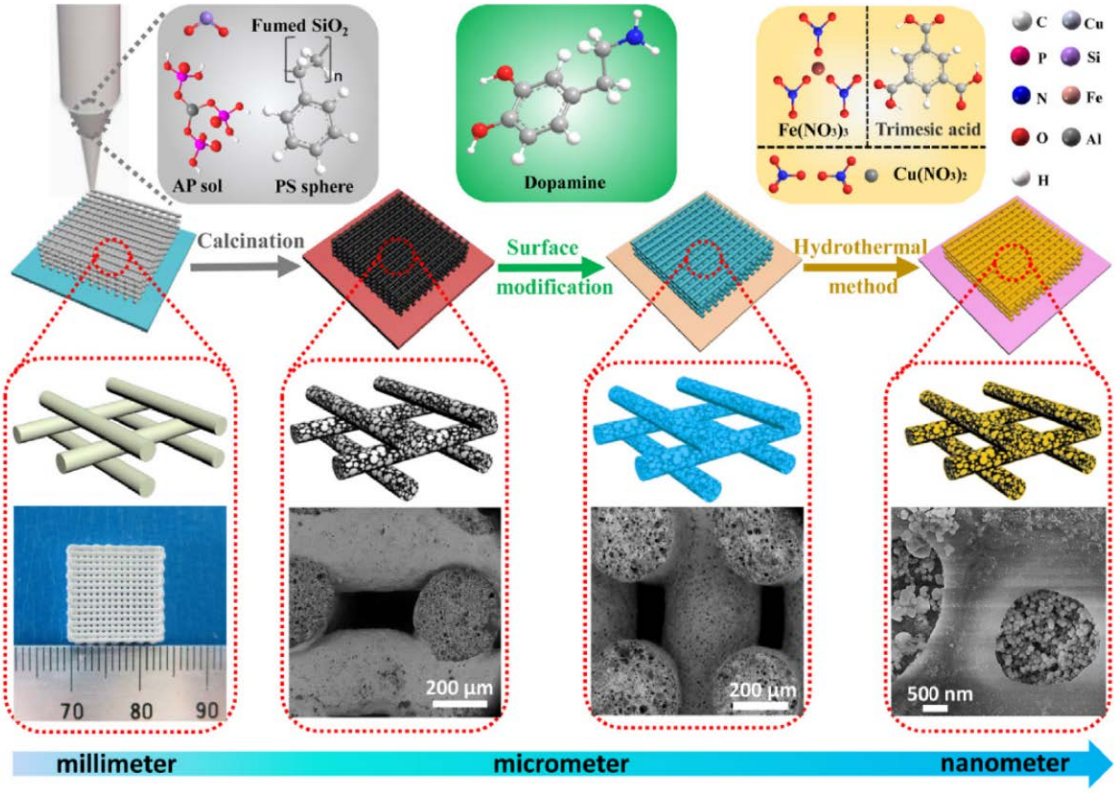

Figure 1.1: Hierarchical porous ceramics manufactured by 3D printing. From [LIU 20].

temperature management of integrated electronic devices. Kim *et al.* designed aluminum nitrides that were originally sintered with various additives such as CeO_2, Sm_2O_3, Y_2O_3, CaO, $CaZrO_3$ to minimize the grain growth [KIM 18]. Thus, these ceramics exhibit improved thermal conductivity (90–156 W/mK) and mechanical strength (560-710 MPa). Silicon nitrides (Si_3N_4) also show excellent thermal properties with high-thermal resistance and conductivity [MUT 03] in addition to better machining properties and an high electrical resistance that makes it a good candidate as high-thermal conductivity dielectric material.

Ceramic-based capacitors are used in electronic equipments such as transformers and antiferroelectric ceramic filters [FUJ 00, IMO 07, ZHA 10]. Barium titanate ($BaTiO_3$) nanomaterials are used for their high permittivity and stable dielectric properties [PIT 03]. When alloyed to MgO and Y_2O_3, they are shaped as multilayers to make capacitors[SON 05, CHO 06]. Thanks to the diffusion of alloying elements, $BaTiO_3$-based materials with various concentration gradients and a shifted Curie temperature can be obtained [SON 05].

1.1.3 Ceramics for energy and other environment technologies

Concentrated solar power systems are one of the most promising and sustainable technologies for environmental electric energy [FER 18]. They are made of an absorber that collects sunlight while the solar energy is used to produce steam that drives an electricity turbo-generation unit. Absorbers are mainly made out of graphite, alumina and silicon carbide ceramics.
Ultra-high temperature ceramics such as ZrB_2 or HfB_2 are ideal for thermal protection systems as they benefit from high chemical and structural stability at extreme operating temperatures, with a melting temperature of 3250 °C (while ZrO_2 and MgO reach respectively at 2700 °C and 2800 °C) [SCI 13, FAH 17]. They are widely used in the aerospace industry for hypersonic vehicles, rocket motor nozzles or atmospheric entry probes capable of the most extreme entry conditions. On the other hand, SiC ceramics and composites (ZrB_2-SiC) are considered as promising materials for fusion energy systems as they are very stable (*i.e.* oxidation resistance, high hardness and retained strength) at HT ($T > 2000$°C) or harsh conditions including radioactive environments. SiC ceramic matrix composites benefit of interesting microstructure- and constituent-dependent structural properties. They are characterized by the enhanced reliability, predictability and tailorability of various properties including high-thermal conductivity at HT in addition to benefit from non-brittle behavior. Finally, ceramic nanofibers are currently envisaged as possible new materials for energy conversion and storage devices as they benefit of high porosity and large surface area and they are already commonly used as photoelectrodes of dye-sensitized solar cells [BIS 12, ZHO 17].

1.2 Towards micro- and nanoscale ceramics

Modern techniques including severe plastic deformation and high-pressure spark plasma sintering are used to improve the mechanical properties of bulk materials using optimized formability approaches. Indeed, these methods are used to reduce the grain size and benefit of the Hall-Petch behaviour down at the nanoscale [MOR 01, YAN 08, SOK 17]. As shown Figure 1.2, polycrystalline materials exhibit higher hardness and strength up to a certain grain size decrease down to the micro- or even to the nanoscale [MOR 01, HUA 20]. This strategy was recently applied to ceramics including alumina and zirconia-based alloys (see *e.g.*, [SAN 08, CHR 08]). In this section, we introduce the basic concepts related to the mechanics of nanocrystalline materials and how they apply to ceramic materials.

1.2.1 Reducing the grain size towards nanocrystalline materials

When decreasing the grain size the yield strength of polycrystalline materials increases while their ductility decreases. This behaviour is modeled by the Hall-Petch relation

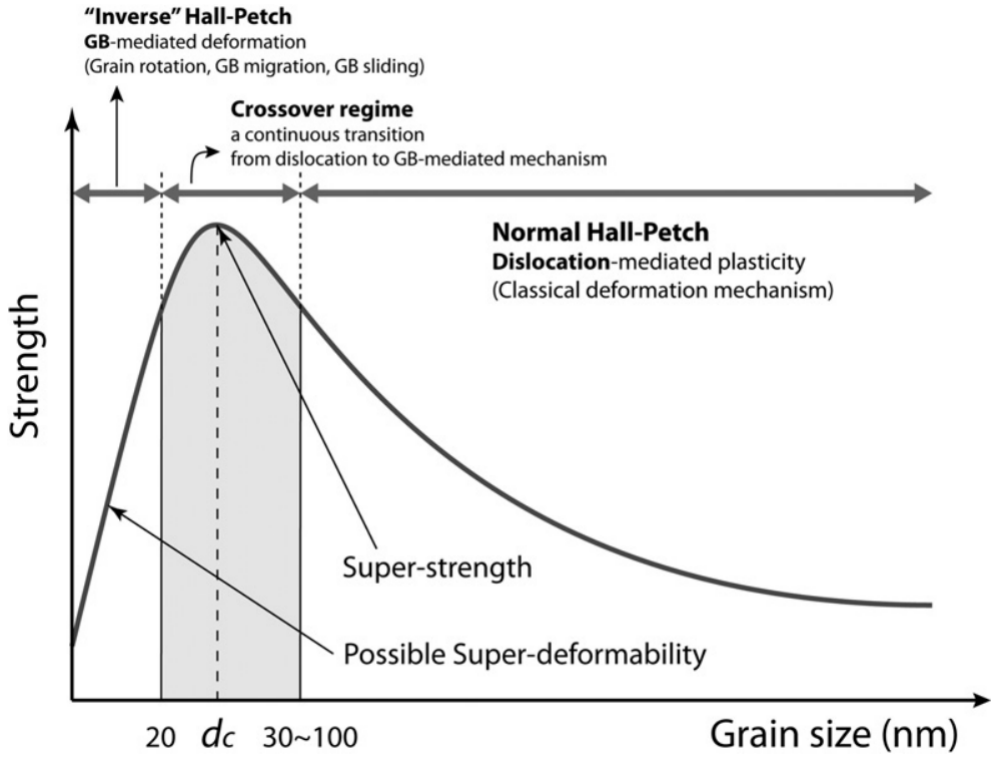

Figure 1.2: Hall-Petch diagram: strength *vs.* grain size. Adapted from [GRE 11].

(Equation 1.1) that rationalizes the link between the yield strength of a polycrystalline material and the grain size,

$$\sigma_c = \sigma_0 + \frac{k}{\sqrt{d}} \tag{1.1}$$

where σ_c is the critical strength, d is the grain size and σ_0 and k are constants.

If grains are larger than few tens of nm (normal Hall-Petch regime), the strength increases with decreasing their size due to the reduction of the dislocation mean-free path [HAL 51, AGE 09]. This at the cost of a critical strain reduction before failure. This behaviour applies down to few tens nm. For instance, the yield strength of nanocrystalline Cu is about six times larger than that of coarse-grained Cu [WAN 02, VAL 02]. Nevertheless, while the yield strength of Cu increases reducing the grain size its critical strain decreases from 45% to 4% strain. After the maximum strength (*super-strength* label on Figure 1.2) get reached, an inverse Hall-Petch regime replaces the normal one *i.e.*, the strength of polycrystals starts to decrease with decreasing the grain size. In this regime, the regular dislocation-mediated plasticity is replaced by grain-boundary plasticity (rotation, sliding, shearing), partial dislocation emission and absorption at grain boundaries [KE 95, VAN 01b, YAM 02, GIA 06]. This regime can induce super-deformability

[MAR 08].

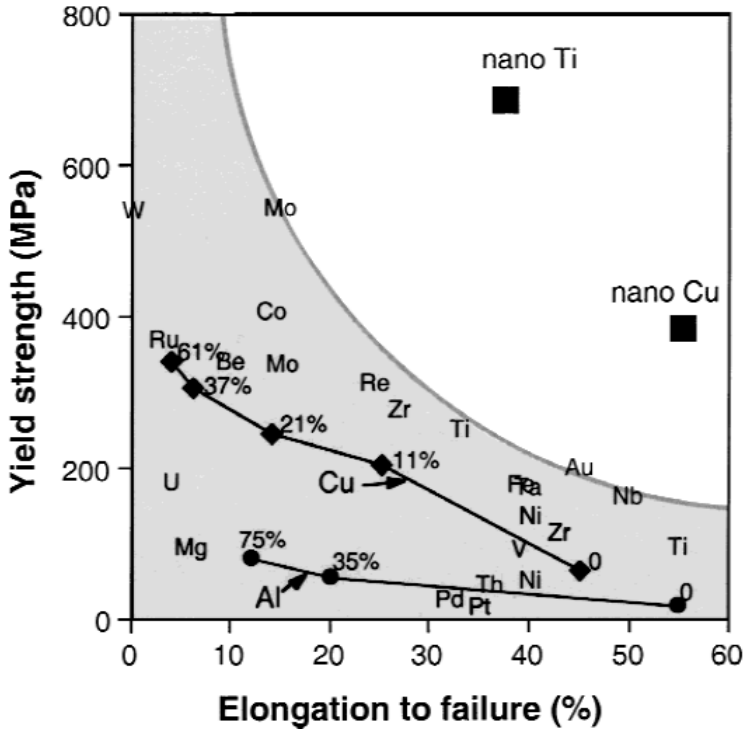

Figure 1.3: Yield strength and ductility improvements obtained using severe plastic deformation on various metals. The black curves describe pre-deformation paths for Cu and Al (the % refers to the material size reduction). From [VAL 02].

As shown Figure 1.3, plastic deformation can also be used to modify mechanical properties. Here, Valiev and co-authors use cold rolling and equal channel angular pressing leading to an increase of the yield strength together with a diminution of the critical strain before failure. This is illustrated by the two black curves that describe Cu and Al respectively (the % value refers to the material thickness reduction obtained before testing). With accumulated plastic deformation, the yield strength of Cu and Al increases while their elongation to failure decreases. As mentioned by the authors, a similar behaviour was observed in Ti (but the yield strength increase with grain size diminution is not described in the original paper). While the authors argue about the influence of the grain size reduction on the enhanced ductility, they also mention the influence of the high-pressure applied and its implication in the formation of nanoscale microstructrures what confirms that the observed mechanical behaviour is not the sole effect of the inverse Hall-Petch process.

Figure 1.4a to c illustrate the inverse Hall-Petch effect in nanocrystalline copper using tensile MD simulations [SCH 98]. In order to simplify the analysis of the simulation,

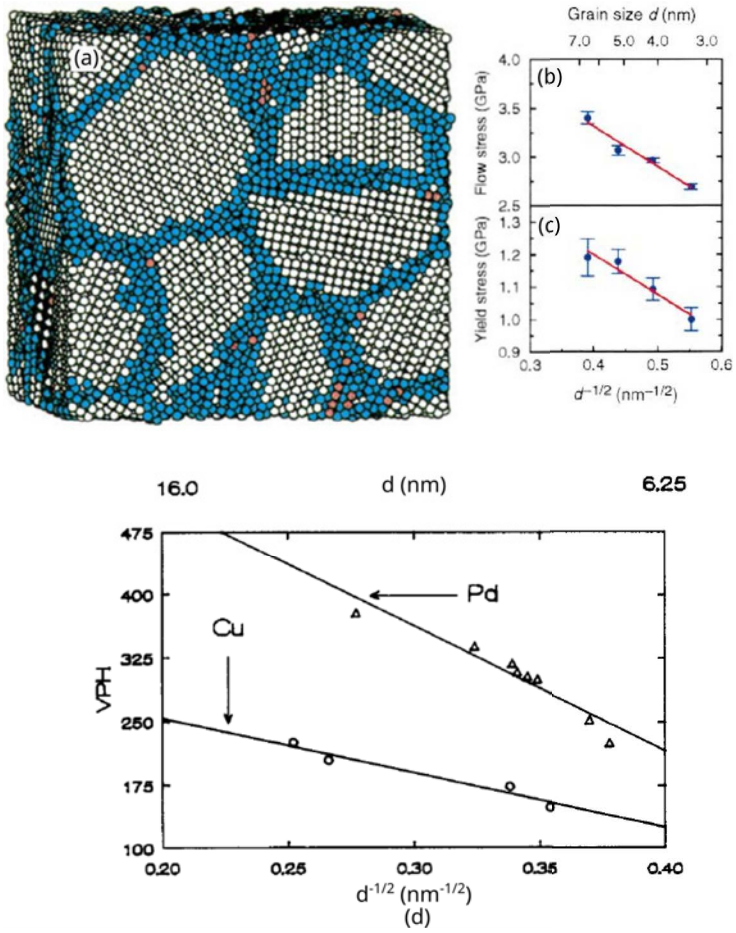

Figure 1.4: MD simulation and experiments of the inverse Hall-Petch behaviour in nanocrystalline metals. (a) Copper nanocrystalline sample as modelled using MD. (b, c) Yield and flow stresses versus inverse square root of grain size in nanocrystalline copper. (d) Experimental results showing the inverse Hall–Petch behaviour in nanocrystalline copper and palladium at RT (VPH = Hardness, in HV unit). Adapted from [SCH 98, CHO 89].

atoms not in local FCC and HCP crystalline order are classified as Grain Boundary (GB). In this study, the authors used a simulation cell of about 10 nm size that contains few grains from 3.3 to 6.6 nm size. Results show that both the yield and flow stress decreases with decreasing the grain size. Figure 1.4d presents and experimental illustration of the inverse Hall–Petch behavirous here in nanocrystalline copper and palladium at RT. The hardness is soften from 16 to 6.25 nm as the grain size decreases [CHO 89].

MD simulations and experiments in metals have shown that grain boundary sliding and amorphization could be responsible for the inverse Hall-Petch relation in nanocrystalline metals [SCH 98, KUM 03, LEG 08]. Fan *et al.* proposed a composite model (Figure 1.5) in which when the grain size d is decreased to a critical value d_c, the plastic deformation is dominated by grain boundary sliding [FAN 05].

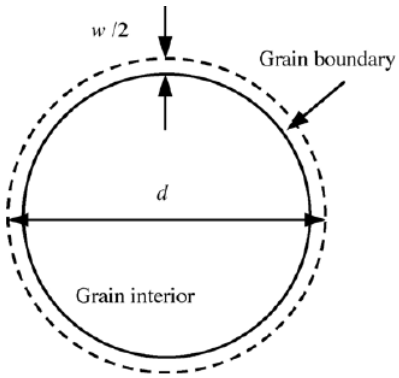

Figure 1.5: Illustration of the Fan model for grain boundary deformation within the inverse Hall-Petch regime [FAN 05].

Several strategies were developed to improve the ductility of nano-structured metals. Wang *et al.* introduce a bimodal grain size distribution by a thermomechanical treatment with pure nanocrystalline Cu to improve the ductility [WAN 02]. He *et al.* presente a new *in situ*-formed nanocrystalline matrix/ductile dendritic phase composite microstructure for Ti alloys [HE 03]. Ti alloys exhibit large compressive plastic strains together with high strength and high ductility. Interface-based nanostructuration using GBs or twins are also commonly used to enhance the mechanical properties of nanocrystalline materials. They rely on a combination that seems to improve both strength and ductility. That is typically the case of nanotwinned metals that exhibited higher yield strength and critical strain than their twin-free counterparts. Jang *et al.* produced twinned Cu nanopillars that exhibit a BDT for samples with CA normal to the Twin Boundary (TB) [JAN 12]. MD simulations were also used to study the plastic deformation of nanotwinned nanopillars by Wu *et al.* [WU 10]. The authors observed two new dislocation mechanisms, which may explain the extreme strength and ductility found in nanotwinned Cu. For the authors, Shockley partial dislocations mainly contribute to the ultrahigh ductility while sessile stair-rod and Frank partial dislocations are responsible for the ultrahigh strength. Inspired by the outstanding mechanical behaviours of nanotwinned metals, Kou *et al.* produced three-order nanotwinned metals (Figure 1.6) with enhanced mechanical properties that are investigated using *in situ* TEM experiments and MD simulations [KOU 14]. The three-order twinned alloys show the outstanding yield strength, compared with other metal materials.

Ceramic materials also exhibit a similar yield stress *vs.* grain size trend. For example, Ryou *et al.* [RYO 18] performed a set of indentation tests on dense $MgAl_2O_4$ with grain sizes ranging from 3.6 to 37.5 nm. Figure 1.7 shows the evolution of the hardness as function of the grain size including a maximal hardness of 22.5 GPa for a grain size of about 19 nm. Ehre *et al.* have also shown that the Vickers microhardness of nanocrystalline MgO obeyed the Hall-Petch relation with a maximum value of 15 GPa for a grain size of about

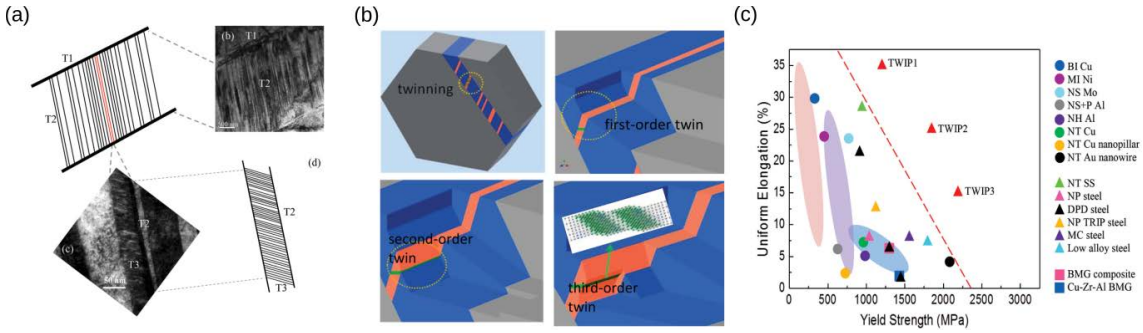

Figure 1.6: Deformation mechanisms in three-order nanotwinned metals. (a) TEM images that show twinned structures before and after tensile deformation. (b) Simulation images of the three-order twinned structure. (c) Yield strength of the three-order twinned alloy as compared with other metal materials. Adapted from [KOU 14].

30 nm [EHR 08]. Furthermore, the authors show that the hardness decreases from 15 to 6 GPa when grain size decreasing from 25 to 3 nm, typical of the inverse Hall-Petch regime. Huang *et al.* performed deformation experiments on α-alumina polycrystals within the Scanning Electron Microscrope (SEM) as well as MD to investigate nanoscratch properties [HUA 10]. They observed the BDT in alumina at small-scale confirming the grain-size role on the ductility of alumina.

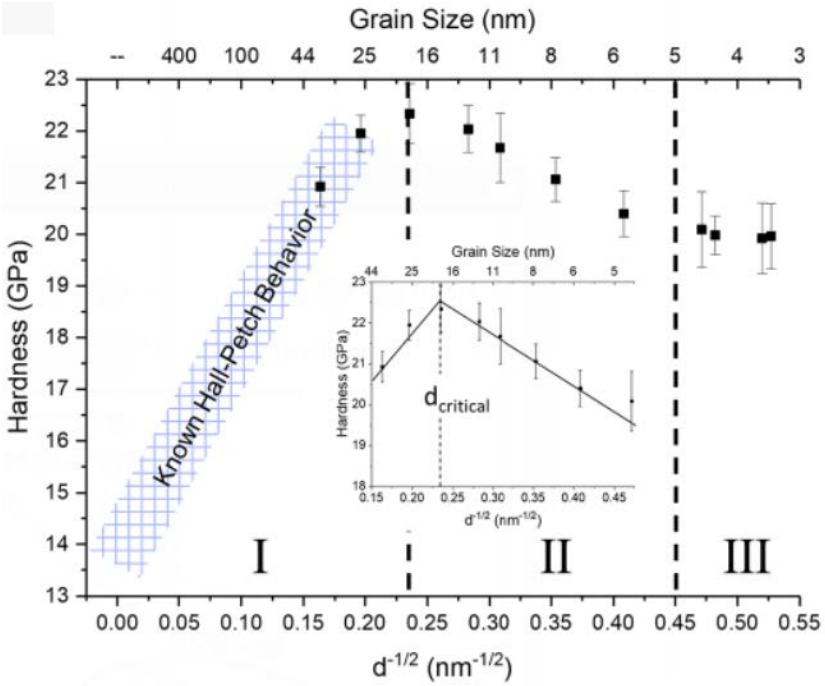

Figure 1.7: Nanoindentation of nanocrystalline $MgAl_2O_4$. Hardness as a function of grain size. The three regions I, II and III represent the Hall/Petch regime, a plateau transient and the inverse Hall-Petch regime, respectively. From [RYO 18].

Guo *et al.* used a similar approach than Fan applied in their case to nanocrystalline boron carbide (B_4C) [GUO 18]. In their work, amorphous bands nucleate from the intersections of grain boundaries and then grow into 2–3 nm wide amorphous zones. These amorphous zones contribute to the plastic deformation and promote grain boundary sliding. The same mechanism was recently identified as one of the main deformation process in olivine, one of the main mineral ceramic compound of the Earth upper mantle [SAM 21].

To better understand and improve the mechanics of nanocrystalline materials, the scientific attention focuses on both the role of GBs and the behaviour of isolated single crystalline micro- and nano-objects like pillars, particles or wires under stress. This last topic will be covered in the next section.

1.2.2 Small-scale mechanics

1.2.2.1 Insights from micropillar compression tests

In recent years, the investigation of the elementary deformation processes in nanocrystalline materials becomes more reliable with the development of modern small-scale mechanics techniques such as nanoindentation, *in situ* nanocompression tests and multi-scale modeling.
Most of the studies were performed on metal alloys. In the early 2000s, Uchic *et al.* reported particularly high compressive strength for single crystalline Ni micropillars when compared to their bulk counterpart [UCH 04]. Figure 1.8 shows the stress-strain response of pillars with size ranging from 20 to 40 µm compressed along the ⟨134⟩-orientation at RT. Overall a *smaller is stronger* trend is noticed together with an enhanced ductility for smaller samples. Kiener *et al.* focused on the tensile behavior of copper single crystals at the micro-scale [KIE 08]. The authors confirmed the size-dependence of the flow stress as well as a strain-hardening regime strongly dependent on the sample aspect ratio. Extensive micro-compression and tensile experiments within the SEM and TEM were conducted on other microscale objects (*e.g.*, whiskers and wires) by the Richter group [RIC 09, SED 12]. Schneider *et al.* performed compressive tests on body-centered-cubic (W, Mo, Ta, and Nb) micropillars with size ranging from 1 to 5 µm using compression experiments within the SEM [SCH 09]. They found that the strength increases when the pillar diameter size decreases. The same trend is found in HCP Mg and Ti micropillars [BYE 10, LIL 10, YU 10]. For example, Lilleodden *et al.* performed compression experiments inside a TEM on Mg micropillars with diameters ranging from 6.1 to 15 µm along the ⟨0001⟩-direction. They show that the stress required for deformation twinning strongly increases with decreasing pillars size when deformed at the micro-scale. Yu *et al.* also confirmed this behaviour testing single crystalline Ti alloy micropillars with diameters ranging from 1 µm to 8 µm under uniaxial compression experiments inside the TEM.

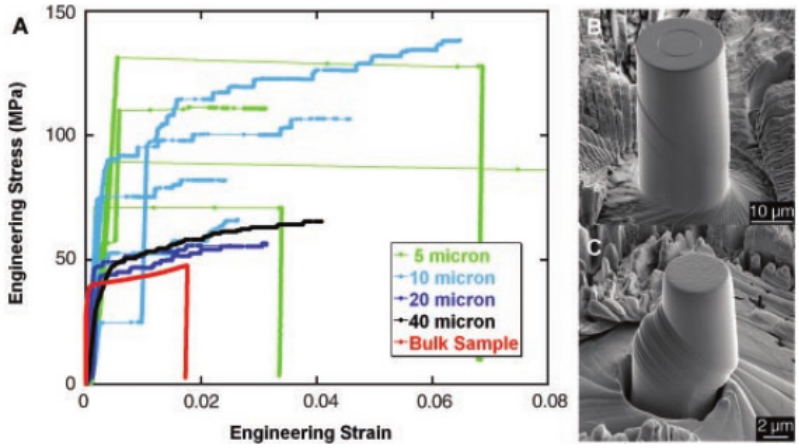

Figure 1.8: Mechanical behaviors of Ni micropillars compressed along $\langle 134 \rangle$ inside the SEM at RT. (A) Stress-strain curves for Ni micropillars ranging from 5 to 40 µm in diameter, compared with Ni bulk. (B) A 20 µm Ni micropillar after compression. (C) A 5 µm Ni micropillar after compression. From [UCH 04].

While less studies are referenced in the literature when compared to metals and alloys, ceramic micro- and nano-objects are also under investigation.
As example, Korte *et al.* studied the size-effect on the yield stress of MgO pillars using SEM compression experiments [KOR 11a]. Results show a BDT in MgO and favour dislocation glide rather than cracking under higher stress in smaller pillars. Indeed, for the soft direction <001> ($\frac{1}{2}\langle 110 \rangle \{110\}$ slip systems activated), the yield stress varies from 0.75±0.29 to 2.65±0.37 GPa with decreasing size *i.e.*, about 20 times larger than the macroscopic flow stress at RT (∼20–60 MPa). In addition, Korte *et al.* used 3D electron backscattered diffraction to investigate the effects of size on plastic deformation of MgO micropillars [KOR 11b]. These results were recently resumed in a review paper focusing on dislocations and deformation of MgO [AMO 18].

1.2.2.2 Deformation of micro- and nanoparticles

Several groups (including MATEIS) recently focused on the behaviour of individual crystal at small scales. While it provides fundamental piece of information about mechanical properties and elementary deformation processes, a bottom-up approach allows for a better understanding of the mechanical behaviour of nanocrystalline materials as focusing on their original block *i.e.*, the individual single grain.

One of the pioneer work about single grain mechanics at small-scale is the study of Mordehai and colleagues about gold particles [MOR 11]. In this study, the authors show a correlation between strength and size of Au micro- and NPs similar to the one observed

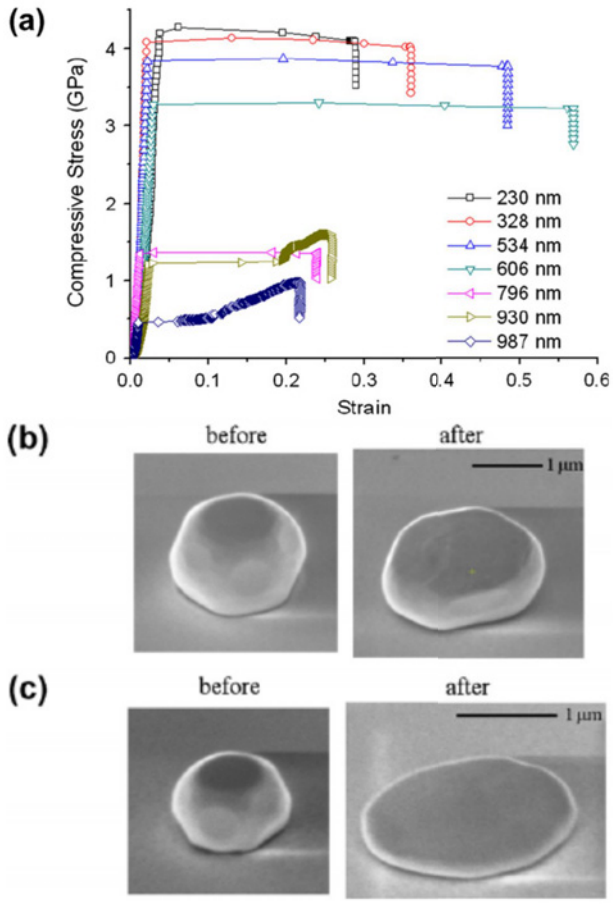

Figure 1.9: Mechanical behaviour of Au microparticles under compression. (a) Stress-strain curves for different sample sizes. (b,c) SEM images of Au particles (987 and 230 nm) before and after compression. Adapted from [MOR 11].

in pillars using multi-scale simulations including the Finite-Element Method (FEM) and MD as well as SEM compression tests. Figure 1.9a shows compressive stress-strain curves of several Au particles (230-987 nm size range). All particles are first characterized by an elastic regime. Then, smaller microparticles (<600 nm) show a particularly elevated yield stress followed by strain bursts of large amplitude while lower-range yield strength and strain-hardening can be observed in larger samples. After deformation, these particles exhibit a characteristic 'pancake' shape (Figure 1.9b,c). The authors also performed MD simulations to better asses the deformation mechanism of Au microparticles. They conclude that the deformation was governed by dislocation nucleation from the vertices and corners of the modelled NPs. Both computed and experimental strengthes approach the theoretical strengths of Au (3.12 GPa [WAN 13a]) at the beginning of plasticity, especially for smaller size samples.

Feruz *et al.* used MD to study the strength of various FCC single crystal NPs [FER 16].

Compression tests were performed on ideal Wulff-shaped NPs (Figure 1.10a) along the <111> direction. Figure 1.10b shows simulated stress-strain curved up to the nucleation-induced stress drop in Au NPs. In particular, the results show that the yield stress decreases as the size of the NPs increases. In all investigated FCC nanometals, the plastic regime starts thanks to the nucleation of Shockley partial dislocations at the vertices or corners of the NPs.

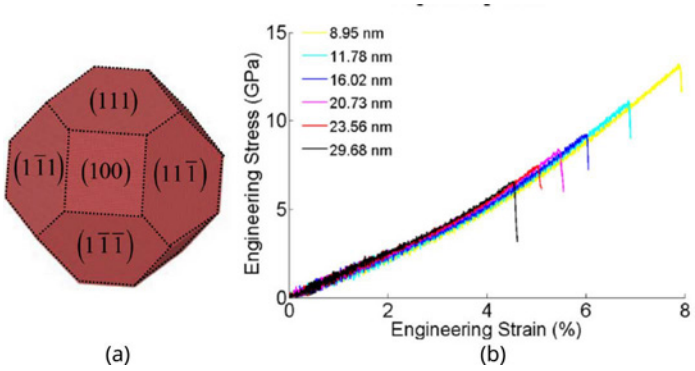

Figure 1.10: MD simulation of Wulff-shaped Au NPs. (a) Wulff-shaped Au NPs compressed along <111> using MD simulations. (b) Simulated stress-strain curves. Adapted from [FER 16]

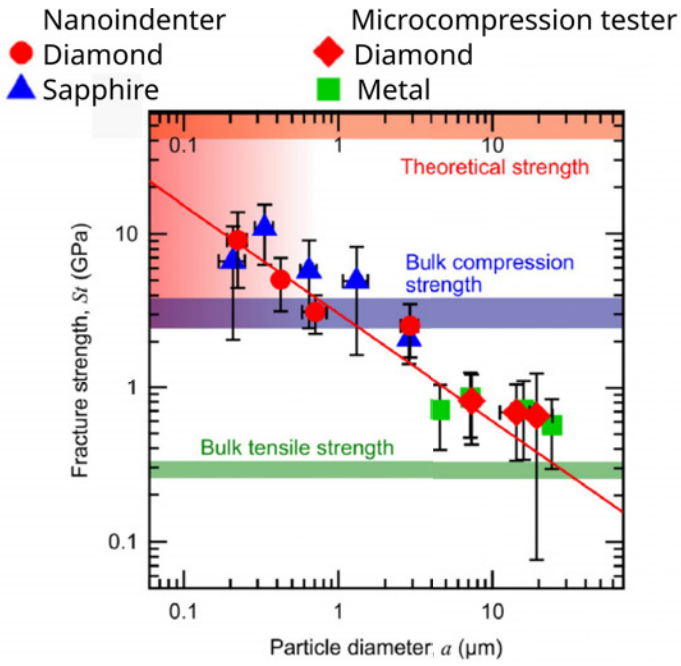

Figure 1.11: Fracture strength of α-Al_2O_3 microparticles as function of the particle diameter. The theoretical, bulk compression and tensile strengths are shown for comparison. From [KUR 20].

Similar approaches combining MD and *in situ* SEM or TEM were also applied to ce-

ramics. Kuroyanagi *et al.* investigated size-effect in α-Al_2O_3 microparticles [KUR 20]. In this study, they authors performed *in situ* TEM microcompression tests of crystalline particles with diameters ranging from 15 to 30 µm. Comparisons of the sample fracture strength to the theoretical, compressive and tensile bulk strengths (Figure 1.11) indicate that the strength required for crack propagation increases as the sample size reduces due to enhanced plastic deformation as discussed in [SCH 72, WAN 13b].

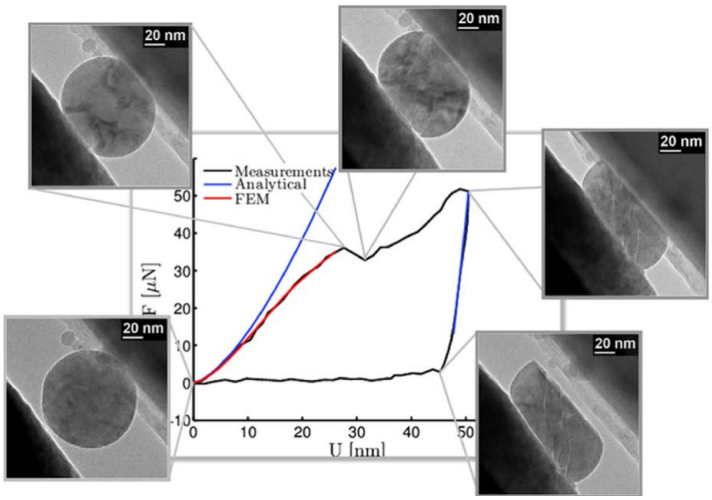

Figure 1.12: *In situ* TEM nanocompression of an alumina NP. High-resolution TEM (HRTEM) images and mechanical response (black curve). The simulation using digital image correlation and finite-element is shown in red, the analytical Hertz fit is shown in blue. From [CAL 14].

Nevertheless, different mechanisms seem to be involved in the deformation of alumina NPs depending on their size. As shown by Calvie *et al.*, the mechanical properties of small alumina NP (<100 nm) exhibit ductility without sign of cracks up to large strains [CAL 14]. In this study, the authors developed a methodology to determine the constitutive laws of NPs based on *in situ* TEM compression tests using digital image correlation. A force-displacement curve is shown in Figure 1.12 from which the parameters of the constitutive law are extracted using two different methods either the Hertz theory for the load curve of the elastic response or a cylinder for the unload curve. The constitutive model involves four parameters which includes the Poisson ratio υ=0.3, the effective Young's modulus E^*=115 GPa, the initial yield stress σ_y=10 GPa and a strain hardening coefficient H. For larger particles (>100 nm), the authors show that the mechanical behaviour is close to bulk *i.e.*, force-displacement exhibits a brittle behaviour with crack propagation within the elastic regime as seen in Figure 1.13a,c. In this case, the maximum compressive strength is 3.4 GPa.

Issa *et al.* also investigated the mechanisms of ⟨100⟩-oriented MgO nanocubes using *in situ* TEM compression tests performed at RT as well as MD [ISS 15, ISS 21]. Results show a surface dislocation nucleation process at way higher stress (few GPa) than in bulk MgO

single crystals. Dislocations were identified within the $\frac{1}{2}\langle 110\rangle\{110\}$ slip systems (Figure 1.14). Also, the authors have shown than increasing the size of the nanocubes leads to a transition *i.e.,* from dislocation nucleation to dislocation multiplication [ISS 21].

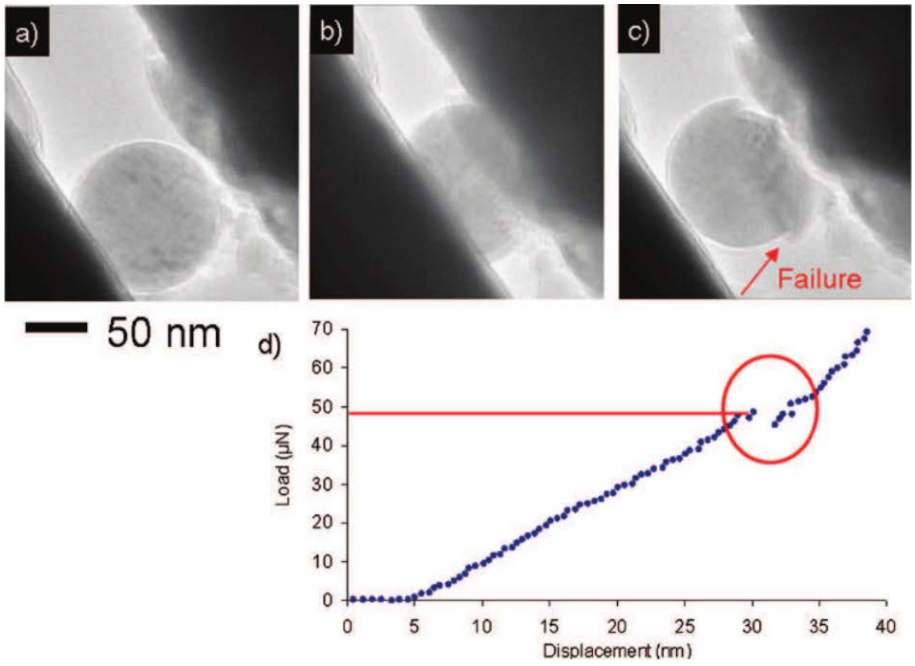

Figure 1.13: *In situ* TEM nanocompression of a 125 nm alumina NP. (a,c) TEM images that illustrate the starting configuration, the loading and the fracture of the NP, respectively. (d) corresponding force–displacement curve. The red circle emphasize the fracture initiation. From [CAL 14].

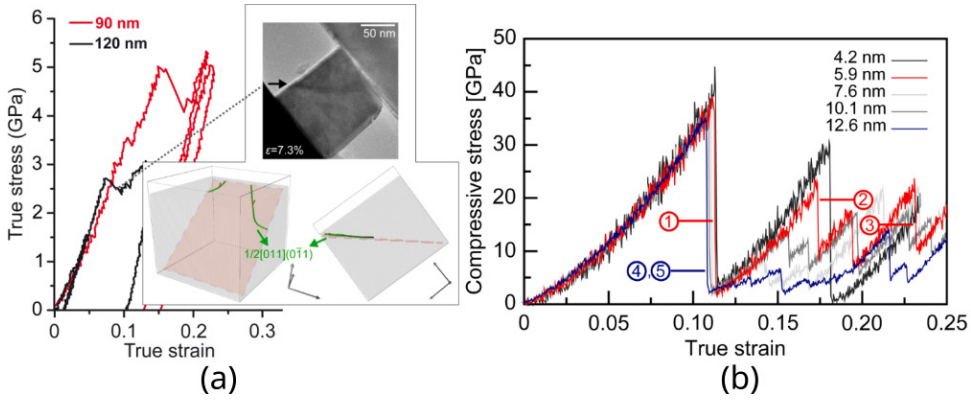

Figure 1.14: *In situ* TEM and MD of $\langle 100\rangle$-oriented MgO nanocubes under compression at RT. (a) Stress–strain curves of MgO nanocubes and dislocation nucleation in 90 and a 120 nm samples. MD simulations confirm dislocation nucleation events from corners and edges within the $\frac{1}{2}\langle 110\rangle\{110\}$ slip mode. (b) MD stress–strain curves. Adapted from [ISS 15]

In contrast with bulk materials, micro- and nanoscale particles can sustain extremely high stresses (in the GPa range) and ductility, even in the case of originally brittle ma-

terials. This behaviour is related to various elementary deformation processes including dislocation nucleation and twinning. Amodeo and Pizzagalli recently published a review article on NP mechanical properties with an emphasis on modeling elementary deformation processes [AMO 21]. The reader can refer to their work and references therein to get a broader overview about the mechanics of NPs. In the next section, we will focus on alumina *i.e.*, from the applications to its atomic-scale elementary properties.

1.3 α-alumina

Alumina is the second most abundant metal oxide of the earth crust next to silica. It can appear under various crystalline phases called α, β, γ or δ with the most common and the one of interest here being sapphire (also called corundum) *i.e.*, α-Al_2O_3.

1.3.1 Applications

α-alumina is used in several fields of applications especially for its excellent mechanical properties and bio-compatibility.For example, millions of alumina ceramic orthopedic implants were manufactured from the 1970s mostly due to producers such as Ceramtec in Germany or CERAVER in France [NEV 01, DAL 07]. Alumina alloys were introduced in orthopedics by Pierre Boutin who invented non-porous alumina to use it as the total hip replacements [BOU 77]. In 1988, Boutin *et al.* pointed out that perfect bone stock quality as well as high-quality ceramics are prerequisites for durable fixation of total hip prosthesis [BOU 88]. Massin *et al.* studied four generations of Biolox Delta ceramics in total hip replacement [MAS 14]. They showed that Biolox products reduce the risk of wear and implant failure in comparison to metal bearing surfaces.

Several studies followed these pioneer works and the first drawbacks of alumina ceramics identified were their modest toughness. Generally, alumina ceramics are brittle under impact and initial implant-fracture rates could reach several percent [DEA 02]. Then, alumina compounds have to be thicker than with other, tougher materials in order to satisfy the strength levels required for clinical uses leading to a loss of bone stock [HUL 93]. Even after long-lasting microstructural developments and a continuous increase of their strength supported by a decrease of the failure ratio (less than 0.1%), there is still a need to develop alumina alloys with higher toughness [CHE 09].

Since decades, α-alumina has been used for dental bracket, implants, abutments as well as frameworks for crowns to enforce the strength of dental porcelains [ALS 14]. The high purity alumina crown copings or fixed prostheses cores are fabricated using computer-aided

design and manufacturing techniques. The first fully dense dental alumina polycrystalline ceramic (Procera^{TM} AllCeram) was introduced in 1993 [LI 14]. It contains more than 99.9% alumina and has a high flexural strength (600 MPa). The outer contour of the coping is milled to the programmed thickness and dimension sintered and is then veneered with aesthetic porcelain including a compatible coefficient of thermal expansion. Microstructural and morphological factors influence the improvement of alumina ceramics mechanical properties.
Several factors such as elongated grains (high aspect ratio grains), small grain sizes and narrow grain size distribution allow to enforce toughness and reduce surface roughness [KOV 96, KOV 00]. Furthermore, combination of alumina with other compounds such as zirconia are also often used to improve material properties. For example, Ce-TZP/Al_2O_3 nanocomposites are considered as a promising materials for dental implants.

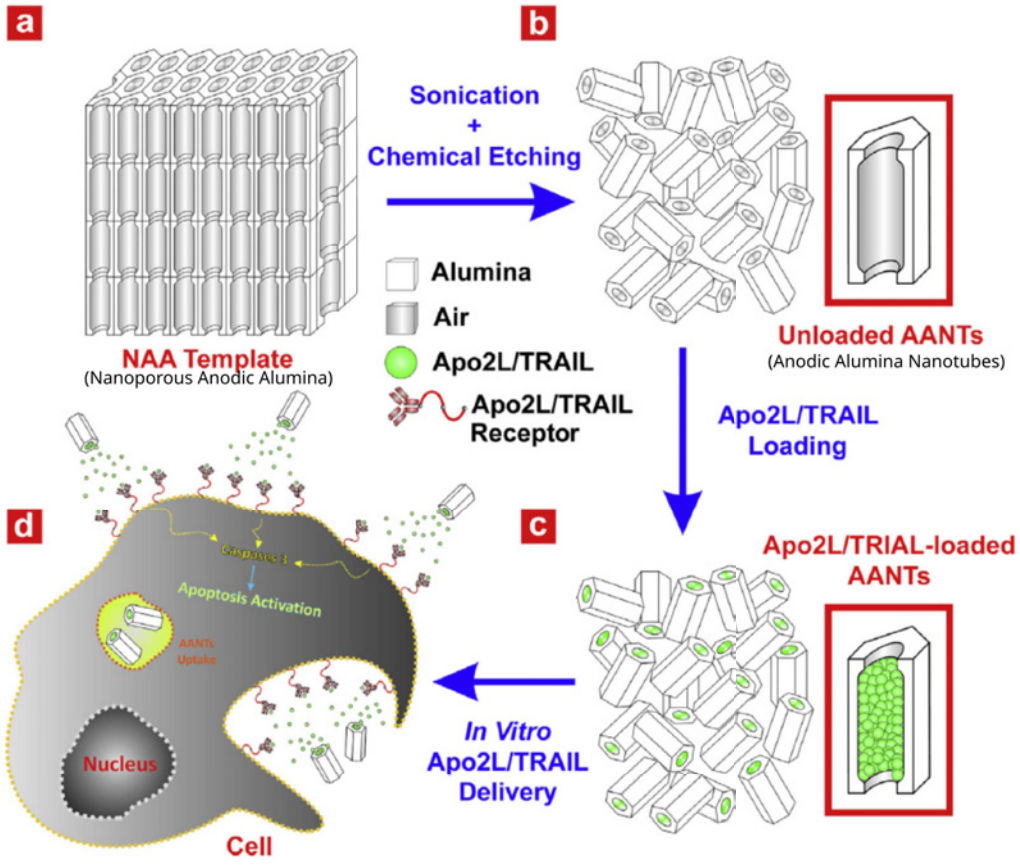

Figure 1.15: Fabrication, loading and drug delivery using alumina nanotubes[WAN 14].

Bulk alumina is also used for drug delivery. As example, Nanoporous Anodic Alumina (NAA) is a promising biomaterial due to its unique microstructural features including a regular pore size and a uniform pore density. NAA shows high stiffness and strength as

well as elevated chemical and thermal stabilities [WAN 14]. Anodic Alumina Nanotubes (AANTs) are used as nano-carriers for drug delivery of anticancer therapeutics. Figure 1.15 summarizes the fabrication of AANTs, their drug loading (here Apo2L/TRAIL, a model drug) and the mechanism of release to eliminate cancer cell apoptosis. AANTs are fabricated to provide high loading and biocompatibility. The NAA template is spread using a chemical etching process into several small-size alumina nanotubes, and each nanotube is then loaded with *in vitro* drugs to be delivered into cells.
Alumina is also used as grinding or abrasive material. For example, Yin *et al.* investigated the material removal rate during an abrasive process for the single-phase polycrystalline alumina and for a two-phase alumina–titania composite. The results reveal identical mechanisms of microfracture and grain dislodgement under the grinding conditioned applied. There were no distinct differences in surface roughness and morphology for both materials ground at either conventional or high speed [YIN 05].
Finally, α-alumina is also commonly used for electronic applications as a constituent of conductors and high-voltage resistors. Wada *et al.* tested mutual grain-boundary transport of aluminum and oxygen in polycrystalline α-Al_2O_3 under oxygen potential gradients at HT [WAD 11]. α-Al_2O_3 is predominantly an electronic conductor at HT and both the aluminum and oxygen ions migrate without any acceleration or inhibition due to the interdiffusion. Moreover, Belkin *et al.* demonstrated that the insulating properties of alumina nanocapacitors can be recovered after high voltage breakdown opening promising routes for a new generation of self-healing capacitors [BEL 17]. Xiong *et al.* found that α-Al_2O_3 interlayers can be used to enhance open-circuit voltage for hole-conductor-free C-Based perovskite solar cells [XIO 18]. In this context, an alumina interlayer serves as an excellent insulating layer to divide cathode and anode. Moreover, it also modifies the interface between the Electron Transport Material (ETM) and various perovskites retarding the recombination at the ETM/perovskite and perovskite/counter electrode interfaces simultaneously.

After this short introduction about (non exhaustive) alumina applications, the next section we will focus on lattice aspects and deformation properties of α-Al_2O_3.

1.3.2 Lattice and elastic properties

α-Al_2O_3 belongs to the $R\bar{3}c$ space group and can be described by a rhombohedral or an hexagonal unit cell. The hexagonal cell is made of 30 atoms and the lattice parameters are a_0=4.76 Å and c_0=12.99 Å [GIE 68]. Along the [0001] basal direction, the α-Al_2O_3 crystal structure can be described by the succession one oxygen layer consecutive to two aluminum layers shifted from each other, see Figure 1.16. The basic structure thus consists of hexagonal close-packed planes of oxygen intercalated with aluminum planes.

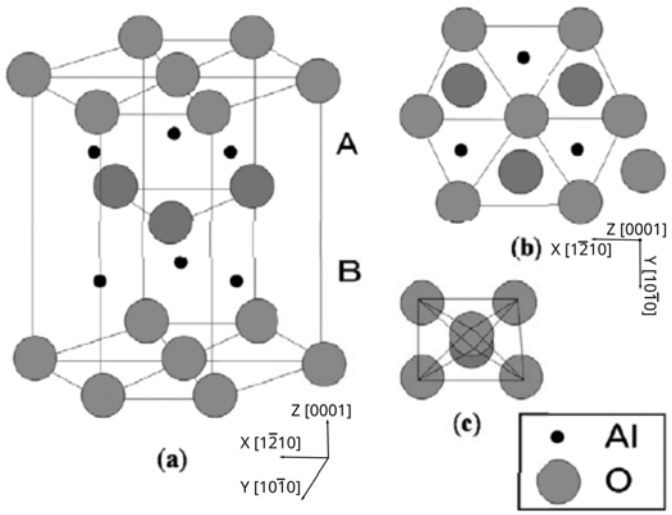

Figure 1.16: Crystal structure of α-Al_2O_3. (a) 3D view, (b) Projected view along [0001], (c) Octahedral substructure. From [SHI 10].

The four index notation of Miller-Bravais is often used to describe HCP crystals. It refers to th $hkil$ indices withm $i = -(h + k)$. Using this notation, the characteristic angle θ between two crystallographic planes (h_1, k_1, i_1, l_1) and (h_2, k_2, i_2, l_2) in α-Al_2O_3 can be described as follow,

$$cos(\theta) = \frac{(h_1h_2 + k_1k_2) + 1/2(h_1k_2 + h_1k_2) + 3/4(a/c)^2 l_1 l_2}{\sqrt{(h_1^2 + h_1k_1 + k_1^2) + 3/4(a/c)^2 l_1^2}\sqrt{(h_2^2 + h_2k_2 + k_2^2) + 3/4(a/c)^2 l_2^2}} \tag{1.2}$$

Reference	**Elastic constants**					
	C_{11}(GPa)	C_{12}(GPa)	C_{13}(GPa)	C_{14}(GPa)	C_{33}(GPa)	C_{44}(GPa)
[OHN 86]	496.9±1.4	162.3±1.6	115.5±1.6	-21.9±0.2	500.5±1.6	146.8±0.2
[MAY 60]	496.0	135.0	117.0	-23.0	502.0	14.01
[WAC 60]	496.8±1.8	163.6±1.8	110.9±2.2	-23.5±0.3	498.1±1.4	147.4±0.2
[BER 63]	490.2	165.4	113.0	-23.2	490.2	145.4
[TEF 66]	497.4	164.0	112.3	-23.6	499.4	147.4
[GIE 68]	497.6±0.2	162.6±0.4	117.2±0.2	-22.9±0.1	501.9±0.2	147.2±0.1
Average	496.1±1.8	164.3±1.2	115.0±2.4	-23.1±0.7	499.2±2.9	146.0±1.6

Table 1.1: α-Al_2O_3 single crystal elastic constants.

Table 1.1 and 1.2 show elastic constants for α-Al_2O_3 single crystals as derived from experimental measurements. In particular, the table 1.2 shows that the orientation $[1\bar{1}02]$

exhibits the lowest Young's modulus of 418±26 GPa [CHE 17, KON 21]. On the other hand, Young's modulus of 451±25 GPa and 445±17 GPa are obtained for the [0001] and $[11\bar{2}0]$ directions, respectively [WAD 95, CHE 17, MAO 11, SAL 94, OLI 92, KON 21]. Among the four orientations tested to compute the shear modulus G, $[11\bar{2}0]$ leads to the lowest value with G=169.5 GPa while the orientation $[1\bar{1}00]$ is the leads to the highest one *c.a.* G=254.5 GPa. Figure 1.17a,b show the variations of the shear modulus and thermal expansion as function of temperature in single crystal α-Al_2O_3. As the temperature increases, the thermal expansion increases while the elastic moduli decreases.

Reference	E **(GPa)**			
	[0001]	$[11\bar{2}0]$	$[1\bar{1}02]$	
[WAD 95]	461.0			
[CHE 17]	456.5	431.2	386.1	
[MAO 11]	461.0			
[SAL 94]	465.0	430.0		
[OLI 92]	445.7			
[KON 21]	451.0	462.0	398.0	
	G **(GPa)**			
	[0001]	$[1\bar{1}00]$	$[11\bar{2}0]$	$[1\bar{1}02]$
[MA 20]	227.0	254.5	169.5	180.0

Table 1.2: α-Al_2O_3 single crystal Young's (E) and shear (G) moduli.

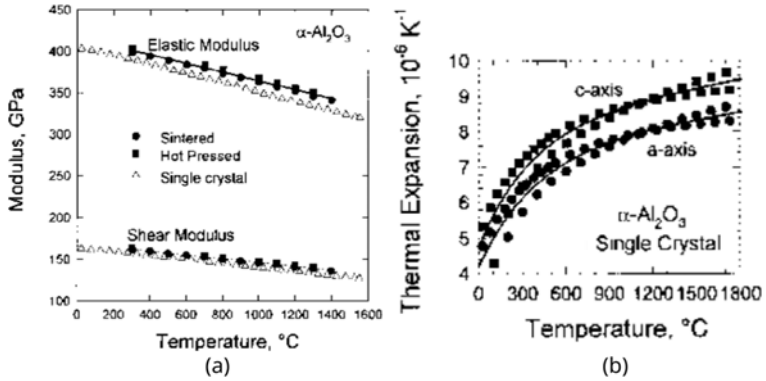

Figure 1.17: Elastic and thermal properties for single crystalline α-Al_2O_3 as function of temperature. (a) Shear (G) modulus. (b) Thermal expansion. Adapted from [MUN 97].

1.3.3 Plastic properties

1.3.3.1 Insights from experiments

α-Al_2O_3 deformation is characterised by several possible slip modes including $\frac{1}{3}\langle 1\bar{2}10\rangle(0001)$ basal slip, prismatic slip modes $\frac{1}{3}\langle 1\bar{2}10\rangle\{10\bar{1}0\}$ and $\frac{1}{3}\langle 10\bar{1}0\rangle\{1\bar{2}10\}$, rhombohedral slip $\frac{1}{3}\langle 0\bar{1}11\rangle\{01\bar{1}2\}$ and pyramidal slip modes [VEN 94]. In the literature, α-Al_2O_3 crystallographic planes and slip systems are often called using acronyms *i.e.*, c for basal slip, m and a for the two respective prismatic planes and R for the rhombohedral one as shown Figure 1.18a. The pyramidal slip modes are referred as the s $\frac{1}{3}\langle\bar{1}101\rangle\{10\bar{1}1\}$ or $\frac{1}{3}\langle\bar{1}2\bar{1}0\rangle\{10\bar{1}1\}$, n $\frac{1}{3}\langle\bar{1}101\rangle\{2\bar{1}\bar{1}3\}$ or $\langle 01\bar{1}0\rangle\{2\bar{1}\bar{1}3\}$, w $\frac{1}{3}\langle\bar{1}102\rangle\{2\bar{1}\bar{1}2\}$ or $\langle 01\bar{1}0\rangle\{2\bar{1}\bar{1}2\}$ as well as v $\langle 01\bar{1}0\rangle\{4\bar{2}\bar{2}3\}$ [SNO 73]. Figure 1.18b shows an inverse pole figure describing α-Al_2O_3 slip planes respective orientations as well as the angles between important directions. For example, using the Miller-Bravais notation introduced in Equation 1.2, the angle between the R plane $(1\bar{1}02)$ and the c plane (0001) is $\sim$58.0° while the angle between the s plane $(01\bar{1}1)$ and the c plae is $\sim$72.7°.

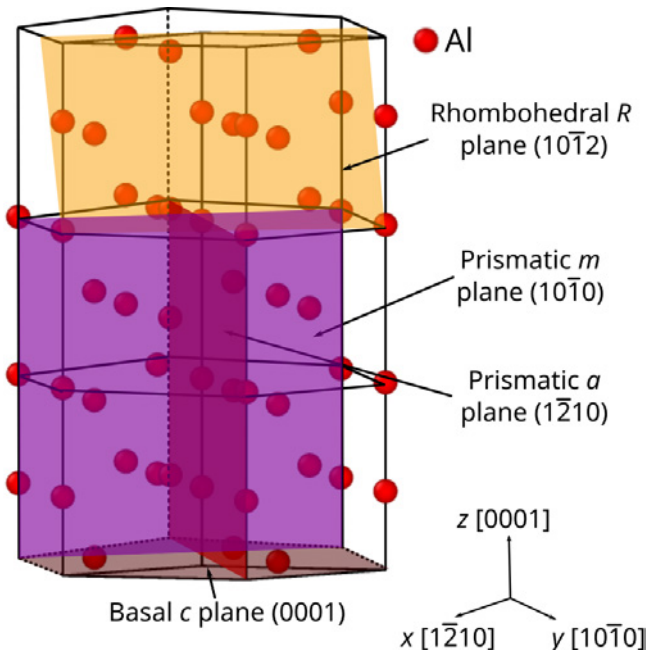

Figure 1.18: Slip systems and relative cristallographic directions in α-Al_2O_3. (a) Slip system orientation as described within the HCP unit cell (only the Al sublattice is shown). (b) Inverse pole figures including important slip plane directions and angles.

Castaing *et al.* [CAS 81a] investigated the mechanical properties of α-Al_2O_3 single crystal under compression between 25°C and 1800°C. Two compression directions were investigated (i) CA parallel to the c axis and (ii) at 45° from the c axis, to respectively observe basal and prismatic slip. Indeed, prism a slip $\frac{1}{3}\langle 1\bar{2}10\rangle\{10\bar{1}0\}$ was observed dur-

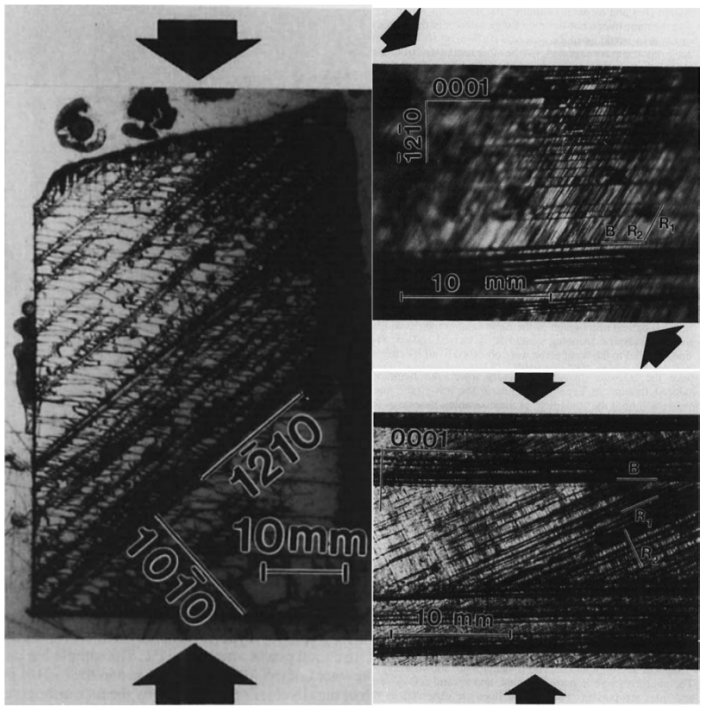

Figure 1.19: Slip traces in α-Al_2O_3 observed by transmission optical microscopy. (a) Prismatic m and a slip observed during deformation with CA parallel to a basal surface (T = 200°C). (b) R and c twinning systems when deformed 45° to $\langle 1\bar{2}10 \rangle$ and $[0001]$ at T=600°C. Adapted from [LAG 94].

ing plastic deformation above 200°C while c slip was activated above 600°C. Lagerlof *et al.* observed dislocation slip and twinning in sapphire using two sets of TEM experiments [LAG 94]. First, CA was aligned with a $\langle 0001 \rangle$-oriented lateral face. The authors observed prismatic a and m slip (see Figure 1.19a) at temperatures as low as 200°C. Second, CA was set at 45° from a $\langle 1\bar{2}10 \rangle$ direction where more complicated processes as basal and rhombohedral twinning were observed down to T=400°C (Figure 1.19b). Basal slip was also observed in this second configuration at higher stresses. Also, Snow *et al.* observed various sets of pyramidal slip systems using TEM in deformed polycrystalline alumina at 1150°C [SNO 73]. Geipel *et al.* observed rhombohedral twins in α-Al_2O_3 single crystal under compression along a prism a $\langle \bar{2}110 \rangle$ direction at 600°C using HRTEM experiments and indicate that they were "screw twins" with a $[0\bar{1}11]$ twin axis that involves shear along $\frac{1}{6}[0\bar{1}11]$ leading to a two-fold rotational symmetry [GEI 94]. Finally, He *et al.* observed basal and rhombohedral twinning under compression along prism a $[\bar{1}\bar{1}20]$ and m $[\bar{1}010]$ directions at 700 and 800°C during HRTEM experiments [HE 02].

The basal edge dislocation is known to be one of the most common to appear during HT deformation tests and is the more investigated in the literature [LAG 83, LAG 94, BOD 05, SHI 07, HEU 10]. $\frac{1}{3}\langle 1\bar{2}10 \rangle$ perfect edge dislocation can dissociate into two par-

tial dislocations with Burgers vectors $\frac{1}{3}\langle 10\bar{1}0\rangle$ and $\frac{1}{3}\langle 01\bar{1}0\rangle$ as shown in Equation (1.3).

$$\frac{1}{3}\langle 11\bar{2}0\rangle \rightarrow \frac{1}{3}\langle 10\bar{1}0\rangle + \frac{1}{3}\langle 01\bar{1}0\rangle \tag{1.3}$$

The dissociation process operates along a $\langle 0001\rangle$ direction via a climbing mechanism resulting into two 60° mixed dislocations [HEU 10]. Still, a net controversy persists about the partial dislocation core structures. Two main models were introduced to explain basal partial core structures and dislocation slip. Firstly, Kronberg *et al.* proposed that partial dislocations can glide between two consecutive Al and O layers [KRO 57]. This slip model involves charge transport due to the strong bonding between Al and O atoms. Secondly, Bilde-Sørensen *et al.* proposed a mixed partial core that glides between two consecutive Al layers without charge transfer [BIL 96]. While Shibata *et al.* confirmed Kronberg's hypothesis using the SEM [SHI 07], Heuer *et al.* produced a markedly detailed atomic model of the dislocation cores with Al-Al terminated partial dislocations using the negative spherical-aberration imaging technique supporting the Bilde-Sørensen's model [HEU 10].

Montagne *et al.* studied the deformation processes of α-Al_2O_3 pillars using RT *in situ* SEM microcompression experiments [MON 14]. Four crystallographic orientations were investigated including m $[1\bar{1}00]$, a $[2\bar{1}\bar{1}0]$, R $[\bar{1}012]$ as well as c [0001]. The authors show that the deformation processes of α-Al_2O_3 micropillars depend on orientation with multiple slip-systems involved including rhombohedral $\frac{1}{3}\langle\bar{1}101\rangle\{1\bar{1}02\}$ and $\frac{1}{3}\langle 0\bar{1}11\rangle\{0\bar{1}12\}$ as well as pyramidal $\frac{1}{3}\langle 0\bar{1}11\rangle\{1\bar{1}01\}$ slip systems (see Table 1.3 and Figure 1.20).

Compression plane	Uniaxial stress (GPa)	Schmid factor	Active slip system
$\{1\bar{1}00\}$ (m)	13.6	0.45	$1/3\langle\bar{1}101\rangle\{1\bar{1}02\}$ (R)
$\{2\bar{1}\bar{1}0\}$ (a)	11.1	0.38	$1/3\langle 0\bar{1}11\rangle\{1\bar{1}01\}$ (s)
$\{0001\}$ (c)	23.7	0.45	$1/3\langle 0\bar{1}11\rangle\{0\bar{1}12\}$ (R)
$\{\bar{1}012\}$ (R)	(13.0)		crack

Table 1.3: Slip plane activity as function of orientation during α-alumina micropillar compression tests performed at RT. From [MON 14].

1.3.3.2 Atomistic simulations

MD simulations are often employed to supplement experimental studies on dislocation nucleation and deformation processes at small-scale [AMO 21]. These simulations are currently applied to investigate the deformation of single crystals. MD has been used for several ceramics, but only few results deal with alumina or nanocrystalline structures. MD appears as the most popular tool to model material deformation at small-scale due to its

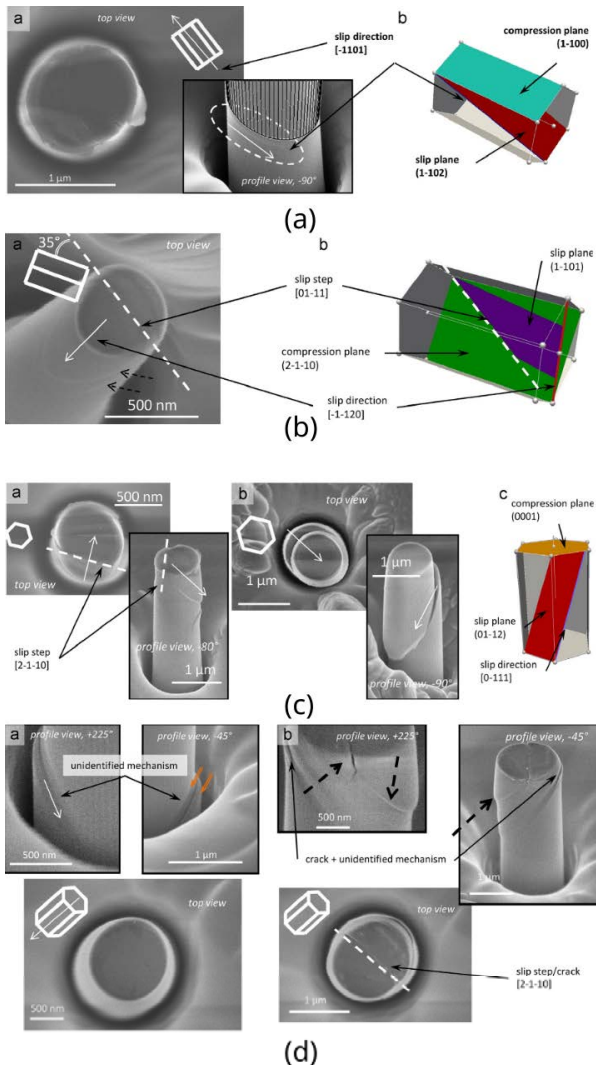

Figure 1.20: SEM compression of α-alumina micropillars. (a) Activation of the rhombohedral slip planes R when CA aligned with the $[1\bar{1}00]$-orientation, (b) Activation of the pyramidal slip planes s $(1/3\langle 0\bar{1}11\rangle\{1\bar{1}01\})$ when CA aligned with the $[2\bar{1}\bar{1}0]$-orientation, (c) Activation of rhombohedral slip planes R $(1/3\langle 0\bar{1}11\rangle\{0\bar{1}12\})$ when CA aligned with the $[0001]$-orientation, (d) The micropillar show a brittle behaviour when CA aligned with the $[\bar{1}012]$-orientation. Adapted from [MON 14].

ability to describe atomic-scale elementary deformation processes (dislocation nucleation, twinning) in virtual nanosamples with sizes comparable to the experiments.

Recently, MD simulations were used to study the nanoindentation and nanocompression of brittle ceramics such as silicon nitrides and carbides [NIS 08]. As already discussed, it has also been used to investigate the plastic deformation of MgO NPs [ISS 15, ISS 21] or ZrO_2 pillars [DU 15, ZEN 16]. However, few is done about the modeling of deformation processes and the mechanical properties of alumina. Sarobol *et al.* investigated the plas-

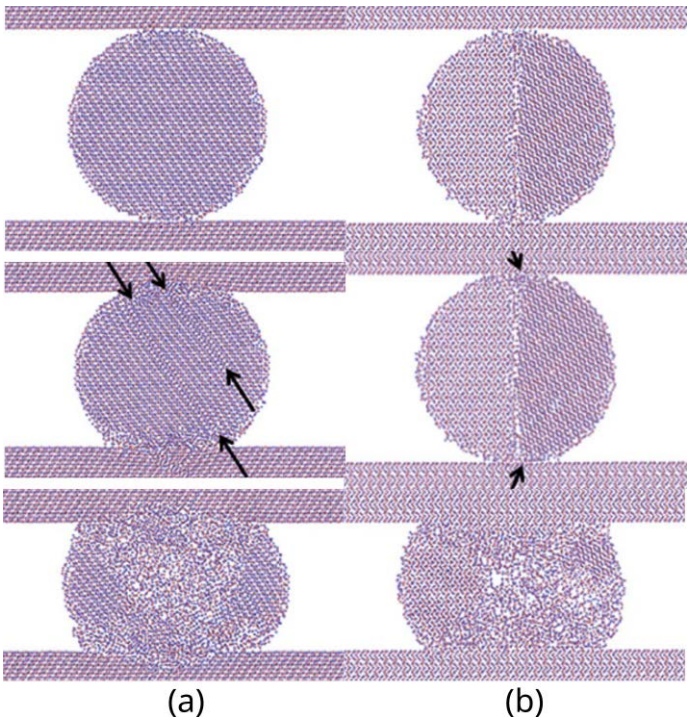

Figure 1.21: MD compression simulations of alumina single crystal and bicrystal NPs. (a) Single crystal NP shown (i) before compression, (2) during loading and (3) at the end of there test when the NP breaks, respectively. (b) Similar illustration in a bicrystalline NP where the nucleation of voids is also observed. Adapted from [SAR 16].

ticity of defective and defect-free alumina micro-, submicro- and NPs under compression using *in situ* TEM experiments and MD simulations [SAR 16]. For single crystalline NPs under compression along [0001] at RT, the authors observed dislocation nucleation from the contact area between the indent and the NPs. These dislocations nucleate within the rhombohedral slip system (Figure 1.21a). After deformation, the authors show that NP fractured and split into two separated parts. For bicrystals, atom reshuffling is observed at the contact between the indent and the grain boundary before voids appear and the bicrystal fractures (Figure 1.21b). No dislocation nucleation was observed in the bicrystal NP simulations.

Zhang *et al.* investigated the deformation mechanisms of α-alumina thin films using MD simulations under hyper velocity impact loading [ZHA 08]. In the simulation, a cylindrical projectile is thrown towards the alumina (0001) surface at hyper velocity 18 Km/s. Analysis of inner impact faces p and q (see Figure 1.22) show wild deformation under the impact and nucleation of dislocation due to the influence of local stress concentration. Multiple elementary deformation processes were identified including pyramidal $(2\bar{1}\bar{1}3)$ slip, $(0\bar{1}11)$ twins, basal slip and twins as well as rhombohedral $(01\bar{1}2)$ twins.

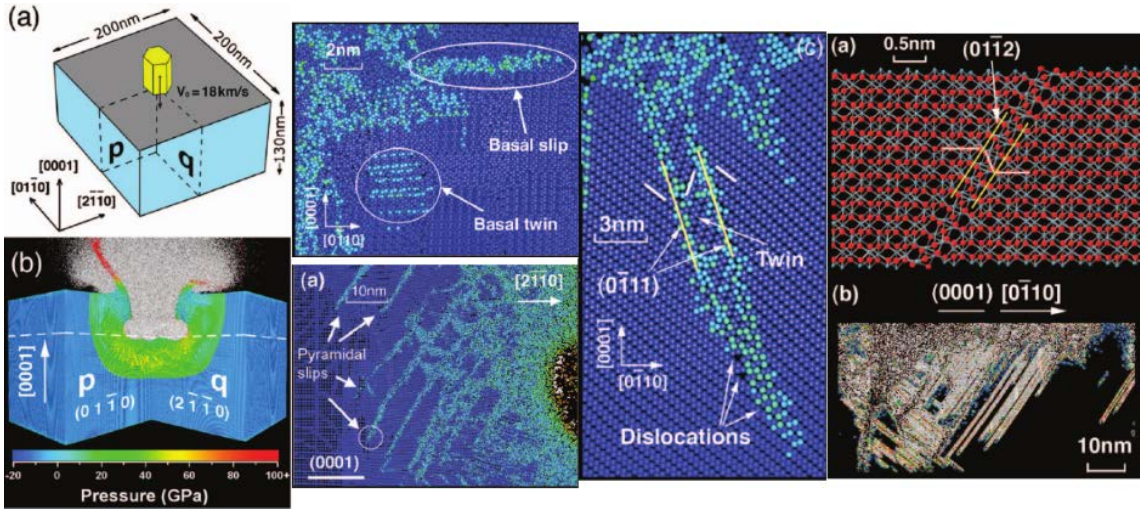

Figure 1.22: MD impact simulations at the surface of an alumina single crystalline thin film. Adapted from [ZHA 07].

Nishimura *et al.* performed MD nanoindentation at 300K in α-alumina [NIS 08]. Three orientations were investigated including [0001], [01$\bar{1}$0] and [2$\bar{1}\bar{1}$0] as shown Figure 1.23. Along the [0001] orientation, prismatic dislocations nucleate first from the contact surface where stacking faults are observed. Then, basal and pyramidal dislocations start to nucleate within the sample (Figure 1.23a). The prismatic and pyramidal dislocations were observed respectively using [01$\bar{1}$0] and [2$\bar{1}\bar{1}$0] orientations.

1.3.3.3 Summary

Overall, plastic deformation processes happening in α-Al_2O_3 for the 4 main directions c, m, a and R can be resumed as follow:

- For the c orientation [0001], at elevated temperatures ($> \sim$300°C), prismatic a slip is easy while pyramidal slip is known to be harder [GOO 72, CAS 81a, KOT 82, LAG 94, UCH 04]. R slip and twinning are more frequently observed at low temperature (LT) [ZHA 08, MON 14, SAR 16]. Basal and pyramidal slips were observed whatever T [GOO 72, CAS 81a, KOT 82, LAG 94, UCH 04].
- For the a orientation [1$\bar{2}$10], basal c and rhombohedral R slip and twinning are observed from RT to HT [GEI 94, LAG 94, HE 02, CAS 04, MON 14, MIA 19].
- For the m orientation [10$\bar{1}$0], c and R slip and twinning are observed from RT to higher temperatures [LAG 94, HE 02, MON 14]. In addition, prismatic slip can be activated at HT [NIS 08].
- For the R orientation [10$\bar{1}$2], no dislocation were observed up to now [ROB 93, MON 14] in the experiments while c, prismatic a, R, pyramidal s and n slips were in MD indentation [KIM 19].

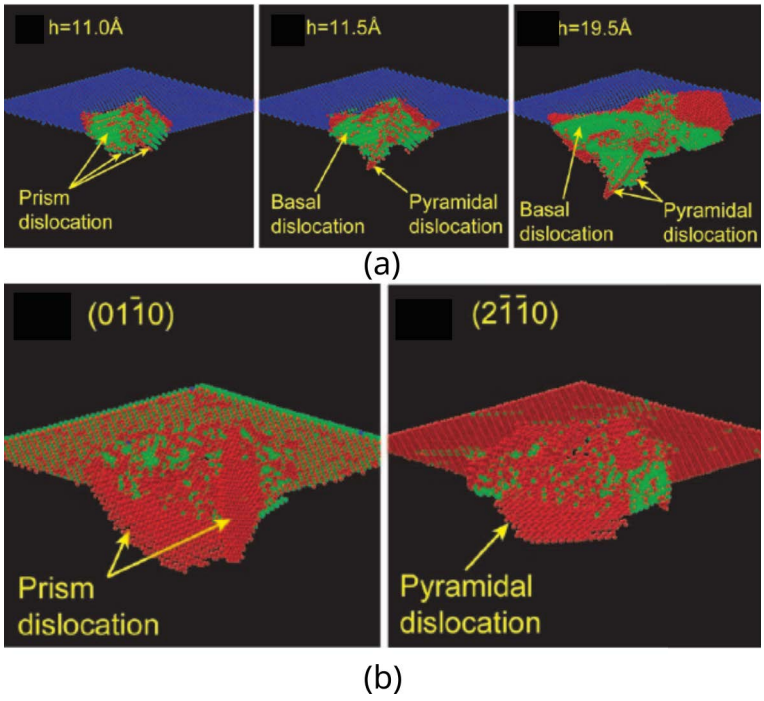

Figure 1.23: MD nanoindentation simulation in α-alumina. (a) $[0001]$ orientation, prismatic dislocations appear first at indenter depth h=11.0 Å before than basal and pyramidal dislocations nucleate. (b) Nucleation of prismatic and pyramidal dislocations during MD nanoindentation along $\left[01\bar{1}0\right]$ and $\left[2\bar{1}\bar{1}0\right]$ respectively. Adapted from [NIS 08].

A literature review of the plastic deformation processes occurring in α-alumina as function of orientation, temperature, type of test and analysis is provided Table 1.4.

After this literature review, the next chapter will focus on the various methods used during the Ph.D as well as on the various interatomic potential frameworks. Finally, the companion tools used in collaboration with the MD LAMMPS code will be introduced.

Chapter I summary:

Three main axis are covered in this literature review chapter to better assess the rest of the Ph.D manuscript. First, we have broadly introduced ceramic materials as well as their roles in various fields of applications. Second, we have discussed how decreasing size influence the mechanical properties of crystalline materials. Third, we have resumed the literature about α-alumina *i.e.,* from related applications to crystalline properties including lattice, slip system and dislocation properties.

Orientation	Temperature (°C)	Test/Analysis	Slip system	Reference
[0001] (c)	1600 to 1850	Compression/TEM	Pyramidal v slip	[KOT 82]
	1600 to 1800	Creep deformation/SEM	Pyramidal w slip	[GOO 73]
	25 to 1800	Compression/SEM	Prismatic a and basal c slips	[CAS 81a]
	25 to 1500	Tensile/SEM	Pyramidal s slip	[ÜNA 94]
	900	Indentation/MD	Rhombohedral R and prismatic m slips	[KIM 19]
	400	Compression/SEM	Basal c slip and R twinning	[LAG 94]
	300	Indentation/MD	Prismatic, basal and pyramidal slips	[NIS 08]
	RT	Compression/SEM	Rhombohedral R slip	[MON 14]
	RT	Compression/MD	Rhombohedral R slip	[SAR 16]
	10	Indentation/MD	Pyramidal n, basal c slips, rhombohedral R and c twinning	[ZHA 08]
$[11\bar{2}0]$ (a)	900 to 1300	Compression/TEM	Basal c slip	[CAS 97]
	600 to 1550	Compression/TEM	Rhombohedral R twinning	[CAS 04]
	900	Indentation/MD	Pyramidal n slip	[KIM 19]
	800	Compression/TEM	Basal c and rhombohedral R twinning	[LAG 94, HE 02]
	300	Indentation/MD	Pyramidal slip	[NIS 08]
	RT	Compression/SEM	Pyramidal s slip	[MON 14]
	RT	Compression/TEM	Basal c slip	[MIA 19]
	Low-T (-196)	Compression/TEM	Rhombohedral R twinning	[GEI 94]
$[10\bar{1}0]$ (m)	RT to 1500	Tensile	Fracture at directions [0001]	[ROB 93]
	600 to 1550	Compression/TEM	Basal c slip and twinning	[CAS 04]
	900 to 1300	Compression/TEM	Basal c slip	[CAS 97]
	900	Indentation/MD	Rhombohedral R and pyramidal n slips	[KIM 19]
	800	Compression/SEM	Basal c and rhombohedral R twinning	[LAG 94]
	700	Compression/TEM	Rhombohedral R twinning	[HE 02]
	300	Indentation/MD	Prismatic slip	[NIS 08]
	RT	Compression/SEM	Rhombohedral R slip	[MON 14]
$[10\bar{1}2]$ (R)	RT to 1500	Tensile	Fracture at directions $[11\bar{2}0]$ and $[\bar{1}012]$	[ROB 93]
	900	Indentation/MD	Basal c, prismatic a, rhombohedral R, pyramidal s, n slips	[KIM 19]
	RT	Compression/SEM	Fracture at direction $[2\bar{1}\bar{1}0]$	[MON 14]
	1150 to 1750	Bending/SEM	Prismatic a slip	[GOO 72]
	-196 to 1200	Bending/SEM	Basal c and Rhombohedral R twinning	[HEU 66]
	1600 to 1800	Creep deformation/SEM	Basal c slip	[FIR 76]
	1150	Compression/SEM	Rhombohedral R and Pyramidal slips	[SNO 73]
	900	Bending/Photomicrographs	Basal c slip	[WAC 54]

Table 1.4: Plastic deformation process observed in α-Al_2O_3 as function of orientation, temperature and technique. For indentation tests, the orientation refers to the indented sample surface while it corresponds to the compression/tensile axis in other cases.

Chapter 2

Methods

2.1 Atomistic simulations using the LAMMPS code

All along this thesis, we use the LAMMPS classical MD simulation code [PLI 95] to perform Molecular Statics (MS) and MD simulations of nanoscale α-alumina. This chapter recalls the basics of such atomistic simulation methods (within the LAMMPS framework) as well as theoretical aspects of the various types of interatomic potentials used for the study. Main information about companion tools (ATOMSK and OVITO) are also provided.

2.1.1 Energy minimization using molecular statics

Energy minimization simulations are the main class of MS simulations. These simulations are time-independent *i.e.*, they consist in parsing spatial configurations that are not correlated in time. As time is not defined, atoms have no velocity and thus no temperature can be defined in MS simulations (it is 0K). In MS, the potential energy E_{pot} of a set of atoms is expressed as:

$$E_{pot} = E(r_1, r_2, r_3, ..., r_N) \tag{2.1}$$

where r_i refers to the position of the i^{th} atom and N is the total number of atoms in the system.

Thus, the force F_i on the atom i is the negative derivative of the potential energy regarding the displacement of the i^{th} atom,

$$\overrightarrow{F_i} = -\overrightarrow{grad}(E_{pot}) \tag{2.2}$$

During MS simulations, a minimum energy configuration (local minimum) can be found

using an iterative process. It is achieved by moving the atoms along the $\overrightarrow{F_i}$ vectors defined by Equation 2.2. The presence of local and global minima is determined by the initial geometry of the system as well as the functional form of $-\overrightarrow{grad}(E_{pot})$.

In LAMMPS, several examples of minimization algorithms are available such as the Polak-Ribiere Conjugate Gradient (CG) [POL 69], the Hessian-Free Truncated Newton algorithm (HFTN) [NAS 85, MAR 10] or the Fast Inertial Relaxation Engine (FIRE) [BIT 06, GUÉ 20]. In CG, the pre-iteration information are merged with the force gradient to calculate a new search direction which is the conjugate (perpendicular) of the previous one at each iteration while a CG inner iteration is adapted to calculate a quadratic model of the potential energy using HFTN. The FIRE algorithm is an MD-inspired damped dynamics method that use velocity projection on force vector together with a variable timestep.
An strategy for typical energy minimization simulation (including pressure relaxation) using LAMMPS can be drawn as follow. First, the CG method can be used to minimize the potential energy of a given system using a force norm criterion of *e.g.*, 10^{-8} eV/Å as a stopping criterion. One can note that such minimization process does not allow for pressure relaxation by simulation cell changes. Thus, we secondly perform an anisotropic box relaxation using the LAMMPS fix box/relax to relax the pressure of the system. This step can be followed by last minimization run using CG, HFTN or FIRE.

2.1.2 Molecular dynamics

In contrast to MS, MD simulations allow the computation of time-dependent displacement of interacting atoms. In regular MD codes such as LAMMPS, MD proceeds in two steps. Firstly, the system energy is computed based on the interatomic potential used and the forces are derived from the system energy as in classical MS simulations. Then, the Newton equation of motion (Equation 2.3) is integrated.

$$m_i \frac{\mathrm{d}^2 \overrightarrow{r}_i}{\mathrm{d}t^2} = \overrightarrow{F}_i \tag{2.3}$$

where m_i is the mass of particle i and dt an elementary timestep.

A solution to Equation 2.3 can be found using the Verlet algorithm [VER 67], derived from a Taylor expansion,

$$\overrightarrow{r}_i(t+\delta t) = \overrightarrow{r}_i(t) + \frac{\mathrm{d}\overrightarrow{r}_i(t)}{\mathrm{d}t}\delta t + \frac{1}{2}\frac{d^2\overrightarrow{r}_i(t)}{dt^2}\delta t^2 + \frac{1}{3!}\frac{d^3\overrightarrow{r}_i(t)}{dt^3}\delta t^3 + O(\delta t^4) \tag{2.4}$$

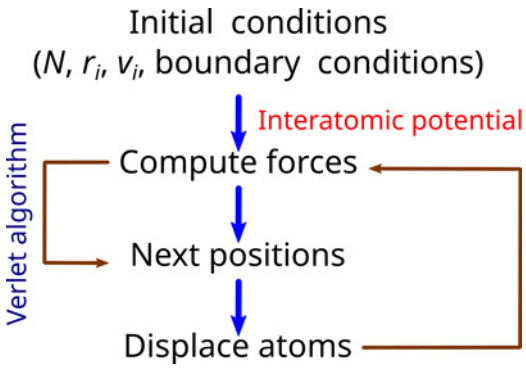

Figure 2.1: Classical MD workflow algorithm.

$$\overrightarrow{r}_i(t-\delta t) = \overrightarrow{r}_i(t) - \frac{\mathrm{d}\overrightarrow{r}_i(t)}{\mathrm{d}t}\delta t + \frac{1}{2}\frac{d^2\overrightarrow{r}_i(t)}{dt^2}\delta t^2 - \frac{1}{3!}\frac{d^3\overrightarrow{r}_i(t)}{dt^3}\delta t^3 + O(\delta t^4) \tag{2.5}$$

After simplification, the Verlet algorithm leads to,

$$\overrightarrow{r}_i(t+\delta t) = 2\overrightarrow{r}_i(t) - \overrightarrow{r}_i(t-\delta t) + \frac{d^2\overrightarrow{r}_i(t)}{dt^2}\delta t^2 + O(\delta t^4) \tag{2.6}$$

One can note that the Verlet algorithm does not require any atom velocity calculation as shown in Equation 2.6. An illustration of a classical MD workflow is illustrated Figure 2.1.

During MD, the kinetic energy E_{kin} and the temperature T are derived from the atom velocities,

$$T = \frac{2}{3}\frac{E_{kin}}{Nk_b} = \frac{1}{3Nk_b}\sum_i m_i\overrightarrow{v}_i^2 \tag{2.7}$$

MD simulations are performed within thermodynamic ensembles referred as NVE, NPT or NVT. The NVE ensemble allows for constant number of particles (N), volume (V) and energy (E). In the canonical ensemble NVT, the temperature can be controlled using various kinds of thermostat including the Nosé-Hoover thermostat that couples the system to an external T reservoir and makes use of a friction term ζ to hamper atomic displacements [HOO 96, NOS 02],

$$\frac{\mathrm{d}^2\overrightarrow{r}_i}{\mathrm{d}t^2} = \overrightarrow{F}_i/m_i - \zeta\frac{\mathrm{d}\overrightarrow{r}_i}{\mathrm{d}t} \tag{2.8}$$

$$\frac{\mathrm{d}\zeta}{\mathrm{d}t} = 1/Q_s(\sum_i m_i\overrightarrow{v}_i^2 - N_{df}k_bT) \tag{2.9}$$

with N_{df} the number of degrees of freedom of the system and Q_s mass.

An additional control on the pressure P is when using running MD simulations within the isothermal-isobaric (NPT) ensemble. Thermodynamically pressure is defined as,

$$P = \frac{N}{V} k_b T + \frac{1}{3V} \sum_i \overrightarrow{r_i} \cdot \overrightarrow{F_i} \tag{2.10}$$

where V is the volume of the silulation cell.

Using LAMMPS, various kinds of barostats (*e.g.*, Berendsen [BER 84], Nosé-Hoover [NOS 02]) can be coupled to the overall simulation cell volume based on a scalar pressure or to orthogonal and tilt directions (x, y, z, xy, xz and yz) using symmetric stress tensor. Other ensembles can also be used within LAMMPS as *e.g.*, the isenthalpic ensemble NPH [AND 80].

2.1.3 Boundary conditions and neighbor lists

Boundary conditions. When running atomistic simulations, it is necessary to define what boundary conditions to use in each direction of the simulation cell. Using LAMMPS, the boundary conditions (BCs) can be periodic (p style, referred later as PBCs) or free. PBCs allow the simulation cell to reasonably mimic an infinite system by replicating itself over given directions using periodic images. This treatment works perfectly well for highly ordered crystals. Various simulation cell shapes are available in the code. Among them, a triclinic-shape box covers the special cases of cubic, rectangular, rhombic dodecahedron, and truncated octahedron boxes.
In this thesis, we used PBCs when calculating α-alumina material properties such as lattice parameters or stacking fault energies but various non-periodic BCs are also defined within the LAMMPS code. These includes the f style for which simulation cell boundaries are fixed, the s style refers to boundaries set so as to encompass the atoms in a given direction (shrink-wrapping), no matter how far they move, and the m style includes constrained shrink-wrapping bounded by a value specified in the data file. Those specific BCs will be recalled later in the chapters dedicated to α-Al_2O_3 NPs compression tests in which the m style BCs were mainly used.

Cutoff and neighbor lists. When running atomistic simulations, the cutoff radius for short-range interactions between atoms cannot naturally exceed half of the box length and on the other hand, the number of interacting pairs in a system containing N particles is on the order of $O(N^2)$. Therefore, thinking about computational costs its obvious to mention that cpu costs would be quadrupled if the size of the system is doubled which is not desired for large-scale simulations. To speed up the simulation while maintaining a reasonable accuracy, the cutoff radius for short-range interactions is usually fixed at a constant value, and then the computational costs are linearly dependent on N. In a large

system where the size of the simulations box is much larger than the cutoff radius, the distances between particles will likely exceed the cutoff radius. In such case it becomes important to quickly and efficiently locate the interacting neighbors within the cutoff radius for each particle in order to reduce computational costs. Two main methods exist to search and find neighbors. The Verlet list method uses a less frequently updated neighbor list with a radius slightly larger than the cutoff radius, while the cell-list method divides the simulation box into many smaller cells so that the neighbors can be found in adjacent cells. For large systems the cell-list method is more efficient [HOW 16]. An other critical aspect related to the cpu costs is the kind of interatomic force model used in the simulation *i.e.*, the interatomic potential. This topic will be covered in the next section.

2.2 Interatomic potentials

In atomistic simulations, interatomic potentials are at the roots of atoms interactions since they describe the atomic bond features. They can just rely on simple analytical formulations or on more complex quantum-based equations. In this section we will recall the basics of the various of types of interatomic potentials used in this thesis to describe atomic bonds in α-alumina as well as the Embedded-Atom Method (EAM) formalism, commonly used to describe the metallic bound used in this work to model zirconium (an standard HCP metal) for comparison.

2.2.1 Rigid ion potential

The RI model was introduced by Catlow to describe atoms interactions in metal oxides such as UO_2 [CAT 77]. The general formulation of the RI potentials is provided in Equation 2.11. The first two terms rely on a so-called Buckingham potential [BUC 38, RIC 54] that is a short range interactions term mainly for van der Waals interactions while the third one is a long-range Coulomb interaction.

$$V_{ij}(r_{ij}) = A_{ij}exp(\frac{-r_{ij}}{\rho_{ij}}) - \frac{C_{ij}}{r_{ij}^6} + \frac{q_i q_j}{4\pi\varepsilon_0 r_{ij}} \tag{2.11}$$

with A_{ij}, ρ_{ij} and C_{ij} are fitted parameters, r_{ij} is the distance between ij pairs of atoms and q_i, q_j the respective atom charges.

RI potentials are fixed charged potentials *i.e.,* a constant charge is associated to each ion during the whole simulation run. This net charge can be different from the theoretical (or experimental) one and is often integrated in the fitting procedure. In this study, short-range interactions are computed in the real space for $r_{ij}<r_c$, with r_c a short-range cutoff radius. In the following, we use r_c=12 Å as it is the shortest common cutoff value

applicable to all the RI potential tested [GAL 92]. On the other hand, long-range interactions are computed using either the Ewald [EWA 21] (with long-range radius r_s=r_c), the Wolf [WOL 99]) or the Multi-level Summation Method (MSM) [HAR 06, HAR 09]. More details about charge summation will be provided later. Here we investigate the RI parameterizations of Bush *et al.* [BUS 94], Catlow *et al.* [LEW 85], Gale *et al.* [GAL 92] and Sun *et al.* [SUN 06], the later being a modified version of the original Matsui potential [MAT 96]. RI potentials parameters are provided in table 2.1.

		Bush	**Catlow**	**Gale**	**Sun**
Al-O	A(eV)	2409.505	1460.3	3596.94	3411.118
	ρ(Å)	0.2649	0.29912	0.23650	0.244549
	C(eV.Å^6)				
O-O	A(eV)	25.41	22764.3	435.63	91.55955
	ρ(Å)	0.6937	0.1490	0.36070	0.547148
	C(eV.Å^6)	32.32	27.879	0.49	32.32
Al-Al	A(eV)			9830.51	
	ρ(Å)			0.28870	
	C(eV.Å^6)			675.70	
Al^{+q} (e)		3	3	2.25	3
O^{-q} (e)		2	2	1.5	2

Table 2.1: RI potential parameters for α-alumina from Bush *et al.* [BUS 94], Catlow *et al.* [LEW 85], Gale *et al.* [GAL 92] and Sun *et al.* [SUN 06].

For the Catlow potential, short-range interaction parameters are derived from experimental lattice and elastic constants, dielectric constants, cohesive energy using least-squares fitting routines. The O-O interaction is taken from [CAT 77], Al-Al interactions are purely coulombic and the short-range attractive r^{-6} interaction is ignored for Al-O. Catlow potentials are the origin of fully-ionic models and were originally developed to investigate cohesive, elastic and lattice dynamics properties of oxides and halides.
The parameters of the Gale potential (Mulliken reference III) were derived from an *ab initio* periodic Hartree-Fock method applied to an energy hypersurface [GAL 92]. In addition, they used the Mulliken energy obtained at the minimum energy conformation to set partial charge values. The charge of aluminium changes up to 0.3e due to lattice distortion leading to electrostatic energy variations included into the short range interaction term.
RI Bush Buckingham term parameters are fitted using least-squares on experimental data including crystal structures, relative permitivities and elastic constants for a large set of metal compounds. For parts of them, phonon spectra are also included into the fit. Based on the authors comments, this fitting approach is supposed to capture the optimal potential for a single compound. Starting with the last optimised structure obtained during the

early stages of the fitting process, it avoids to trap in an undesirable local minimum. In Bush study, all fitting procedures are performed with the General Utility Lattice Program (GULP) [GAL 97].
The Sun potential relies on a simplified version of the original Matsui model built to investigate crystal structures and bulk moduli of CaO-MgO-Al_2O_3-SiO_2 systems (CMAS) [MAT 96]. After simplification, the authors readjusted the potential also using the GULP code [GAL 97]. One can note that the authors biased the weighting factors to better assess the lattice parameters at the expense of the elastic constants. The lattice energy was also included in the fitting procedure (but with a low weight). Their results show that neither the van der Waals terms involving cations nor the short-range cation–cation interactions need to be included in the simulations in order to obtain an acceptable reproduction of the experimental data.

2.2.2 2/3-body interatomic potentials

Biswas *et al.* firstly developed 2/3-body interatomic potential to reproduce structural energies of silicon [BIS 85]. Originally, the potential was fitted on a Density-Functional Theory (DFT) database including the energies of various silicon structures. 2/3-body potentials were originally introduced as a simplification of the 3-body formalism *i.e.*, reducing the 3-body energy to a product of 2-body sums that simplifies energy and atomic forces computation from n^3 steps to n^2 with n the number of atoms in the system. In the original study of Biswas, the 2/3-body interatomic potential is defined as follow,

$$V_{ijk}(r_{ij}, r_{ik}, \theta_{ijk}) = 1/2 \sum_{i,j} V_{ij}^{(2)}(r_{ij}) + \sum_{i,j,k} V_{ijk}^{(3)}(r_{ij}, r_{ik}, \theta_{ijk}) \tag{2.12}$$

with r_{ij} and r_{ik} the two lengths between respective pairs of atoms and θ_{ijk} the angle between the triplet of atoms.

The pair term $V_{ij}^{(2)}$ relies on a short-range Morse potential form [MES 98],

$$V_{ij}^{(2)}(r_{ij}) = D_{ij}[1 - e^{-\alpha(r_0 - r_{ij}}]^2 \tag{2.13}$$

where D_{ij} and α are constants with dimensions of energy and reciprocal distance, and r_0 is the equilibrium distance between the two atoms.

$V_{ijk}^{(3)}$ is defined by a bond length function F_ι multiplied by linear coefficients C_ι,

$$V_{ijk}^{(3)} = \sum_{\iota} C_\iota F_\iota(r_{ij}, r_{ik}) P_\iota(cos(\theta_{ijk})) \tag{2.14}$$

where $F_\iota = \phi_\iota(r_{12})\phi_\iota(r_{13})$, with ϕ_ι the symmetric products of functions of each bond length. The 3-body term $P_\iota(cos(\theta_{ijk}))$ relies on the angular interaction between triplets

of atoms. ι is the parameter of bond length.

F_ι allows to reduce the 3-body energy to a rotationally invariant scalar product of vectors ϕ_ι. ϕ_ι is indeed made of simple 2-body sums based on spherical harmonics and atomic bonds.

$$\sum_{i,j,k} V_{ijk}^{(3)}(r_{ij}, r_{ik}, \theta_{ijk}) = \sum_{\iota} C_\iota \left[\frac{4\pi}{2\iota+1}\right] \sum_{m=-\iota}^{+\iota} \Phi_{\iota m}^{ij} \Phi_{\iota m}^{ik} - \sum_{ij} f_{ij}(r_{ij}) \tag{2.15}$$

$$f_{ij}(r_{ij}) = \sum_{\iota} C_\iota \phi_\iota^2(r_{ij}) \tag{2.16}$$

where $\Phi_{\iota m}^{ij}$ vectors are the moments of the structure around atoms i and j that accounts for local environment. $f_{ij}(r_{ij})$ present the monotonic functional form of the 3-body potential.

Later, Vashishta *et al.* adapted the 2/3-body formalism into two-body and three-body covalent interactions [VAS 90]. Their potential is developed to study structural and dynamical correlations of crystalline, molten, and vitreous states of SiO_2 materials under various conditions of density and temperature. In the M_xN_y-type materials (M= Si, Al, Ge or In and N= O, P, S, Se or Te), the charge transfer from M atom to N atom forms cations M^{a+} and N^{b-} ions what in general results in smaller M^{a+} than N^{b-}. Hence, the two-body term includes the steric repulsion due to atom size and charge transfer (within the Coulomb term). Also charge-dipole interactions arise from the effects of large electronic polarizability of anions.

The Branicio formulation of the Vashishta potential used within the LAMMPS code is similar to Equation 2.12. The two-body part $V_{ij}^{(2)}(r_{ij})$ includes steric-size effects, charge-induced dipole, Coulomb and van der Waals interactions. It applies up to a cutoff distance of r_c= 6 Å.

$$V_{ij}^{(2)}(r_{ij}) = \frac{H_{ij}}{r_{ij}^{\eta_{ij}}} + \frac{q_i q_j}{r_{ij}} e^{(-r_{ij}/\lambda_{1,ij})} - \frac{D_{ij}}{r_{ij}^4} e^{(-r_{ij}/\lambda_{4,ij})} - \frac{W_{ij}}{r_{ij}^6}, r_{ij} < r_c \tag{2.17}$$

where H_{ij} and η_{ij} are respectively the strength and the size exponent of the steric repulsion, λ_1 and λ_4 are the screening lengths of the Coulomb and the charge-induced dipole interactions. D_{ij} and W_{ij} are the strengths of both the charge-induced dipole and the van der Walls interactions, respectively.

In comparison to RI, the 2/3-body potential developed by Vashishta better accounts for covalent features such as bound directionality thanks to the angular term derived from the Stillinger-Weber potential [STI 85],

$$V_{ijk}^{(3)}(r_{ij}, r_{ik}, \theta_{ijk}) = B_{ijk} \frac{\left[\cos\theta_{ijk} - \cos\bar{\theta}_{ijk}\right]^2}{1 + C_{ijk}\left[\cos\theta_{ijk} - \cos\bar{\theta}_{ijk}\right]^2} \times e^{\frac{\gamma}{r_{ij}-r_0}} e^{\frac{\gamma}{r_{ik}-r_0}}, r_{ij} \leq r_0, r_{ik} \leq r_0 \quad (2.18)$$

with B_{ijk} is the amplitude of the 3-body interaction. θ_{ijk} is the angle between vectors $\vec{r}_{ij}$ and $\vec{r}_{ik}$. r_{ik} is the distance between ik pairs of ions. $\bar{\theta}_{ijk}$, C_{ijk} and γ are the parameters of the 3-body interaction that ranges up to r_0.

When applied to alumina, Vashishta *et al.* used a unique radial term for both Al-O-Al and O-Al-O triplets but two different angular terms. Also, the prefactor B_{AlOAl} and B_{OAlO} are different [VAS 08]. Vashishta potential parameters for α-alumina are recalled Table 2.2.

	Al	O	
q(e)	+1.5237	-1.0158	
	Al-Al	Al-O	O-O
λ_1(Å)		5.0	
λ_4(Å)		3.75	
r_c(Å)		6.0	
η_{ij}	7.0	9.0	7.0
H_{ij}(eV.Å$^\eta$)	12.7506	249.3108	564.7334
D_{ij}(eV.Å^4)	0.0	50.1522	44.5797
W_{ij}(eV.Å^6)	0.0	0.0	79.2884
	Al-O-Al	O-Al-O	
B_{ijk}(eV)	8.1149	12.4844	
cos($\bar{\theta}_{ijk}$)	-0.33331	0.0	
γ(Å)		1.0	
r_0(Å)		2.90	
C_{ijk}		10.0	

Table 2.2: 2/3-body Vashishta interatomic potentials parameters for Al_2O_3 [VAS 08].

2.2.3 SMTB-Q potential

The SMTB-Q interatomic potential is a variable charge model originally developed by Tétot *et al.* [TÉT 08]. It is based on the charge equilibration (QEq) method that allows for local ionic charge variations based on the electronegativity equalization principle of Rappé *et al.* [RAP 91]. While it is the most complex interatomic potential used in this study,

it is also the closest to the original quantum theory as it uses the quantum description of insulating oxides [GON 94]. The SMTB-Q formalism is used in the following mostly as a reference *i.e.*, to confront outcomes from RI and 2/3-body potentials. Up to now, it has been successfully used to investigate Al_2O_3 polymorphs phase properties under pressure as well as Al_2O_3 cluster and nanocrystals stability [TÉT 13, SAL 16, LAU 20]. The SMTB-Q model was also used to investigate lattice and mechanical properties of UO_2 and ZrO_2 in good agreement with experimental data [TÉT 08, MBO 19]. In the SMTB-Q framework, the total cohesive energy is described as follows,

$$E_{coh} = E_{ion} + E_{coul} + E_{cov} + E_{rep} \tag{2.19}$$

with

$$E_{ion} = \sum \left(E_i^0 + \chi_i^0 q_i + 1/2 J_{ii}^0 q_i^2 \right) \tag{2.20}$$

$$E_{coul} = \sum_i \sum_{i<j} q_i q_j J_{ij} \tag{2.21}$$

$$E_{cov}^{i,j(i,j=Al,O)} = -\sum \left\{ \sum_{r_{ij} \leq r_c} \epsilon_i^2 exp \left[-2\zeta (\frac{r_{ij}}{r_0} - 1) \right] \Delta q_i \right\}^{1/2} \tag{2.22}$$

$$\begin{aligned} E_{rep}^{i,j(i,j=Al,O)} = & \sum_{r_{ij} \leq r_c}^{i} \sum_{r_{ji} \leq r_c}^{j} A_{ij} exp \left[-p_{Al} (\frac{r_{ij}}{r_0}) - 1 \right] (Al - O) \\ & + 1/2 \sum^{j} \sum_{r_{jj} \leq r_c}^{j} B exp (\frac{r_{jj}}{\rho}) (O - O) \end{aligned} \tag{2.23}$$

where E_{ion} is the second order ionization energy of the atom i defined using the neutral atom energy E_i^0, the electronegativity χ_i^O and the hardness J_{ii}^O, respectively. E_{coul} is the electrostatic term with J_{ij} an integral coulomb term computed using two s-type Slater orbitals (see Ref. [RAP 91] for more details). E_{cov} is a covalent energy term that apply up to the second moment radius r_c^{2nd} located between the 4^{th} and 5^{th} neighbors of each Al and O atoms [GON 94]. ϵ_i and ζ are the hopping integral adjustable parameters (see Ref. [TÉT 13] for more details). Δq_i refers to the covalent contribution of the delocalized electronic charges. Finally, E_{rep} is a short-range interaction term acting between ions where p_{Al} and B are adjustable parameters. Cation–cation short-range interactions (repulsive terms) are neglected because the M outer orbitals are empty in an insulator. In this study, the charge summation within SMTB-Q is performed using the Wolf summation method [WOL 99]. Parameters of the SMTB-Q interatomic potential for α-alumina are provided in Table 2.3.

χ^0_O (eV)	6.57	β_{Al} (eV)	0.7096
J^0_{OO} (eV)	10.22	ζ	1.5885
χ^0_{Al} (eV)	1.19	ϵ	0.1818
χ^0_{AlAl} (eV)	11.19	A_{ij} (eV)	8.8004
R_O (Å)	0.529	r_0 (Å)	1.91
R_{Al} (Å)	0.566	B (eV)	580.44
β_O (eV)	0.5794	ρ (Å)	0.354

Table 2.3: SMTB-Q interatomic potential parameters for α-Al_2O_3 [SAL 16].

2.2.4 The embedded-atom method

Daw *et al.* developed the EAM to compute ground-state properties of metal and alloyed systems [DAW 84]. In the EAM framework, the energy of the atom i is defined using the concept of embedding energy,

$$E_i = F_\alpha \sum_{i \neq j} \rho_\beta(r_{ij}) + \frac{1}{2} \sum_{i \neq j} \phi_{\alpha\beta}(r_{ij}) \tag{2.24}$$

where F_α is the embedding function *i.e.*, the energy required to put atom i (of type α) into the electron cloud, ρ_β is the contribution from atom j (type β) to the electron charge density at the atom i position and $\phi_{\alpha\beta}$ is a pair potential function.

The EAM method is the most commonly used method to compute metal properties. In this thesis, it is used to calculate zirconium properties using the Mendelev potential [MEN 07] for a direct comparison to α-Al_2O_3. Indeed, both materials have the same HCP crystalline structure and preliminary calculations on Zr (*e.g.*, for stacking faults) in addition to a comparison to the literature allows for a better understanding of alumina specifc features.

2.3 Companion tools

2.3.1 ATOMSK

ATOMSK is a command-line tool developped by Hirel [HIR 15]. It can be used to create and manipulate atomic systems for the purposes of *ab initio*, MS and MD simulations. ATOMSK is able to handle several file formats and allow for straightforward conversion of atomic configuration files. In addition to the creation of perfect crystal supercells, ATOMSK allows for the insertion of point and line defects, cracks, planar defects (stacking faults), deformation or transformation of simulation cells. The ATOMSK software can be downloaded here: `https://atomsk.univ-lille.fr/dl.php`.

In this thesis, several options of ATOMSK were used to prepare simulation cells. For example, the option *orthogonal − cell* was used to build α-Al_2O_3 orthogonal supercells, the option *rotate* was used to orient simulation cells (*e.g.*, for stacking fault calculation). ATOMSK was also used to build part of the alumina NPs we have investigated.

2.3.2 OVITO

OVITO is a scientific data visualization and analysis software for molecular and other particle-based simulations [STU 09]. It is developed by OVITO GmbH, a Germany-based spin-off founded by Stukowski, the original developer of the software. The software is developed using object-oriented C++. It is controlled either using a simple and plug-and-play interface or via Python scripts. OVITO can be downloaded at : `https://www.ovito.org`.

In this thesis, OVITO is used as the main tool to analyze results of MS/MD simulations, get 2D/3D images and make simulation movies. Several functions of OVITO are applied to atomic datasets including *e.g.*, the Ackland-Jones analysis designed to identify crystalline structures for each atom based on local environment analysis [ACK 06]. The Dislocation Extraction Algorithm (DXA) was also used to characterize dislocations and determine their Burgers vectors [STU 10]. The displacement vectors analysis was often used to identify local shear events while the coordination analysis was used to compute the Radial Distribution Function (RDF) in some systems, as *e.g.,* during the preparation of α-Al_2O_3 NPs.

Chapter II summary:
The chapter II focuses on methods. First, we have introduced atomistic simulation methods (MS and MD) within the LAMMPS framework as well as the various theoretical backgrounds related to the interatomic potentials we will use to model α-Al_2O_3 properties. Then, companion tools ATOMSK and OVITO used to respectively generate samples and present simulations outcomes were described.

Chapter 3

Transferability of interatomic potentials to nanomechanics in α-alumina

In this chapter, we test several interatomic potentials available from the literature for α-Al_2O_3. The main goal is to confront the various formalisms presented previously such as the RI, 2/3-body and variable charge interatomic potentials and verify their transferability to nanomechanical simulations in α-alumina. For this purpose, several material properties including lattice parameters, elastic constants, stacking fault and dislocation properties are investigated and compared to relevant DFT simulations and up-to-date experiments available in the literature.

3.1 Unit cell, lattice parameters and elastic constants

3.1.1 Methods

α-Al_2O_3 is a iono-covalent ceramic often described by a 30 atoms hexagonal unit cell with lattice parameters a_0=4.76 Å and c_0=12.99 Å [SNO 73]. In this study, an orthorombic unit cell made out of 60 atoms is used for modeling convenience. It is characterised by cell vectors of lengths $a = a_0$, $b = \sqrt{3}a_0$ and $c = c_0$. Both unit cells are shown Figure 3.1.

A 3×3×3 orthogonal supercell is designed for the calculation of α-Al_2O_3 lattice parameters using PBCs. First, the CG is used to minimize the potential energy of the system with a stopping criterion of 10^{-4} eV/Å . Second, an anisotropic relaxation is performed down to zero pressure changing box dimensions and remapping atom positions. Finally, the energy and resulting forces of the system are further minimized (without allowing box relaxation) using the FIRE algorithm down to a net force of 10^{-6} eV/Å for RI and

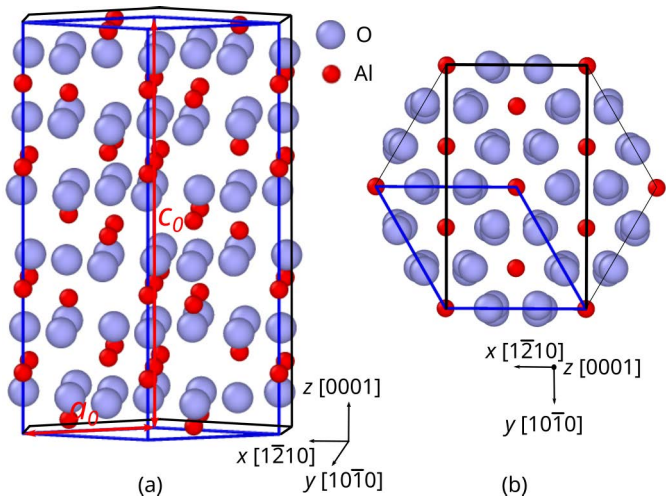

Figure 3.1: Crystal structure of α-Al_2O_3 (a) 3D view, (b) Projected view along [0001]. The black and blue lines refer to the hexagonal (30 atoms) and orthogonal (60 atoms) cells, respectively.

2/3-body interatomic potentials and 10^{-4} eV/Å for SMTB-Q.

Interatomic potential		**Lattice parameter (Å)**	
		a_0	c_0
Rigid ion	Bush	4.82	13.01
	Catlow	4.78	12.57
	Gale	4.76	12.99
	Sun	4.77	12.99
2/3-body	Vashishta	4.72	13.17
Variable charge	SMTB-Q	4.81	13.06
DFT			
Ref.[LEI 13, MAR 01]		4.75±0.06	13.05±0.15
Experiment			
Ref.[GIE 68, ISH 80]		4.75±0.01	12.99±0.01

Table 3.1: α-Al_2O_3 lattice parameters a_0 and c_0 computed using Bush, Catlow, Gale and Sun RI [BUS 94, GAL 92, LEW 85, SUN 06], Vashishta 2/3-body [VAS 08] and SMTB-Q [SAL 16] interatomic potentials. Experimental [GIE 68, ISH 80] and DFT [MAR 11, LEI 13] data are shown for comparison.

Then we compute the elastic constants (C_{ij}). The C_{ij} characterize the stiffness of a material. They link stress and strain tensors via the generalised Hooke's law $\sigma_i = C_{ij}\epsilon_j$. Due to the hexagonal crystal symmetry, the α-Al_2O_3 stiffness matrix is defined by 6 independent elastic constants only *i.e.*, C_{ij}=($C_{11}, C_{12}, C_{13}, C_{14}, C_{33}, C_{44}$).

$$\begin{bmatrix}\sigma_1\\ \sigma_2\\ \sigma_3\\ \sigma_4\\ \sigma_5\\ \sigma_6\end{bmatrix} = \begin{bmatrix}C_{11} & C_{12} & C_{13} & & & \\ C_{12} & C_{11} & C_{13} & & & \\ C_{13} & C_{13} & C_{33} & & & \\ & & & C_{44} & & \\ & & & & C_{44} & \\ & & & & & C_{66}\end{bmatrix} \begin{bmatrix}\varepsilon_1\\ \varepsilon_2\\ \varepsilon_3\\ 2\varepsilon_4\\ 2\varepsilon_5\\ 2\varepsilon_6\end{bmatrix} \tag{3.1}$$

So,

$$\begin{cases}\sigma_1 = C_{11}\varepsilon_1 + C_{12}\varepsilon_2 + C_{13}\varepsilon_3\\ \sigma_2 = C_{12}\varepsilon_1 + C_{11}\varepsilon_2 + C_{13}\varepsilon_3\\ \sigma_3 = C_{13}\varepsilon_1 + C_{13}\varepsilon_2 + C_{33}\varepsilon_3\\ \sigma_4 = 2C_{44}\varepsilon_4\\ \sigma_5 = 2C_{44}\varepsilon_5\\ \sigma_6 = 2C_{66}\varepsilon_6\end{cases} \tag{3.2}$$

C_{ij} are computed at 0K modeling the stress response under applied respective strains using Equations 3.2. This process is illustrated Figure 3.2. For example, a strain ε_1 along the direction X_1 is applied to the system (while keeping the other strain components null) to compute C_{11} evaluating σ_1 stress response using the first relation in Equation 3.2. A same approach is used for tensile modulus, applying tensile as in the case of $C_{44} = \sigma_4/2\varepsilon_4$ (see Figure 3.2b). For this purpose, a relaxed 3×3×3 supercell is iteratively deformed using PBCs along the appropriate directions. Then, stress tensor variations are computed minimizing the system energy (without shape changes) using the FIRE algorithm [BIT 06] down to a net force of 10^{-6} eV/Å for RI and 2/3-body interatomic potentials and 10^{-4} eV/Å for SMTB-Q.

3.1.2 Results

Table 3.1 shows that all the interatomic potential tested reproduce quite well the two lattice parameters when compared to DFT and experiments except the Catlow RI potential that underestimates c_0 (12.57 Å) when compared to average 13.05 Å and 12.99 Å respectively for DFT and experiments. Results are more critical for elastic constants calculations as shown Table 3.2, where RI Bush, Catlow and Sun potentials are particularly off when compared to literature data. Indeed, RI potentials are not accurate enough here except the Gale potential which provides slightly better results. On the other hand, 2/3-body Vashishta and SMTB-Q potentials provide more accurate results. On this basis, we conclude that the RI Gale [GAL 92], the 2/3-body Vashishta [VAS 08] and the SMTB-Q [SAL 16] interatomic potentials are particularly suited to describe α-Al_2O_3 lattice properties. A particular attention will be paid to these three potentials in the following.

Interatomic potential		Elastic constants					
		C_{11}(GPa)	C_{12}(GPa)	C_{13}(GPa)	C_{14}(GPa)	C_{33}(GPa)	C_{44}(GPa)	C_{66}(GPa)
Rigid ion	Bush	662.2	271.9	180.7	59.6	608.9	132.8	195.2
	Catlow Gale	675.5	272.6	206.6	47.5	505.4	180.1	201.4
		560.3	263.6	220.4	17.3	460.6	170.0	148.4
	Sun	714.5	327.6	187.8	69.1	709.3	99.7	193.4
2/3-body	Vashsishta	476.1	155.4	135.4	10.4	414.9	149.1	160.3
Variable charge	SMTB-Q	498.9	202.2	152.0	37.9	457.4	115.0	145.5
DFT								
Ref.[JAH 06, SAR 13]		490.0±20.0	165.0±15.0	110.0±15.0	-25.0±5.0	500.0±40.0	150.0±20.0	162.5±20.0
Experiment								
Ref.[GIE 68, OHN 86]		495.0±5.0	163.5±0.5	115.0±5.0	-12.0±10	500.0±1.5	147.0±2.0	165.8±0.5

Table 3.2: α-Al_2O_3 elastic constants computed at 0K using RI [LEW 85, BUS 94, GAL 92, SUN 06], 2/3-body [VAS 08] and SMTB-Q [SAL 16] interatomic potentials. Experimental data from Ref. [GIE 68, OHN 86] and DFT data from Ref. [JAH 06, SAR 13] are shown for comparison. C_{66} is computed from the relation $(C_{11}$-$C_{12})/2$.

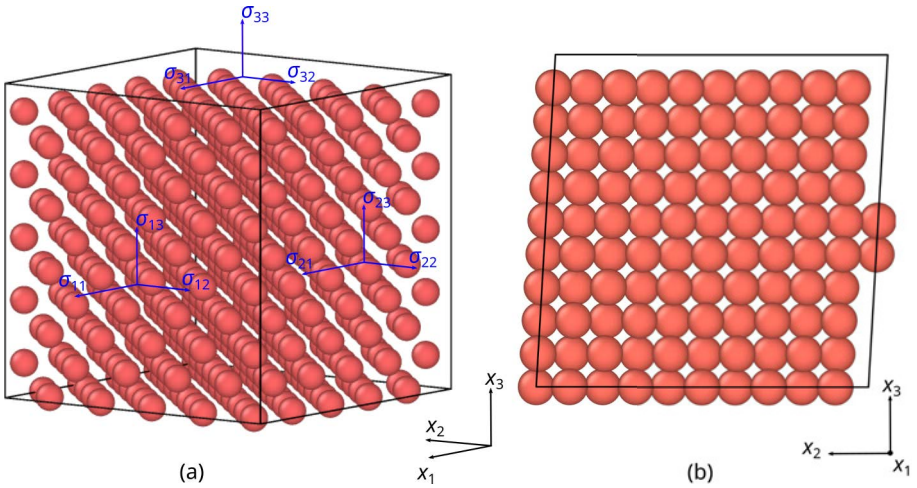

Figure 3.2: Elastic constants calculation (a) Simulation cell illustrating important surfaces and directions for the calculation of the strain and stress tensor components. (b) Example of deformation applied to compute shearing elastic constants.

3.2 Surface energy

α-alumina surfaces have attracted a significant attention especially in the field of catalysis, coatings and electronics [HAR 13, JIA 18, MUR 20]. Therefore, first-principle simulations on surface features were performed showing (0001) < $\{1\bar{1}02\}$ < $\{11\bar{2}0\}$ < $\{10\bar{1}0\}$ < $\{10\bar{1}1\}$ energy ranging that emphasizes the highest stability of the (0001) basal surface [MAR 04, SUN 06]. As shown Figure 3.3, the [0001] stacking of bulk α-Al_2O_3 obeys the following sequence ..-Al_2-O-Al_1-Al_2-O-.. with O a pure oxygen layer and Al_1 and Al_2 two pure aluminum layers shifted from each other. In the simulations, these three layers are often considered as first guesses to compute the (0001) surface energy. Guenard *et al.* have investigated the (0001) surface of α-alumina with single Al layer termination using grazing incidence X-ray scattering [GUE 98]. They conclude that surface Al layer is closer to the underlying O layer due to surface relaxation, when compared to bulk conditions. This result was confirmed by Walter *et al.* using dynamical low-energy electron diffraction and various sample surface preparation methods [WAL 00]. Wang and collaborators used DFT simulations and confirmed the stability of the Al-terminated basal surface, even under high oxygen partial pressure conditions [WAN 00a]. Finally, Blonski and collaborators performed molecular static simulations for three terminations of the (0001) surface (one O terminated and two Al terminated). After minimisation, the authors show similar results for the two Al-terminated surfaces with surface energies lower that in the O-terminated case [BLO 96].

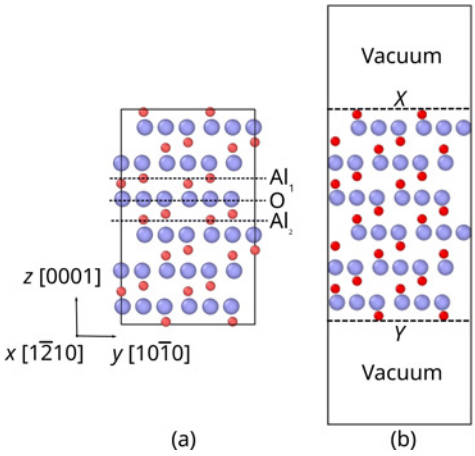

Figure 3.3: Slab-type supercell for basal surface energy calculation in α-alumina. The simulation relies on a collumnar supercell of Al_2O_3 oriented along the $[0001]$ direction. Red and blue atom refers respectively to aluminum and oxygen atoms. O, Al_1 and Al_2 layers are depicted by dashed lines. (a) Original supercell used for E_{bulk} calculation. (b) Supercell with vacuum out of X=Al_2 and Y=Al_1 free surfaces.

3.2.1 Methods

Generally, atomistic computation of surface energies rely on the use of a slab-type supercell with either 3D-PBCs and empty space out of the surface of interest (on the two sides X and Y, see Figure 3.3) or free-BCs along the surface direction together with 2D-PBCs for the two in-plane directions [ZU 15, GOR 15, YIN 17]. Then, the surface energy γ_s^{XY} is computed using Equation equation (3.3)

$$\gamma_s^{XY} = \frac{E_{slab}^{XY} - nE_{bulk}}{2A} \tag{3.3}$$

where E_{slab}^{XY} is the minimized potential energy of the simulation cell including XY-terminated surfaces, E_{bulk} is the per-atom minimised energy of the bulk material, n is the number of atoms contained in the slab and A is the slab cross-section area.

In simple structures (*e.g.*, FCC monoatomic metals), the two opposite side surfaces of a simulation supercell can be identical (X=Y) what makes the surface energy calculation straightforward. However, in more complex cases, surfaces can be hetero-terminated ($X \neq Y$) when the crystal structure is defined by alternating plans along the surface stacking direction. In this later case, the surface energy can be averaged (γ_s^{ave}) accounting for the two different surfaces (as *e.g*, in the case of $L1_2$ crystal $\{100\}$ surface energy). In α-alumina, most of the crystallographic planes alternates with a period larger than two leading to a more complex definition of γ_s^{ave} (especially when no energetically favoured surface is identified). Obviously, one could force the X=Y terminations by slicing the simulation supercell whatever the crystalline structure. However, this generally leads to

non-stoichiometric configurations in ionic materials that are out of reach for most of classical charge summation algorithms.

Here we design slab simulations that refer to the three possible terminations of the (0001) surface in α-alumina *i.e.*, XY=Al_1O, Al_1Al_2 or OAl_2 (see Figure 3.4a and b) in order to solve a derived set of surface energy equations. A this stage, one can anticipate that Al_1O and OAl_2 simulations should lead to same results as both Al basal surface terminations rely on the same atomic arrangement only shifted one from each other. However, we preferred to keep the both at this stage for a sake of clarity. Supercells were made out of $3{\times}3{\times}n_z$ unit cells. First, the simulation cell is relaxed (force norm limit of 10^{-6} eV/Å for RI and 2/3-body, 10^{-4} eV/Å for SMTB-Q) using 3D-PBCs to compute E_{bulk}, then the box dimension is extended twice along the [0001] direction (without remapping atomic positions) to introduce vacuum and compute E_{slab}^{XY} using the same minimization protocol and 3D-PBCs as illustrated Figure 3.3. The Ewald, Wolf and MSM charge summation methods are compared in the case of the RI Gale interatomic potential. A long-range radius varying from 12 to 24 Å was tested also for this potential without significant changes on the conclusions. A relative accuracy of 10^{-6} is set for both Ewald and MSM. n_z ranging from 3 to 21 was tested to investigate possible electrostatic interactions between free surfaces without significant impacts on the results. Finally, γ_s^{XY} is computed for each XY case using Equation equation (3.3) and single-surface energy γ_s^i, *i.e.*, $\gamma_s^{Al_1}$, $\gamma_s^{Al_2}$ and γ_s^O, are derived using Equation equation (3.4).

$$\gamma_s^{ii} = \gamma_s^{ij} + \gamma_s^{ik} - \gamma_s^{jk} \tag{3.4}$$

where i, j and k refer to the three different terminations.

3.2.2 Results

Figure 3.4 illustrates α-Al_2O_3 basal-surface configurations before and after simulation for the various surface terminations. Al_1Al_2 simulations show comparable relaxed configurations whatever the potential or charge summation method used with both Al surface-ending layers about to merge with their O respective sublayer (Figure 3.4c) as already observed in Refs. [TEP 00, RUB 03, KUR 10, SAL 16]. However, significant surface reconstruction is observed in the Al-double layer surface region of Al_1O and OAl_2 simulations as shown Figure 3.4e,f,g while the opposite O-single layer surface is more stable during the simulation. One can notice that Vashishta and SMTB-Q potentials lead to similar surface reconstruction processing within the Al-double layer surface region where one of the first two Al layers migrates below the first O layer. Furthermore, the Gale potential shows results that depend on the charge summation method used *i.e.*, Ewald, Wolf and MSM. On one hand, the Wolf method leads to a qualitatively similar surface

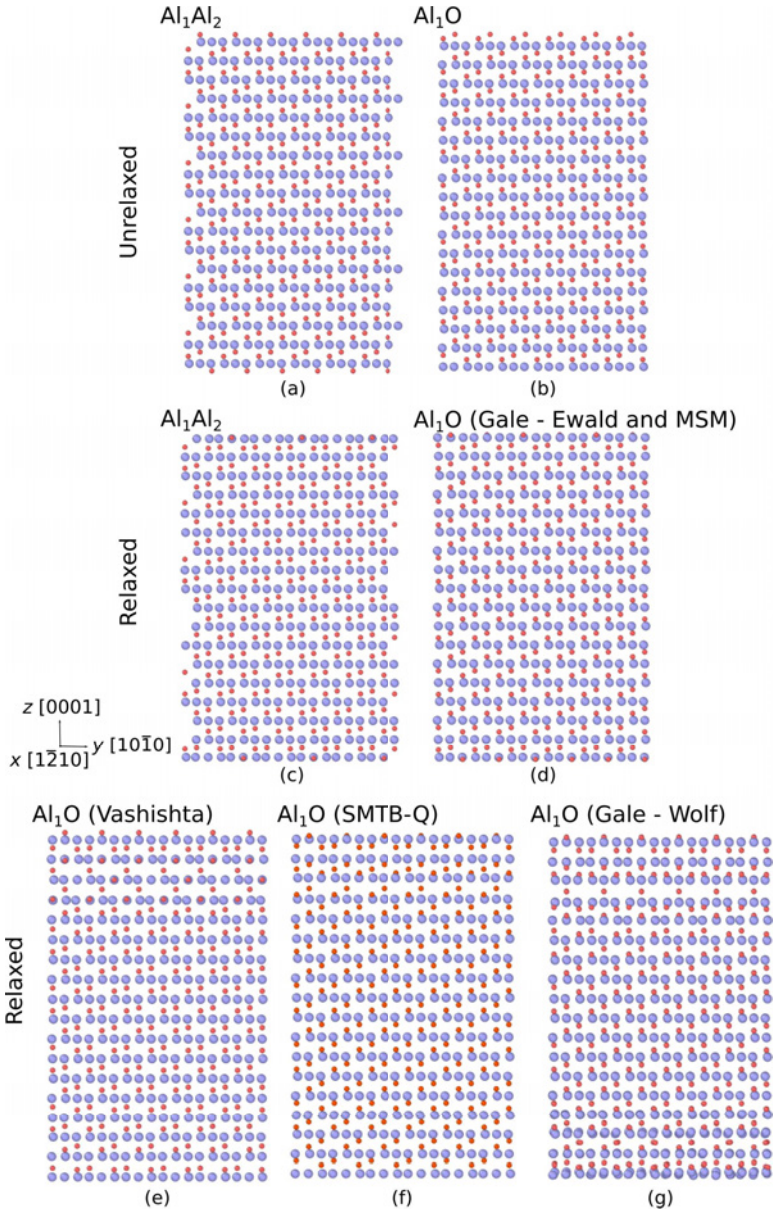

Figure 3.4: α-Al_2O_3 basal surface energy simulation (n_z=3). (a,b) Unrelaxed simulation cell for Al_1Al_2- and Al_1O-terminations as examples, (c) Al_1Al_2 relaxed configuration (Vashishta), (d) Al_1O relaxed configuration computed with Gale potential using the Ewald summation method, (e,f,g) Al_1O relaxed configuration using respectively (e) Vashishta, (f) SMTB-Q and (g) Gale (Wolf method) interatomic potentials. Aluminum atoms are depicted in red while oxygen atoms are colored in blue.

reorganization process than when using Vashishta or SMTB-Q potentials *i.e.*, surface reconstruction only in Al-double layer surface region (Figure 3.4d). However, the surface reconstruction details are different when compared to the two aforementioned potentials (see Figure 3.4g in comparison to 3.4e and 3.4f) and, moreover, the surface O-single layer is more desorganized including three consecutive Al layers over it instead of two in the Vashishta and SMTB-Q cases. Finally, the O-terminated region reconstructs when using Ewald or MSM in the same way than in the Al_1O and OAl_2 cases *i.e.*, only the Al-single layer configuration with an energy of about 4.1 J/m^2 can be stabilized in this case (Figure 3.4d).

Surface energies are provided in Table 3.3. As expected, $\gamma_s^{Al_1}$ and $\gamma_s^{Al_2}$ computed using Equation 3.3 are very close with variations only due to the interatomic potential used. Al_1O and OAl_2 simulations show particularly large energy values when compared to the more stable Al_1Al_2 configuration due to surface oxygen atoms. Finally, results provided by Vashishta and SMTB-Q interatomic potentials are in good agreement with DFT data for comparable terminations [SIE 02, KUR 10, CHO 15]. In particular, values obtained using SMTB-Q for the Al-terminated surface are in good agreement with the one of Salles *et al.* (1.89 J.m^{-2}) computed using the same interatomic potential [SAL 16]. While the SMTB-Q model shows a quantitative agreement with DFT results, the Vashishta potential overestimates the γ_s^O while keeping γ_s^{Al} in a good range. Overall, one can conclude that the Vashishta potential is still in qualitative agreement with DFT outcomes as it confirms both $\gamma_s^O > \gamma_s^{Al}$ and the energy increase induced by O atoms in the case of Al-double layer reconstructed surfaces. The Vashishta potential ability to reproduce the complex Al-double layer surface reconstruction in a similar manner than the more complex SMTB-Q reinforces the transferability of the potential to surface properties albeit its simple formulation. On the contrary, the Gale potential provides way larger surface energies when compared to the other two potentials and DFT data.

Interatomic potential		**Surface energy (J.m^{-2})**		
		γ_s^O	$\gamma_s^{Al_1}$	$\gamma_s^{Al_2}$
Rigid ion	Gale	14.25	3.65	3.65
2/3-body	Vashishta	7.10	1.67	1.67
Variable charge	SMTB-Q	3.48	1.83	1.85
DFT				
Ref. [TEP 00, MAR 04, KUR 10]		3.98±0.48	1.92±0.27	

Table 3.3: (0001) surface energy in α-Al_2O_3 computed using the RI Gale potential [GAL 92] with Wolf charge summation method, the 2/3-body Vashishta [VAS 08] and the SMTB-Q [SAL 16] interatomic potentials. Averaged DFT data computed from Ref. [TEP 00, MAR 04, KUR 10] are shown for comparison.

3.3 Stacking faults energy

3.3.1 Methods

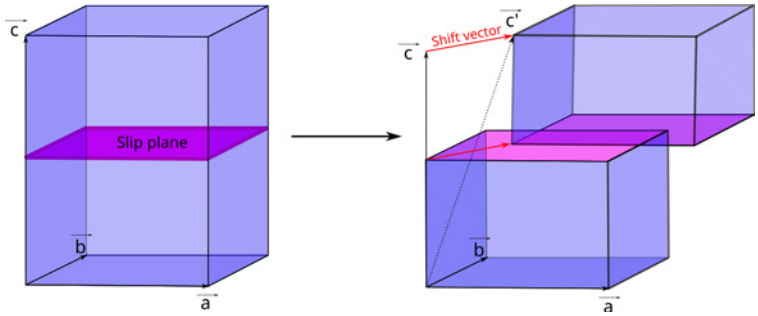

Figure 3.5: Stacking fault simulation methodology. The upper part of a collumnar supercell is shifted to generate a stacking fault. The supercell vector normal to the faulted plan (here $\vec{c}$) is tilted to ensure PBCs remapping the atoms out of the box.

Due to its intrinsic link with plastic deformation and mechanical properties, Generalised Stacking Fault Energy (GSFE) is one of the main lattice property to analyse when investigating the transferability of interatomic potentials to nanomechanics. The concept of stacking fault was first introduced by Vitek [VIT 68] and is now used in several atomic-scale plasticity models including dislocation or twin nucleation [CHE 03, VAN 04], dislocation core Peierls-Nabarro modeling [PEI 40, NAB 47] and ductile fracture modeling [RIC 74].

The basic method to compute GSFE (also called γ^{sf} in the following) is to build a collumnar orthogonal supercell with the longer direction normal to the faulted plane of interest (see Figure 3.5). Then, atoms contained in the upper half of the supercell are shifted along an in-plane direction leading to a planar fault and are then allowed to relax only normally to the stacking fault. Owing the perfect collumnar cell as a reference, γ^{sf} is defined as the energy variation normalised by the in-plane section area of the supercell,

$$\gamma^{sf} = \frac{E_f - E_0}{A} \tag{3.5}$$

where E_0 is the reference energy of the simulation cell, E_f is the energy after the stacking fault is produced and A is the cross-section area of the simulation cell.

In this study, we allow supercell vectors tilting using a triclinic box to conserve 3D-PBCs along the whole simulation procedure. The simulation is performed using an iterative process, including either the calculation of Stacking Fault Energies (SFEs) along a single direction (the energy *vs.* displacement curve is thus called a γ-line) or along an entire crystallographic plane leading to an energy map called γ-surface. Energy minimizations are performed using a force norm criterion of 10^{-6} eV/Å when using Vashishta potential

and 10^{-4} eV/Å for SMTB-Q and Gale potentials. Results exhibit excess energy, possibly including local minima referred as stable Stacking Fault Energy (sSFE). Generally, shifts are produced iteratively from one to the next equivalent atomic position. During crystal plastic deformation, sSF are generally produced in the trail of a leading partial dislocations as *e.g.*, in the case of $\frac{1}{6}\langle 112\rangle\{111\}$ partial dislocations in FCC metals. Thus, the calculation of the GSFE often provides guidelines to identify the possible sSF of a crystal structure and probable dislocation dissociation paths as well as quantifying their propensity to appear *i.e.*, the lower the sSFE the easier the dislocation dissociation process.

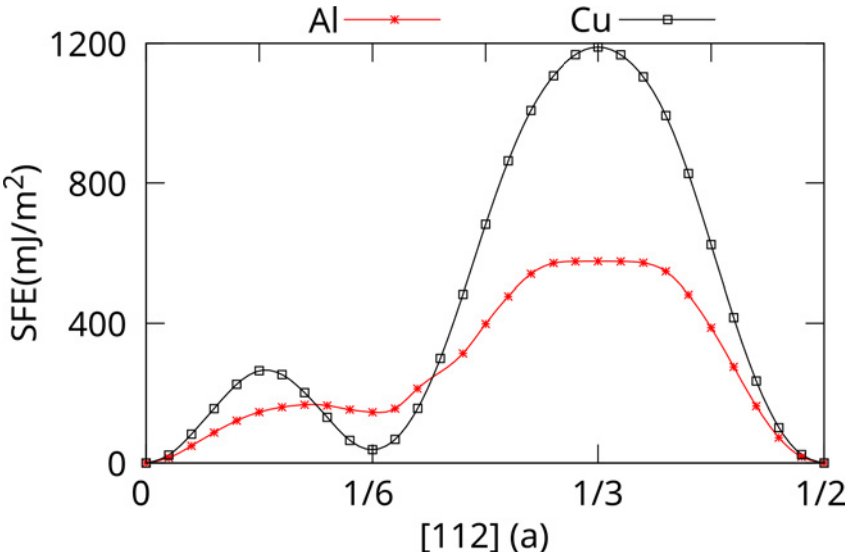

Figure 3.6: γ-line computed along $\langle 112$ in the $\rangle\{111\}$ slip plan of FCC Al and Cu using Mendelev [MEN 08] and Mishin EAM potentials [MIS 01], respectively

Figure 3.6 show example γ-line as computed in Al and Cu FCC metals using Mendelev [MEN 08] and Mishin EAM potentials [MIS 01], respectively. Computed γ-line show unstable and stable local minima (uSFE and sSFE), respectively for displacements of $\frac{1}{12}$ and $\frac{1}{6}$ of $[112]a_0$.

3.3.2 Basal (0001) stacking fault energies

A 3×2×8 supercell oriented along x=$[1\bar{2}10]$, y=$[10\bar{1}0]$ and z=[0001] is constructed for basal c GSFE calculations with translation vectors along x=$[1\bar{2}10]$ and y=$[10\bar{1}0]$ (see Figure 3.7). Configurations including two possible cutting c plane *i.e.*, between an O and an Al plane (Al_1 or Al_2) or between two consecutive Al_1 and an Al_2 planes, are investigated here using the Gale, the Vashishta and the SMTB-Q potentials. Results show that cutting between cationic and anionic planes lowers the SFE whatever the interatomic potential used (Figure 3.8a). Thus in the following, only lower energy basal GSFE with cutting

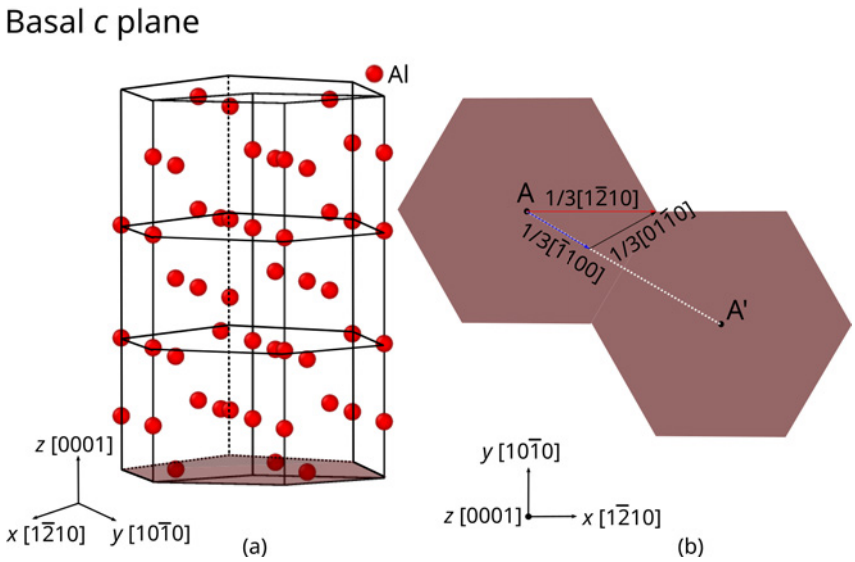

Figure 3.7: Illustration of the (0001) basal plane in α-Al_2O_3, (a) within the α-Al_2O_3 unit cell, red atoms refer to the Al sublattice, (b) in-plane projected view and important directions for basal stacking fault simulation.

plane between Al and O will be discussed.

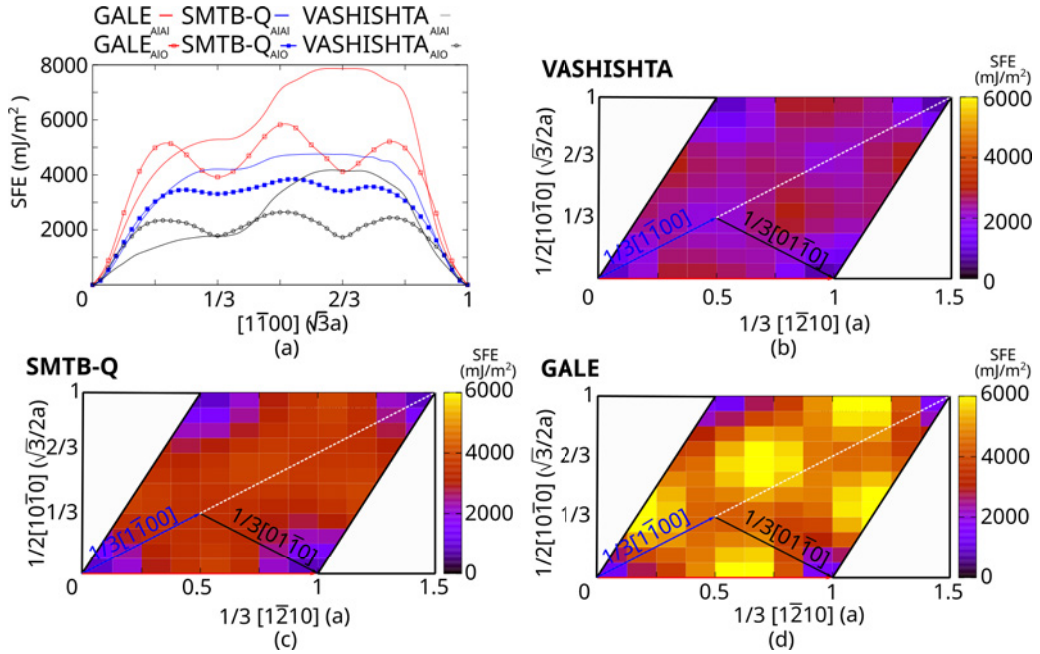

Figure 3.8: Stacking fault energy in the (0001) basal plane. (a) [1$\bar{1}$00] basal γ-lines with cutting planes between consecutive Al and O plans (dashed curves) and between two Al plans (plain curves). (b)-(d) Basal γ-surfaces computed using (b) Vashishta, (c) SMTB-Q and (d) Gale interatomic potentials, respectively.

The (0001) GSFE computed with the various potentials are shown in Figure 3.8. An

energy local minimum is found for a translation vector $\overrightarrow{b_1}=\frac{1}{3}[1\bar{1}00]$ leading to a sSFE of 1785.6, 3307.7 and 3917.8 mJ.m^{-2}, respectively for the Vashishta, the SMTB-Q and the Gale interatomic potentials (see Figure 3.8a). The Vashishta potential shows the lowest $\frac{1}{3}[1\bar{1}00](0001)$ sSFE when compared to the two other potentials. This result is in good agreement with first-principles data of about 1490 mJ.m^{-2} [MAR 01]. The γ-surface shows a similar qualitative behaviour with Vashishta and Gale showing lower and larger energy levels than SMTB-Q, respectively (see Figure 3.8c-d). The basal γ-surface suggests a possible split of the $\overrightarrow{b}=\frac{1}{3}[1\bar{2}10]$ Burgers vector into $\overrightarrow{b_1}+\overrightarrow{b_2}=\frac{1}{3}[1\bar{1}00]+\frac{1}{3}[0\bar{1}10]$ in a similar manner than in the model proposed by Kronberg [KRO 57]. However, this dissociation path has never been observed experimentally possibly due to the particularly high-energy of the basal sSFE. The dissociation of basal dislocations will be further discussed in the following.

As shown Figure 3.9, the $\frac{1}{3}[1\bar{1}00]$ sSFE is typical of the HCP structure and is commonly in metallic systems as *e.g.*, in zirconium (Zr) [CLO 09]. Here, the basal γ-surface in Zr is computed for comparison using the EAM Mendelev potential [MEN 07] (Figure 3.9) using the same methodology than for α-Al_2O_3. Both GSF show several similarities : they show similar global shapes as well as the same sSF displacement vector *i.e*, $\overrightarrow{b_1}=\frac{1}{3}[1\bar{1}00]$ with a sSFE of 197.7 mJ.m^{-2} in the Zr case in good agreement with Clouet results (see Figure 3.9a). This value is about one order of magnitude lower than in the case of alumina due to the softer metallic bond (that is compared here to a more energetic iono-covalent one).

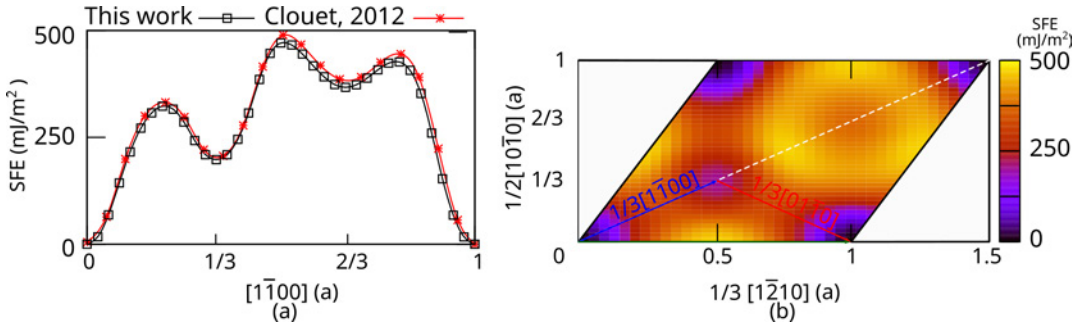

Figure 3.9: (0001) Basal stacking fault energy computed in Zr using the Mendelev EAM interatomic potential [MEN 07]. (a) γ-line computed in the $[1\bar{1}00]$ direction. Our study (black curve) is compared to Clouet data (red curve) [CLO 09]. (b) The basal γ-surface in Zr (our work).

3.3.3 Prismatic $\{10\bar{1}0\}$ and $\{1\bar{2}10\}$ stacking fault energies

α-Al_2O_3 is characterised by two kinds of prismatic planes *i.e.*, the m plane $\{10\bar{1}0\}$ and the a plane $\{1\bar{2}10\}$, as illustrated Figures 3.10. To compute the GSFE in the m plane, the simulation supercell is oriented with x=$[1\bar{2}10]$ and z=[0001] (the displacement directions) while the y axis is normal to the slip plane. On the other hand, simulation cell for the a

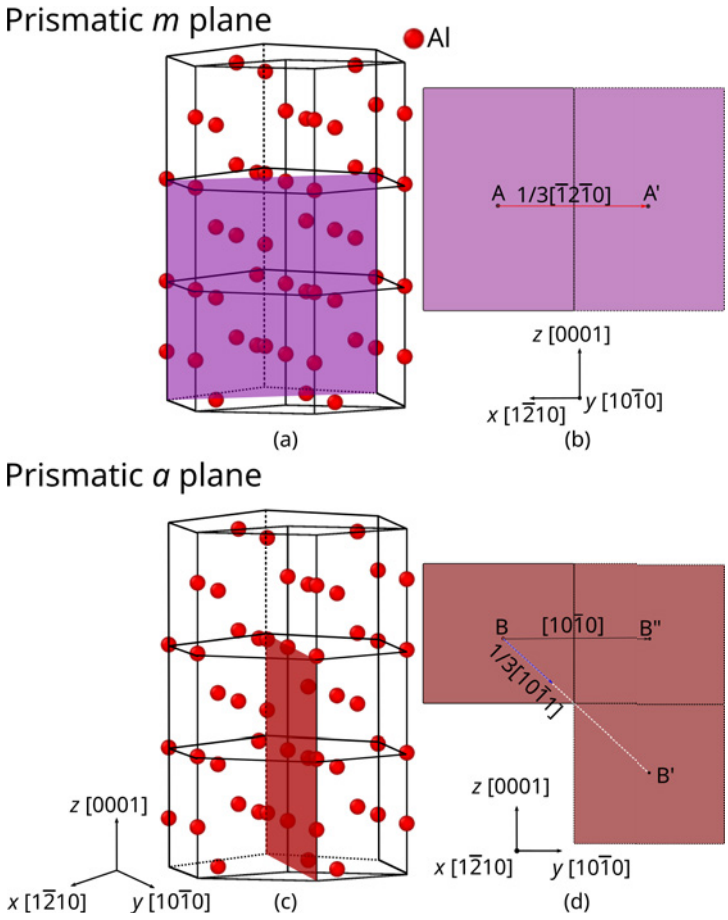

Figure 3.10: Representation of the prism m and a planes using perspective and in-plane projection views. (a,b) $\{10\bar{1}0\}$ prismatic m plane and (c,d) $\{1\bar{2}10\}$ prismatic a plane. Atoms colored in red rely on the Al sublattice.

plane GSF has the x axis direction normal to the fault plane and shift vectors along m and c directions.

The m plane γ-surface and γ-line along $\overrightarrow{b} = \frac{1}{3}[1\bar{2}10]$ are shown in Figure 3.11, respectively for Gale, Vashishta and SMTB-Q interatomic potentials. The results only show unstable configurations with a maximum of uSFE ranging from 5312 mJ.m^{-2} (Vashishta) up to 10650 mJ.m^{-2} (Gale) for x=$\frac{1}{6}[1\bar{2}10]$. This particularly high-energy of the uSF is reproduced using the SMTB-Q potential (6584 mJ.m^{-2}). Hence, this property suggests the m plane inadequacy for slip in α-Al_2O_3 what is confirmed by the lack of dislocation glide experimental evidence within this slip plan. A similar comparison with Zr than in the c case is shown Figure 3.3.3 with similar conclusions *i.e.*, same general shape of the GSFE and lower sSFE in the case of Zr.

Figure 3.12 shows the prismatic a γ-surface as well as the $[10\bar{1}0]$ γ-line as calculated with Gale, Vashishta and SMTB-Q interatomic potentials respectively. In this case, SMTB-Q

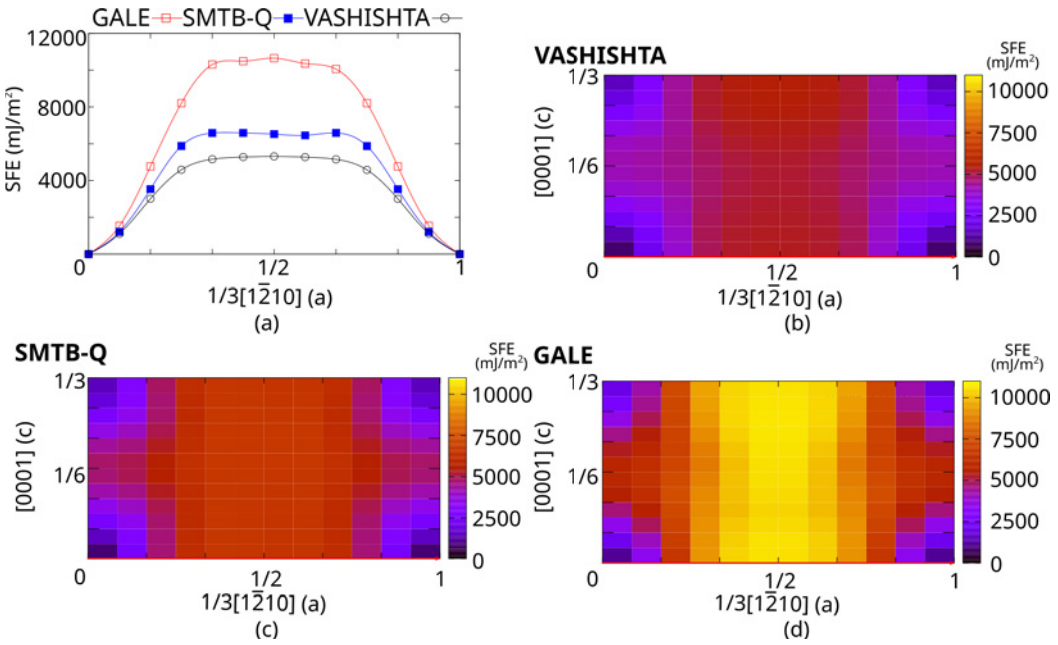

Figure 3.11: Stacking fault energy in the $\{10\bar{1}0\}$ prismatic m plane. (a) $\frac{1}{3}[1\bar{2}10]$ γ-line, (b)-(d) Prism m γ-surface computed using (b) Vashishta, (c) SMTB-Q and (d) Gale interatomic potentials, respectively.

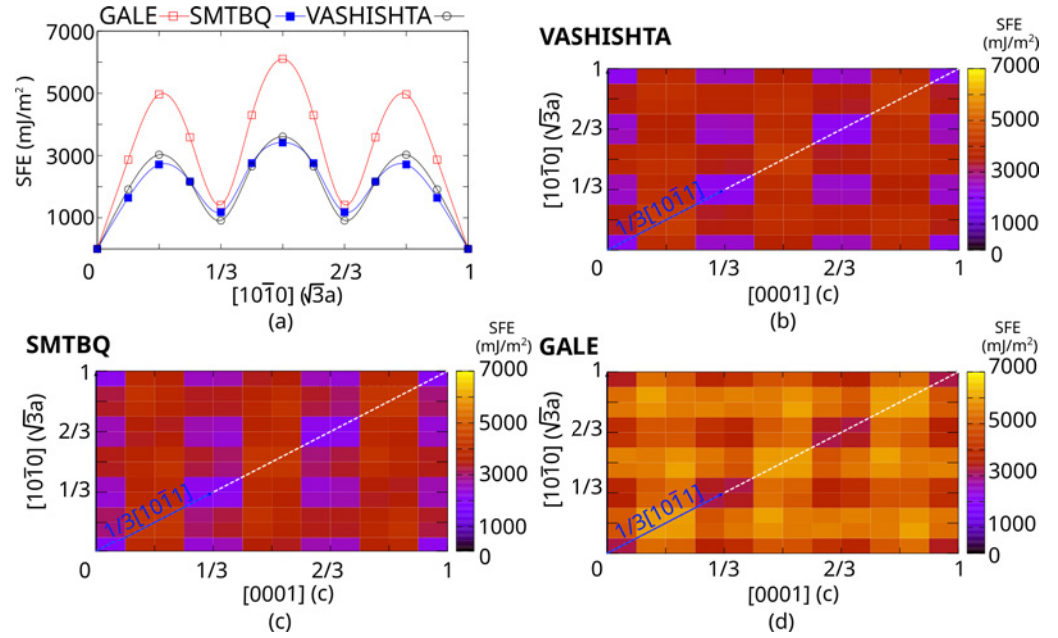

Figure 3.12: Stacking fault energy in the prismatic $\{1\bar{2}10\}$ a plane (a) $[10\bar{1}0]$ γ-line, (b)-(d) Prism a γ-surfaces computed using (b) Vashishta, (c) SMTB-Q and (d) Gale interatomic potentials, respectively.

and Vashishta potentials provide very close GSFE values while the Gale potential mainly overestimate. Three local minima are observed along the $[10\bar{1}0]$ direction. They correspond to the well-known $\frac{1}{3}[10\bar{1}0]$ dissociation path of the $\overrightarrow{b}=[10\bar{1}0]$ Burgers vector dis-

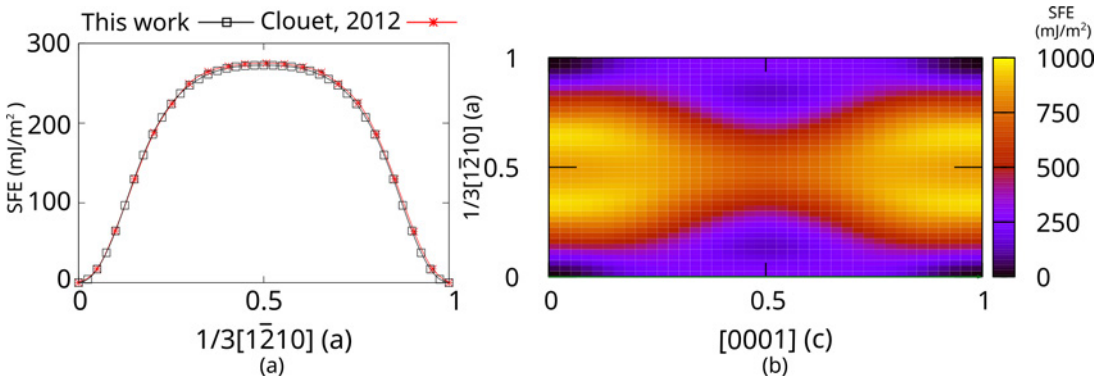

Figure 3.13: $(10\bar{1}0)$ Prismatic stacking fault energy computed in Zr using the Mendelev EAM interatomic potential [MEN 07]. (a) γ-line computed in the $[1\bar{2}10]$ direction. Our study (black line) is compared to Clouet data [CLO 09]. (b) The prismatic γ-surface

.

location within the prism a slip system [LAG 94, HE 02]. The prism a sSFE energy is about 911.5 mJ.m^{-2}, 1178.9 mJ.m^{-2} and 1411.4 mJ.m^{-2}, respectively for the Vashishta, the SMTB-Q and the Gale potentials. One can notice from the γ-surface that perfect crystal equivalent positions are also identified at $\frac{1}{3}[10\bar{1}1]$ and $\frac{2}{3}[10\bar{1}1]$, as expected from crystallography. Those equivalent positions are separated by single-hump energy barriers about twice larger than those of the $\frac{1}{3}[10\bar{1}0]$ direction what justify the lack of experimental evidence of perfect $\frac{1}{3}[10\bar{1}1]$ dislocation gliding in the a plane. Due to its low sSFE, the prism a plane plays a key-role in α-alumina plasticity that will be discussed later in this study.

3.3.4 Rhombohedral $\{01\bar{1}2\}$ stacking fault energies

The $\{01\bar{1}2\}$ rhombohedral (R) plane is reported as the one of the two host plane (with the c plane) for twinning in α-Al_2O_3 [HEU 66, SCO 83, LAG 02]. An illustration of the R plane is provided Figure 3.14. In this study, the supercell for R plane GSF calculation is built rotating the original supercell by 58° around the $[1\bar{2}10]$ axis leading to the x=$[11\bar{2}0]$, y=$[\bar{1}101]$ and z=$[1\bar{1}02]$ orientation.
The R γ-surface computed with the various potentials is illustrated Figure 3.15. As for the other cases, Vashishta and SMTB-Q potentials show quantitatively comparable results that are mainly overestimated by the Gale potential. Whatever the potential, the GSF suggests a dissociation path from $\overrightarrow{b}=\frac{1}{3}[0\bar{1}11]$ into smaller $\langle\bar{2}021\rangle$-type Burgers vectors but no local minima in the vicinity of $\frac{1}{22}[0\bar{1}11]$ as sometimes proposed in the literature in the context of rhombohedral twinning [GEI 94, LAG 02], even using coarsen displacement resolution simulations.

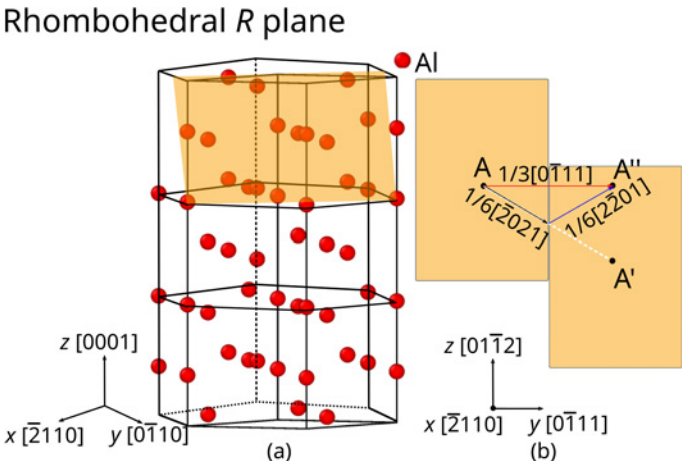

Figure 3.14: Illustration of a $\{01\bar{1}2\}$ rhombohedral plane, (a) within the α-Al_2O_3 unit cell, red atoms refer to the Al sublattice, (b) in-plane projected view and important directions for the stacking fault simulation within the R plane.

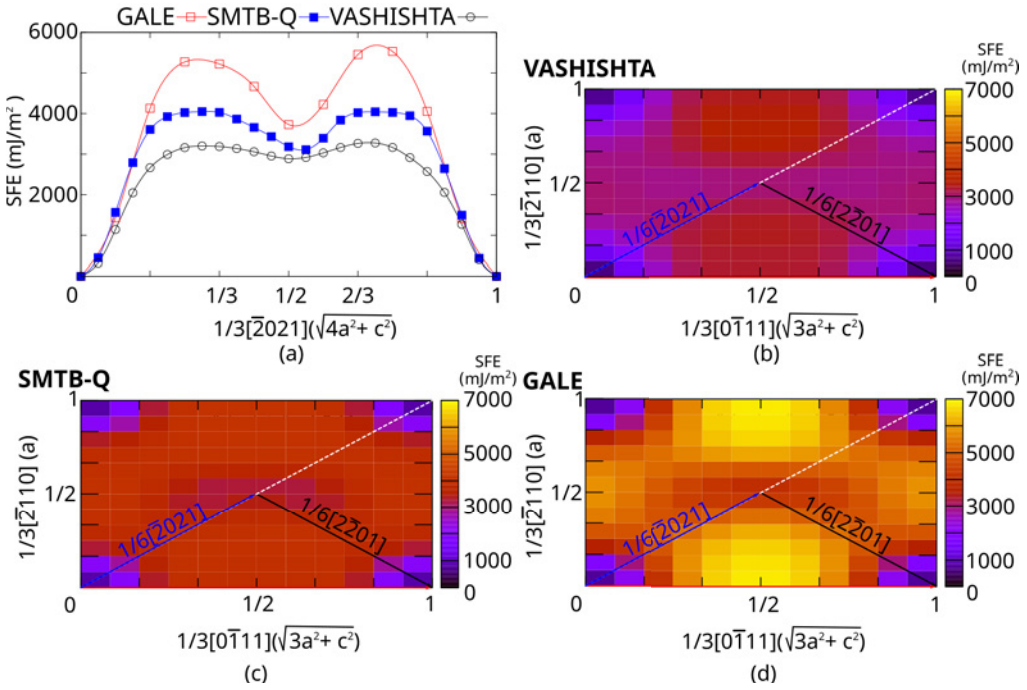

Figure 3.15: Rhombohedral (R) $\{01\bar{1}2\}$ stacking fault energy. (a) $[\bar{2}021]$ γ-line, (b)-(d) γ-surfaces computed using (b) Vashishta, (c) SMTB-Q and (d) Gale interatomic potentials, respectively.

3.3.5 Pyramidal Stacking fault energies

Several authors have shown that under certain orientations, pyramidal slip can occur in α-alumina (Figure 3.16) [HOC 75, SNO 73]. Four typical pyramidal slip systems are identified *i.e.*, the s slip systems $\frac{1}{3}\langle\bar{1}101\rangle\{10\bar{1}1\}$ or $\frac{1}{3}\langle\bar{1}2\bar{1}0\rangle\{10\bar{1}1\}$, n $\frac{1}{3}\langle\bar{1}101\rangle\{2\bar{1}\bar{1}3\}$ or $\langle01\bar{1}0\rangle\{2\bar{1}\bar{1}3\}$, w $\frac{1}{3}\langle\bar{1}102\rangle\{2\bar{1}\bar{1}2\}$ or $\langle01\bar{1}0\rangle\{2\bar{1}\bar{1}2\}$ as well as v $\langle01\bar{1}0\rangle\{4\bar{2}\bar{2}3\}$. Table 3.4

shows the parameters used to construct the different pyramidal supercells.

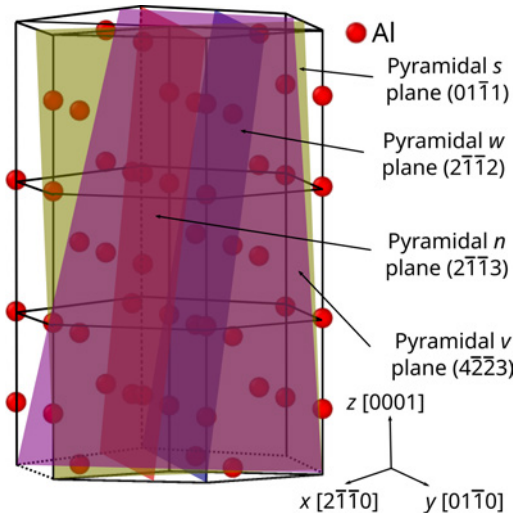

Figure 3.16: The s, n, w and v pyramidal planes described in the framework of the α-Al_2O_3 cation sublattice.

Slip plane	Rotation axis	Rotation angle	Final orientation
n	$[01\bar{1}0]$	61.7°	$x' = [\bar{2}112]$, $y' = [01\bar{1}0]$ and $z' = [2\bar{1}\bar{1}3]$
s	$[1\bar{2}10]$	72.7°	$x' = [1\bar{2}10]$, $y' = [\bar{1}012]$ and $z' = [10\bar{1}1]$
w	$[0\bar{1}10]$	70.3°	$x' = [2\bar{1}\bar{1}4]$, $y' = [0\bar{1}10]$ and $z' = [2\bar{1}\bar{1}2]$
v	$[0\bar{1}10]$	74.9°	$x' = [\bar{2}113]$, $y' = [0\bar{1}10]$ and $z' = [4\bar{2}\bar{2}3]$

Table 3.4: Parameters for pyramidal GSF supercell constructions. The supercells are built rotating the original basal collumnar orthogonal supercell around various axis using angle that rely on the target orientation.

Figures 3.17 and 3.18 describe the γ-lines and γ-surfaces for the s, n, w and v pyramidal planes computed using the Vashishta interatomic potential. The pyramidal s γ-surface is computed between equivalent positions defined by $\frac{1}{3}[\bar{1}011]$ and $\frac{1}{3}[1\bar{2}10]$. Simulations along $\frac{1}{3}[\bar{1}011]$ show a local minimum (sSFE=4554.1 mJ.m^{-2}), while only an extremum (uSFE=4905.1 mJ.m^{-2}) is noticed along $\frac{1}{3}[1\bar{2}10]$. Therefore, pyramidal s slip is possibly characterized by a $\frac{1}{3}\langle\bar{1}011\rangle$ Burger vector as proposed by Ünal *et. al.* [ÜNA 94]. Pyramidal n γ-surface is computed between equivalent positions at $\frac{1}{3}[\bar{1}101]$ and $[01\bar{1}0]$. The pyramidal n γ-line computed along $\frac{1}{3}[\bar{1}101]$ does not show any local minimum but only a maximum of about uSFE=4556.4 mJ.m^{-2}, while it shows a local minimum uSFE=1830.1 mJ.m^{-2} along $[01\bar{1}0]$ which is far lower than that maximum.
Pyramidal v γ-surface is characterized by a slight vertical asymmetry *i.e.*, the left part of the γ-line shows a higher energy than the right part. One can notice from the γ-surface that perfect crystal equivalent positions can be identified along $\frac{1}{6}[\bar{2}023]$ and $[0\bar{1}10]$, as expected from crystallography. Those equivalent positions are separated by two-hump energy barriers about twice larger than those of the perfect $[0\bar{1}10]$ direction what justify

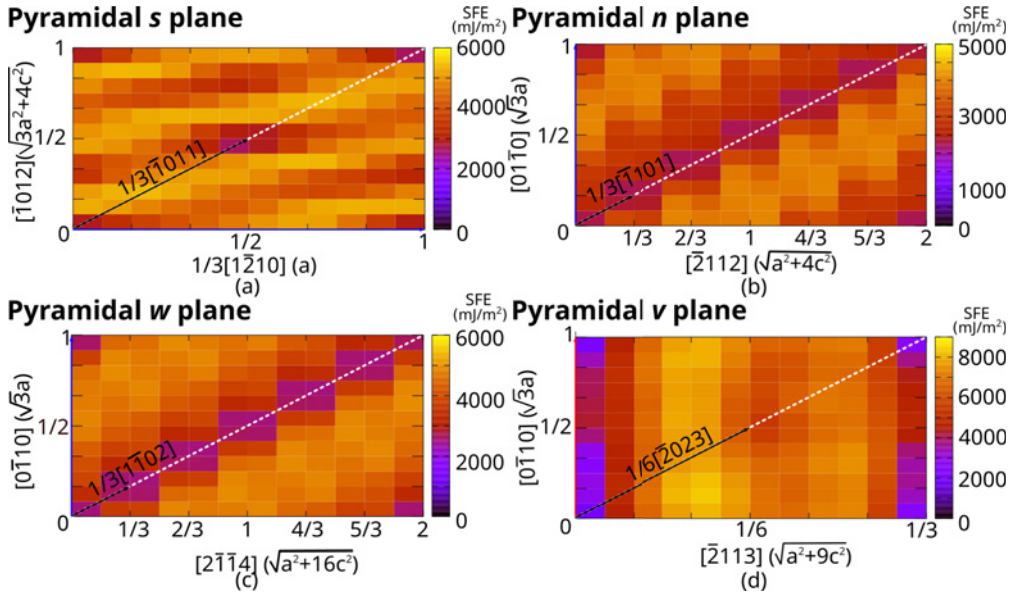

Figure 3.17: γ-surfaces in (a) s, (b) n, (c) w and (d) v pyramidal slip planes computed using the Vashishta interatomic potential.

the lack of experimental evidence of $\frac{1}{6}[\bar{2}023]$ dislocation gliding in the v plane [KOT 82].

The pyramidal w γ-surface shows equivalent positions along $\frac{1}{3}[1\bar{1}02]$ and $[0\bar{1}10]$. The sSFE for the two directions show comparable energy (respectively sSFE=4027.5 and 4156.9 mJ.m^{-2}), while the maximum noticed along $[0\bar{1}10]$ (uSFE=5418.0 mJ.m^{-2}) is larger than the one along $\frac{1}{3}[1\bar{1}02]$ (uSFE=4795.2 mJ.m^{-2}). Hence, $\frac{1}{3}\langle 1\bar{1}02\rangle$ is a possible Burgers vector for pyramidal w as discussed by Gooch *et. al.* [GOO 73].

3.3.6 Discussions about GSF

Slip plane	$\overrightarrow{b}$	$\overrightarrow{b_p}$	Burgers vector length (Å)
Basal c (0001)	$\frac{1}{3}\langle 11\bar{2}0\rangle$	$\frac{1}{3}\langle 1\bar{1}00\rangle$	4.72 (2.73)
Prismatic m $\{10\bar{1}0\}$	$\frac{1}{3}\langle 11\bar{2}0\rangle$		4.72
Prismatic a $\{1\bar{2}10\}$	$\frac{1}{3}\langle\bar{1}101\rangle$		5.16
	$\langle 10\bar{1}0\rangle$	$\frac{1}{3}\langle 10\bar{1}0\rangle$	8.18 (2.73)
Rhombohedral R $\{01\bar{1}2\}$	$\frac{1}{3}\langle 0\bar{1}11\rangle$	$\frac{1}{6}\langle\bar{2}021\rangle$	5.16 (3.50)
Pyramidal n $\{2\bar{1}\bar{1}3\}$	$\langle 01\bar{1}0\rangle$		8.18

Table 3.5: Slip planes and shortest possible Burgers vectors in α-Al_2O_3. b relies to perfect Burgers vectors while b_p is for partial dislocation.

Overall, GSFE computed using the Vashishta potential provide comparable results

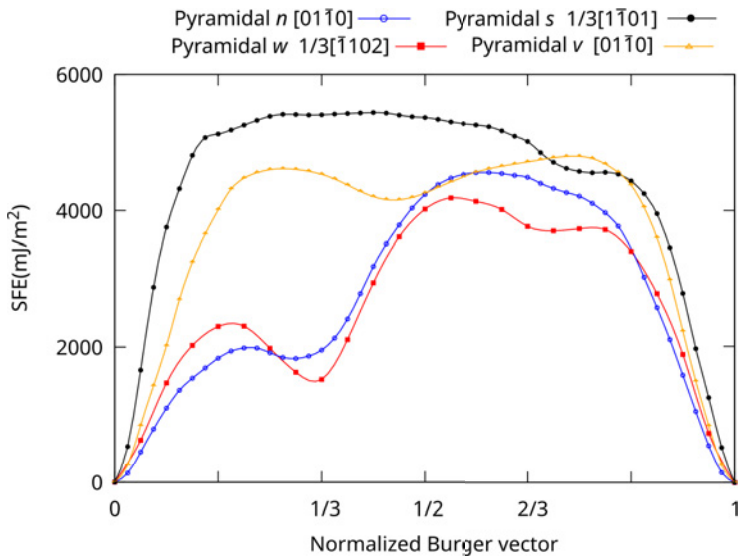

Figure 3.18: γ-lines for s, n, w and v pyramidal slip computed using Vashishta interatomic potentials. Translation directions are provided in the legend.

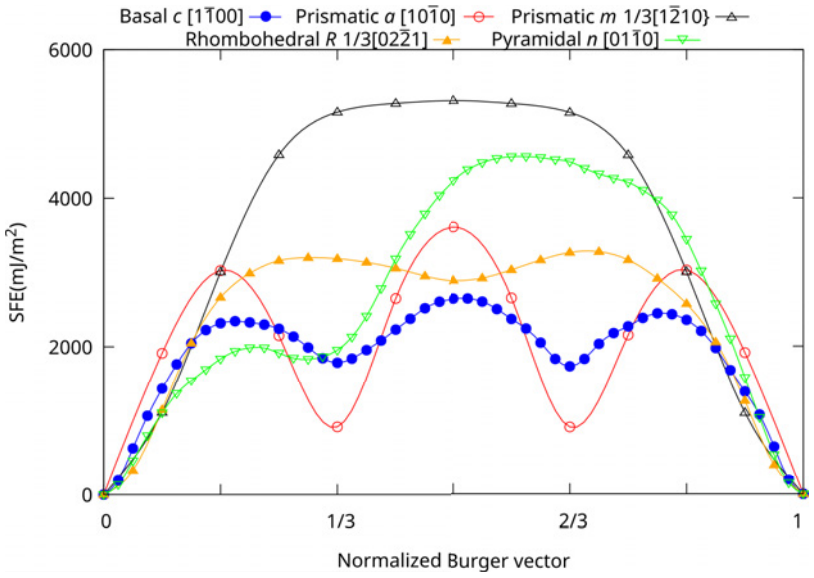

Figure 3.19: γ-lines computed in the c, a, m, R and n planes using appropriate Burgers vectors directions (see legend). Simulations are performed using the Vashishta interatomic potential.

to those computed using the more detailed SMTB-Q in the contrary to Gale potential outcomes that are significantly larger. This result reinforces the transferability of the Vashishta potential to shear-related properties. The Figure 3.19 shows γ-lines computed in the various slip planes and along appropriate Burgers vector directions. Results suggest dissociation paths with quite low sSFE for the prism a and the c slip systems (respectively 911.5 and 1785.6 mJ.m^{-2}) as well as for the pyramidal n slip system (1830.1

$mJ.m^{-2}$). These results are in good agreement with experimental observations of basal slip and twinning as *e.g.,* in case of bulk alumina deformation experiments performed at intermediate temperature [CAS 04] as well as evidences of prim a slip (as *e.g.*, in Ref. [CAS 81a, CAS 81b]). Furthermore, these results confirm observed (and modeled) dislocation dissociation paths [LAG 94, CAS 04, HE 02]. The pyramidal n slip system is also identified with MD simulations and plays a dominated role on plastic deformation process [ZHA 08, KIM 18]. On the other hand, only high-level GSFE extreme are noticed for the the m plane γ-line (as for the entire m γ-surface) what supposes (i) no dislocation dissociation path and (ii) hard shearing capabilities, as confirmed by the lack of experimental evidences about dislocation slip in the m plane. Finally, the R plane shows a sSF configuration at $\frac{1}{6}[0\bar{2}21]$ which has a larger energy value than in the c and a cases. While elevated SFE generally decreases dissociation likelihood, one can notice that the R sSF suggested here is associated to a particularly short Burgers vector of about 3.50 Å (see Table 3.5) what might counteract the energy criterion. Also, it is worth noticing that the sSF configuration computed in the R plane is characterized by a translation vector significantly different than the $\frac{1}{21.9}[0\bar{1}11]$ suggested in the literature [GEI 94, LAG 02, HE 02]. Additional simulations using for example DFT simulations could help to conclude about this specific point.
Finally, GSFE simulations suggest a high-transferability of the Vashishta potential toward shearing properties while the discrepancies noticed when using the RI Gale potential increase. In the last section, we will focus on the ability of the Vashishta potential to model the well-known basal edge dislocation. As in the entire study, results will be compared to SMTB-Q outcomes as well as to the current literature.

3.4 Basal edge dislocation

Dislocations are linear defects responsible for the irreversible plastic deformation of crystalline materials. In particular, their mobility is strongly related to the atomic configuration close to the defect core. In α-alumina, basal $\frac{1}{3}\langle 1\bar{2}10\rangle(0001)$ dislocations are known to be the most common to appear during high-temperature deformation [LAG 94, HE 02, HEU 10]. Moreover, the $\frac{1}{3}\langle 1\bar{2}10\rangle$ edge dislocation can dissociate into two partial dislocations with $\frac{1}{3}\langle 10\bar{1}0\rangle$ Burgers vectors (see Equation 3.6). It is known that the dissociation process operates along the [0001] direction within a prismatic plane via a climbing mechanism resulting into two 60° mixed dislocations [HEU 10].

$$\frac{1}{3}[11\bar{2}0] \rightarrow \frac{1}{3}[10\bar{1}0] + \frac{1}{3}[01\bar{1}0] \tag{3.6}$$

Still, a net controversy persists about the partial dislocation core structures for which two models are discussed in the literature. On one hand, Kronberg *et al.* proposed that

slip occurs between two consecutive Al and O layers [KRO 57]. This slip model involves charge transport due to the ionic bonding between Al and O atoms. On the other hand, Bilde-Sørensen *et al.* proposed a mixed partial core that glides between two consecutive puckered Al layers without charge transfer [BIL 96]. The various dislocation core models are illustrated Figure 3.20. While Shibata *et al.* [SHI 07] confirmed Kronberg's core hypothesis using scanning HRTEM, Heuer *et al.* [HEU 10] produced a markedly detailed atomic model of the dislocation cores with Al-Al terminated partial dislocations using the negative spherical-aberration imaging technique supporting the Bilde-Sørensen's model.
In the following, we extent the original work of Tsuruta *et al.* [TSU 14] by investigating both Al/O-terminated or Al/Al-terminated basal partial dislocations using both the 2/3-body Vashishta and the variable charge SMTB-Q potentials.

3.4.1 Methods

As shown Figure 3.20, a dipole of edge basal dislocations is introduced in a $73.13 \times 0.83 \times 144.97$ nm^3 simulation cell following the approach proposed by Tsuruta *et al.* This size was chosen large enough to avoid size-effect. Each $\frac{1}{3}\langle 11\bar{2}0\rangle$ dislocation is introduced as a pair of mixed partial dislocation separated by 2 nm long stacking faults within the prismatic plane. This length corresponds to the lowest energy configuration when computed using the Vashishta potential (see Ref. [TSU 14]). The partial dislocation pairs are either Al/Al- (Figure 3.20(b,d)) or Al/O-terminated (Figure 3.20(c,e)) as proposed in the models of Bilde-Sørensen and Kronberg, respectively. After removing corresponding Al and O atoms on planes perpendicular to the basal plane, the empty region is closed applying the linear elastic theory [HIR 82].

Using the Vashishta potential, the system is then relaxed using the following procedure. Firstly, the energy is minimized using the FIRE algorithm and a force norm criterion of 10^{-6} eV/Å. Then, a LT MD shake (timestep dt=1 ps) is performed during 50 ps using the NPT ensemble (anisotropic pressure relaxation) and the Nosé-Hoover thermostat in order to remove residual stresses. The final configuration obtained is later referred as the Vashishta relaxed dislocation core configuration.
Secondly, the Vashishta relaxed dislocation core is used as an input for further SMTB-Q potential calculations: the potential energy is first minimized using the FIRE algorithm and a quite large force norm target (pre-minimization). At this stage, the residual hydrostatic pressure is about several GPa due to the lattice parameter difference between both interatomic potentials. Then, a 0K pressure relaxation simulation and a final minimization run are consecutively performed down to a net force norm of 10^{-2} eV/Å.

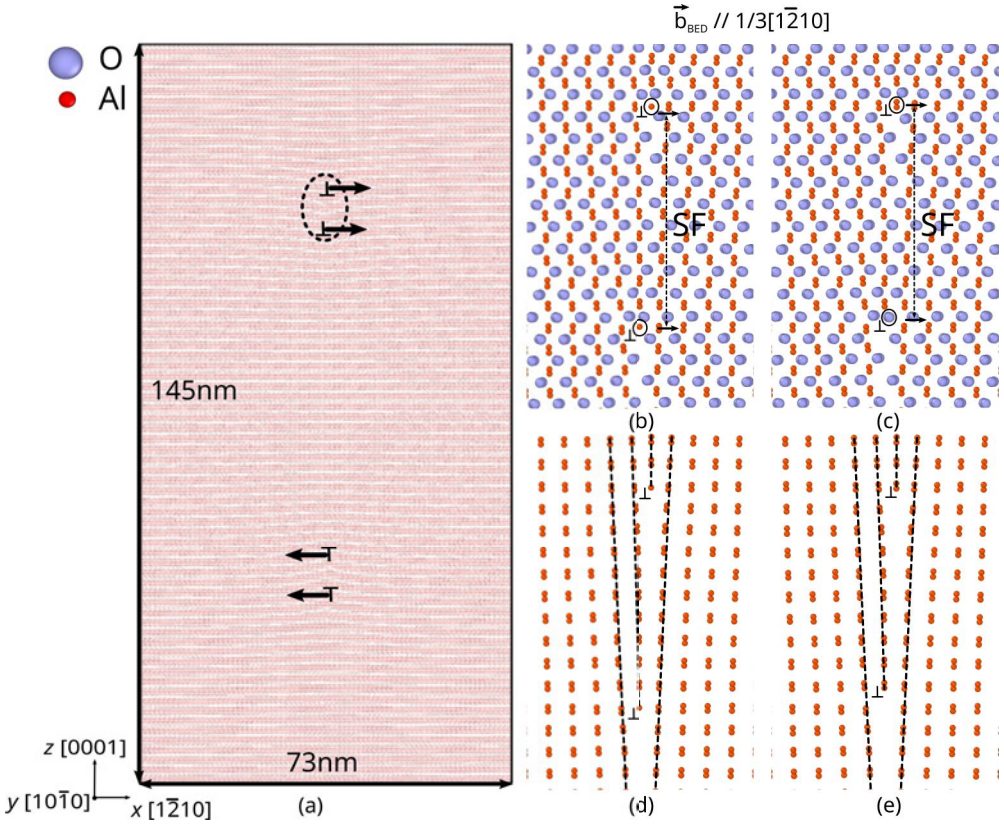

Figure 3.20: Unrelaxed basal edge dislocation core structure. (a) Simulation cell and edge dislocation dipole. (b) Al/Al-terminated dislocation core (Bilde-Sørensen's model), (c) Al/O-terminated dislocation core (Kronberg's model), (d) and (e) illustrate respective cation sublattices.

3.4.2 Results

Figure 3.21 shows partially and fully relaxed configurations for Kronberg and Bilde-Sørensen dislocation models using both the Vashishta and SMTB-Q interatomic potentials. *Minimization #1* refers to the outcome of the first minimization episode (whatever the interatomic model used) while *Minimization #2* refers to (i) the minimization outcome after the NPT run in the case of the Vashishta potential and (ii) the minimization outcome after the box relaxation run in SMTB-Q case. Due to the perfect symmetry observed, only one dislocation extracted from the original dislocation dipole is discussed in the following. Dislocation core configurations obtained using the Vashishta potential are similar to those of Tsuruta *et al.* using the same interatomic potential. The two mixed partial dislocation exhibit particularly different structures whatever the Al/Al- or Al/O-terminated configuration. When compared to the unrelaxed structure shown Figure 3.20, the fully-relaxed top cores (single-Al or double-Al terminated respectively for Bilde-Sørensen and Kronberg models) shown Figure 3.21c,g are characterized by a regular dislocation core relaxation process that adapts the local mismatch while the bottom cores (either single-Al or single-O terminated respectively for Kronberg or Bilde-Sørensen model) are characterized by an

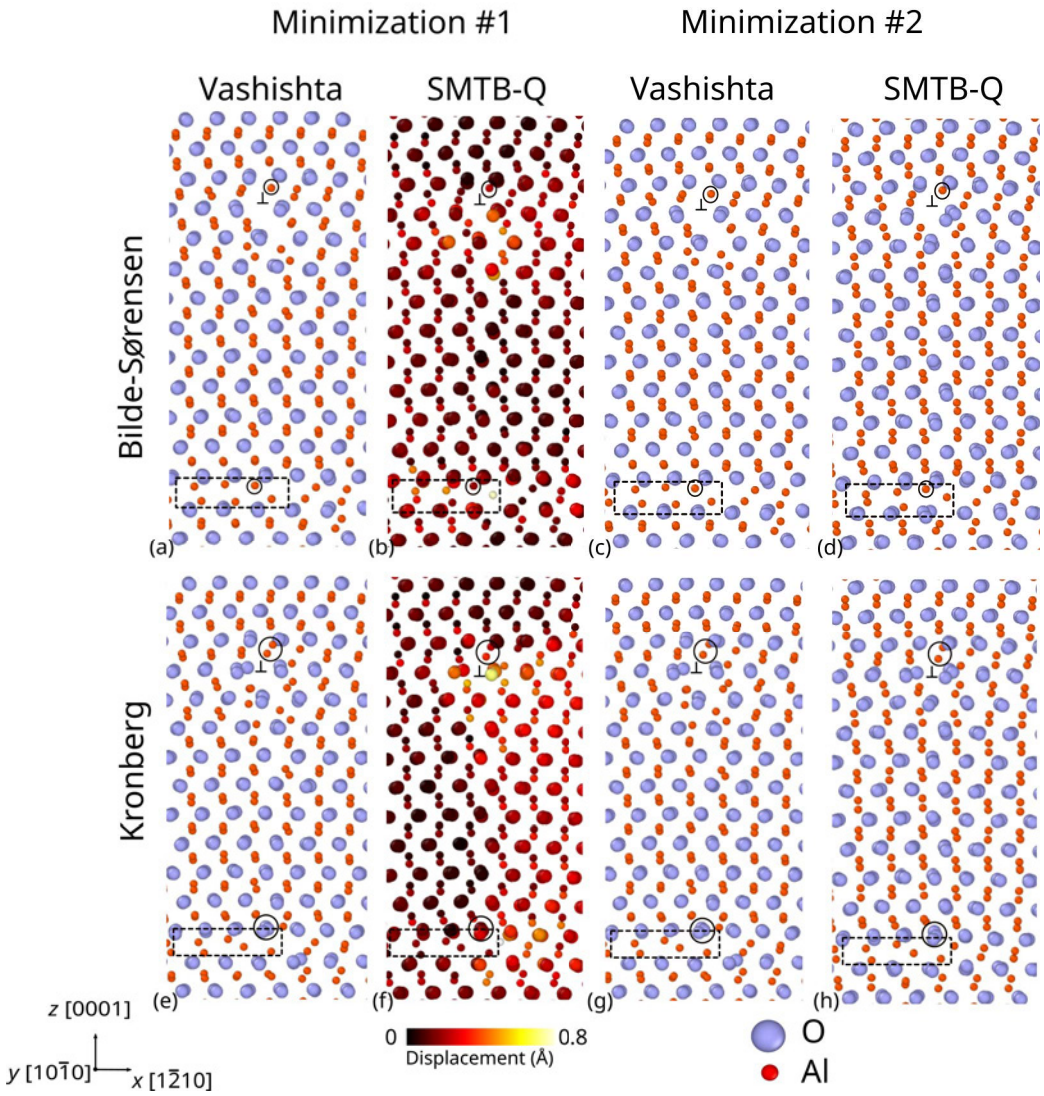

Figure 3.21: Dislocation core for (a:d) Al/Al-terminated (Bilde-Sørensen) and (e:h) Al/O-terminated (Kronberg) dislocations computed using the Vashishta and SMTB-Q interatomic potentials. The stacking fault length is set to ∼2 nm. Minimization #1 refers to the initial minimization run result while Minimization #2 refers to (i) the post-NPT minimized configuration for Vashishta and (ii) the post-box relaxation minimized configuration in the SMTB-Q case. Atoms surrounded by black circles refer to dislocation-termination atoms. The dashed rectangle emphasizes the puckered Al layers in which the bottom dislocation fault extends. (b,f): atoms are colored according to the displacement vector amplitude calculation. For each case, the reference structure is the input configuration *i.e.*, the fully-relaxed Vashishta configuration presented in c) and g) respectively.

extended fault in the Al puckered layer. As in the work of Tsuruta *et al.*, we also notice the larger extent of the Al fault for the Al/Al-terminated dislocation model when using the Vashishta interatomic potential.
Topological configurations obtained using the variable charge potential SMTB-Q are particularly similar to those obtained using the Vashishta potential. This feature is quantified here using the displacement vector analysis after *Minimization #1* shown in Figure 3.21b,f taking respective inputs as reference file. Indeed, the maximum displacement computed between the fully-relaxed Vashishta configuration and the partially-relaxed SMTB-Q configuration (before simulation box relaxation) located deep in the dislocation core is lower than 1 Å which confirms the similarity between the two configurations. Here again using the SMTB-Q potential, the top core is characterized by a regular core relaxation without particular directional extension while the bottom core show an extended planar fault within the Al puckered layer. However, one can notice two particular changes specific to the SMTB-Q potential (i) the oxygen atoms in the top core are slightly more disorganized and (ii) the bottom core planar fault is less extended for both models, when compared to the Vashishta potential. Nevertheless, these differences remain quite acceptable having in mind the simplicity of the 2/3-body Vashishta potential when compared to the more complex SMTB-Q.

A simplified calculation of the dislocation energy E_{dislo} can be derived using the simulation cell energy with and without defect:

$$E_{dislo} = \frac{E_{tot} - n.E_{coh}}{2L} \tag{3.7}$$

where E_{tot} is the minimized energy of the simulation as computed after *Minimization #2*, n is the number of atoms, E_{coh} is the per-atom cohesive energy and L is the dislocation length.

Equation 3.7 can be used to qualitatively compare interatomic potential tendencies as presented in Table 3.6. Results confirm prior topological observations with only slight energy variations between Kronberg and Bilde-Sørensen models. Here, the comparison between Vashishta and SMTB-Q leads to (i) similar topological configurations, (ii) comparable range of energy and, the most important, (iii) similar relative energy trends *i.e.*, E_{dislo} is slightly lower in the Bilde-Sørensen case than in the Kronberg one. Having in mind the previous outcomes on GSFE, this results appears as an additional confirmation of the Vashishta potential transferability to nanomechanics.

	Vashishta		**SMTB-Q**	
E_{coh} (eV/at.)	-6.35		-6.40	
	Al/Al	**Al/O**	**Al/Al**	**Al/O**
n	1019720	1019700	1019720	1019700
E_{tot} (eV)	-6475206.6	-6475074.6	-6528738.4	-6528609.4
L (Å)	8.18		8.32	
E_{dislo} (eV/Å)	14.44	14.74	18.59	18.65

Table 3.6: Dislocation energy as computed using Equation 3.7 respectively for Kronberg Al/O and Bilde-Sørensen Al/Al dislocation model using the Vashishta and the SMTB-Q potentials.

3.5 Conclusion

The aim of Chapter 3 was to investigate the atomic-scale modeling possibilities in α-alumina verifying the transferatiblity of various interatomic potentials to small-scale deformation. Lattice parameters, elastic constants, surface and stacking-fault energies as well as dislocation properties were investigated using rigid ion, 2/3-body and variable charge potentials leading to the following conclusions:

— All the potentials tested succeed in computing lattice parameters of α-Al_2O_3 but most of the tested rigid ion potentials show discrepancies when computing elastic constants (all except the Gale parameterization [GAL 92]). However, these later are correctly reproduced by the 2/3-body Vashishta and the SMTB-Q potentials.
— The 2/3-body Vashishta and variable charge SMTB-Q potentials provide similar topological outcomes and energy values for the various (0001) surface terminations. Same conclusions are drawn for stacking fault energy calculations in several slip plans of the crystalline structure. These results are in good agreement with already published DFT data and experiments while the Gale rigid ion potential overestimates surface and stacking fault energies and show different topological configurations.
— The basal edge dislocation structure as computed using the Vashishta potential compare successfullly to the more sophisticated SMTB-Q. Furthermore, both potentials show similar dislocation energy trends (as a function of the core model) that confirms a slighlty lower core energy for the basal edge dislocation when defined using the Bilde-Sørensen model.

Chapter III summary:

This chapter focused on testing the transferability to α-Al_2O_3 of a bench of interatomic potentials including RI, 2/3-body and variable charge interatomic potentials. These potentials were investigated computing various materials properties known to be relevant for nanomechanical simulations. Three potentials were highlighted *i.e.*, the RI Gale [GAL 92], the Vashishta [VAS 08] and the SMTB-Q [SAL 16], the later being used only for small-scale comparisons due to elevated cpu costs. Finally, the Vashishta potential has shown to be the best at reproducing data when compared to SMTB-Q or literature data including DFT simulations and experiments.

Chapter 4

α-Al_2O_3 nanoparticles modeling fabrication and characterization

As described in Chapter 1, the plastic deformation of NPs is strongly related to their size, shape and surfaces [MOR 11, WEI 12, AMO 17, KIL 18, SHA 18, AMO 21]. At the nanoscale, free surfaces play a dominant role as sources and sinks for dislocation nucleation in originally pristine nanostructures. In particular, it is known that dislocations or twins can nucleate in highly-stressed regions.

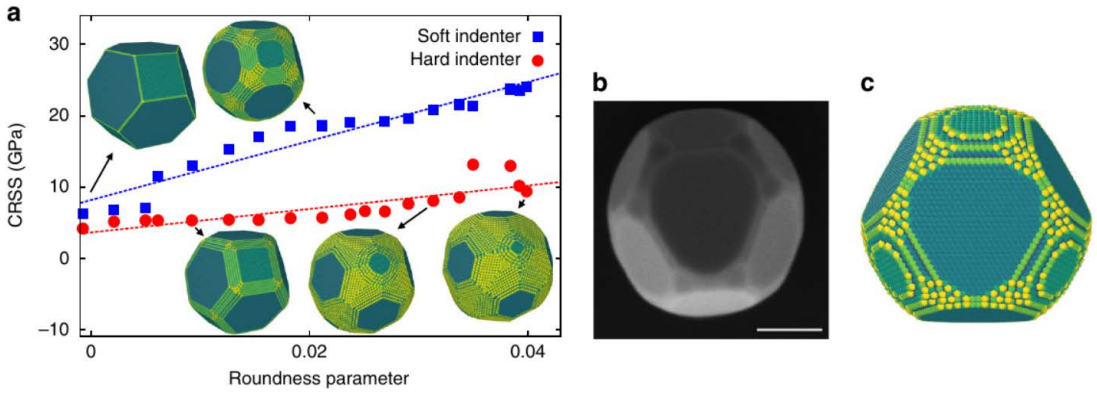

Figure 4.1: Influence of edge and corner roundness on the mechanics of nickel NPs. (a) MD compressive strength as function of the NP roundness, (b) SEM imaging of Wulff shape Ni NP, (c) a similar NP made for MD simulations. Adapted from Ref. [SHA 18].

Thus, modeling advanced shapes and surfaces of nano-objects is important to better address their deformation processes and mechanical properties (Figure 4.1). This is particularly true in the case of ceramics and oxides where charges have to be taken into account. In addition to its role in nucleation-controlled plasticity, the design of nano-objects also has implications in other physical properties such as surface-mediated bulk diffusion as *e.g.* in ZnO nanowires where a large diffusivity is observed [SHI 17, CHE 15] or in catalysis [ABU 19, CAR 21]. In the following, we first describe the two methods

we used to build charged and neutral α-Al_2O_3 nanospheres, methods referred later as the classical and the pattern-based methods, respectively. Then, the molecular processing of the samples *i.e.*, energy minimization, equilibration and surface characterization, using the Vashishta interatomic potential, will be presented. These samples will be further used to investigate the mechanical properties of α-Al_2O_3 under compression in the final Chapter 5.

4.1 Nanosphere fabrication methods

4.1.1 The *cutting-block* classical method

To build nano-objects for MD simulations, researchers generally replicate a pre-oriented unit cell in the three directions of space before slicing. For NPs, the cuts are carefully chosen to obtain pre-defined NP shapes such as cubes, spheres or polyhedrons (like *e.g.*, Wulff-shaped or winterbottom NPs). Even if very popular, this method has few drawbacks such as generating absolutely flat surfaces and sharp edges (see discussion in Ref. [AMO 17, SHA 18]).

This classical method is applied here to build charged NPs using ATOMSK and the Lewis *et al.* [LEW 82] .cif file parameterization of the α-Al_2O_3 unit-cell from the American Mineralogist Crystal Database (`http://rruff.geo.arizona.edu/AMS/amcsd.php`). First, a large and neutral block of α-Al_2O_3 atoms is constructed as shown Figure 4.2a before a nanosphere is carved out using a combination of the -select and -rmatoms commands of ATOMSK. The center of the nanosphere is arbitrary located at the same position than the center of the block, see Figure 4.2b. This method does not allow to conserve the net charge of the original block. For example, a NP of radius r=10 nm is made of 24538 Al and 36996 O atoms using this method. In this case, the Al atoms ratio $\mu_{Al} = \sum Al/(\sum Al + \sum O)$ is equal to 0.39877 which is slightly sub-stoechiometric (μ_{Al}=0.4 in the neutral case) meaning that the system ends up with a negative net charge. In nature, charged systems will generally find a way to neutralize using their close environment (*e.g.*, adsorbing O or H atoms for example) which is usually not straightforward in classical MD simulations. In addition, charge summation methods (*e.g.*, Ewald) are not designed to rigorously solve charged systems but only neutral. For this purpose, we propose in the following an alternative method to design neutral nano-objects.

4.1.2 The pattern-based method

To avoid charged surfaces, we developed a new method referred as the pattern-based method in opposition to the aforementioned classical method. Basically, this method relies on the definition of neutral motives made of few atoms that are reproduced on a 3D

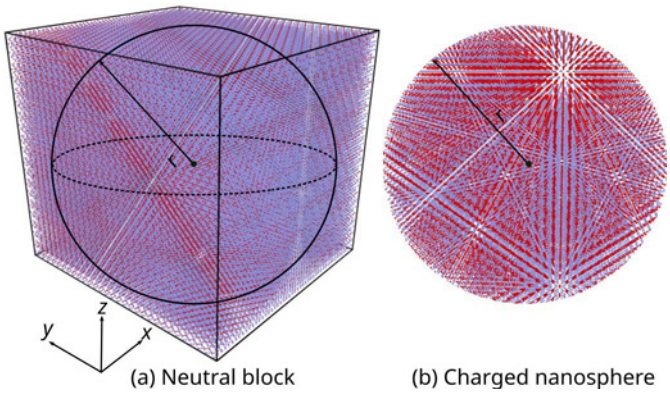

Figure 4.2: Numerical fabrication of charged NPs using the cutting-block classical method, (a) illustration of the starting α-Al_2O_3 block later sliced to create a nanosphere (b). This method does not conserve the starting neutral charge of the block system.

canvas designed *a priori*, based on the target shape of the sample. Obviously, several motives and/or canvas can be used and the thinner the canvas *i.e.*, the smaller the motive, the more precise the sample surface discretization. One typical motive-canvas couple is the α-Al_2O_3 orthogonal unit-cell and its respective lattice (the one used for simulations presented in Chapter 3). While this guess is simple to build, it leads to particularly rough-shaped nano-objects when using it as a 3D pattern due to the large number of atoms (60 atoms) per unit-cell.

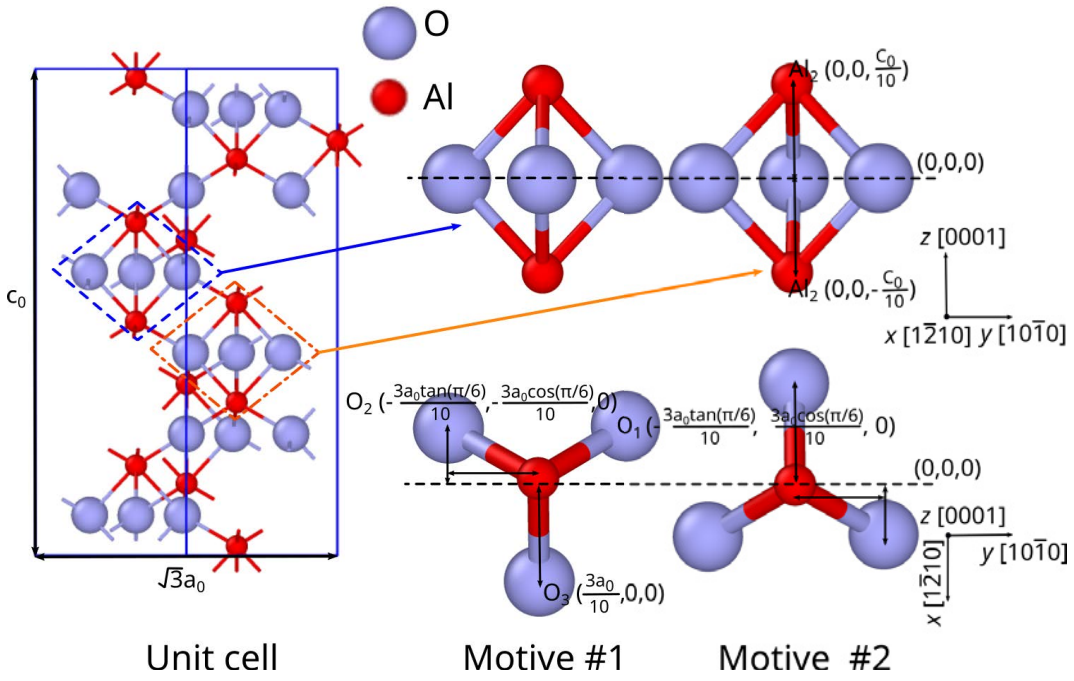

Figure 4.3: Elementary motives #1 and #2 used in the pattern-based method to build α-Al_2O_3 neutral NPs.

In this study, we use two motives made of a single α-Al_2O_3 molecule each (2×5 atoms) as shown Figure 4.3. The two motives differ only by their middle oxygen atoms that alternate from back to front x position. Assuming the origin of the motive at mid-distance between the two Al atoms, atoms of motive #1 are positioned at Al_1=(0,0,-$\frac{c_0}{10}$), Al_2=(0,0,$\frac{c_0}{10}$), O_1=(-$\frac{3a_0 tan(\pi/6)}{10}$,-$\frac{3a_0 cos(\pi/6}{10}$,0), O_2=(-$\frac{3a_0 tan(\pi/6)}{10}$,$\frac{3a_0 cos(\pi/6}{10}$,0) and O_3=($\frac{3a_0}{10}$,0,0), while only O_3 is changed into (-$\frac{3a_0}{10}$,0,0) in motive #2. These two motives are associated to two orthogonal canvas oriented along x=[1$\bar{2}$10], y=[10$\bar{1}$0] and z=[0001] that allow the 3D mapping of whatever α-Al_2O_3 nano-object (particles, but also wires or thin films) with highly-discretized surfaces. Canvas #2 is shifted from canvas #1 by $\overrightarrow{t}$=(a_0, a_0.tan(π/6)/2,−c_0/6), both canvas grid coordinates are defined by the same following set of equations,

$$c_{x(i,j,k)} = i.a_0 + j.a_0.cos(\pi/3) + k.a_0.cos(\pi/3) \tag{4.1}$$

$$c_{y(i,j,k)} = j.a_0.sin(\pi/3) + k.a_0.cos(\pi/3).tan(\pi/6) \tag{4.2}$$

$$c_{z(i,j,k)} = k.c_0/3 \tag{4.3}$$

where i, j and k are integer variables that allow the mapping of the entire 3D space.

To build a neutral nanosphere, both canvas are truncated using the sphere definition (Equation 4.4). The truncation operation is performed at the grid stage *i.e.,* before applying the molecular motive to not split alumina molecules and avoid non-stoechiometric configurations as shown Figure 4.4. In the following, the final built configuration will be referred as "as built".

$$(c_x - x_c)^2 + (c_y - y_c)^2 + (c_z - z_c)^2 \leq r^2 \tag{4.4}$$

where (x_c, y_c, z_c) are the coordinates of the sphere centre and r its radius.

4.2 NP characterization

4.2.1 Equilibration and surface reconstruction

After the fabrication of charged and neutral NPs of various sizes, they are relaxed using the Vashishta interatomic potential to adjust atomic positions. Firstly, the NP energy is minimized using the CG algorithm and free boundary conditions with a force norm criterion set to 10^{-6} eV/Å. Then, the minimized configurations are heated up for 30 ps using the NVE thermodynamic ensemble and a timestep of 1 ps. Two sample benches are set

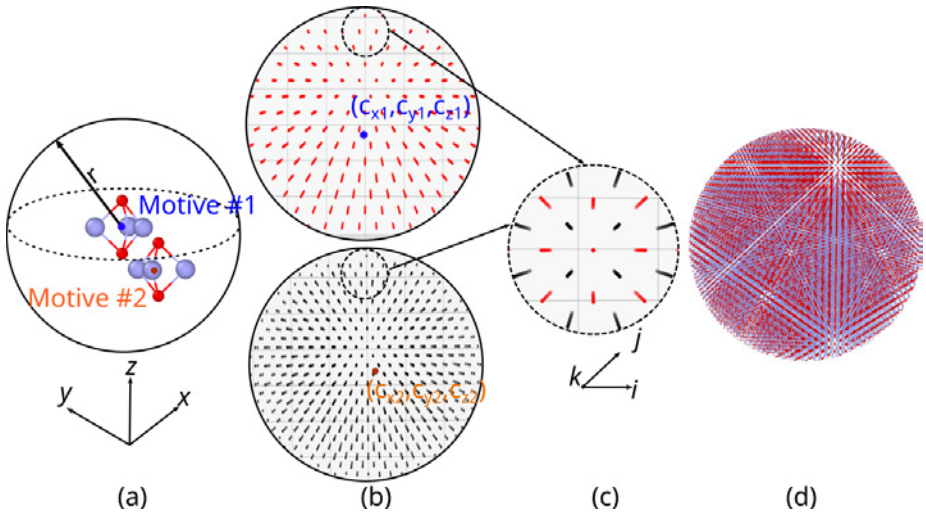

Figure 4.4: Numerical fabrication of neutral NPs using the pattern-based method, (a) Two neutral elementary motives are first defined as well as (b) two canvas: the red grid relies to canvas #1, the gray one to canvas #2. (c) Canvas are merged and cut to design of the NP, (d) The two motives are pasted at each node of the canvas leading to the design of a neutral α-Al_2O_3 NP.

with target heating temperatures of 600 and 1000 K, respectively. Afterwards, NPs are equilibrated using the NVT ensemble and the Noosé-Hoover thermostat for another 50 ps. After the equilibration process, the 600 K bench is cooled down to 5 K while the rest is saved aside for high-temperature tests.

Figure 4.5 show slices of 7 nm diameter NPs before and after the aforementioned equilibration process. For a sake of clarity, only the O atom sublattice is shown on the figure. The O sublattice crystalline structure is characterized as HCP using the Ackland-Jones algorithm [ACK 06] of OVITO.
α-Al_2O_3 NPs show surface reconstruction during the whole equilibration process. In particular, surface reconstruction is strengthened during the high-temperature equilibration process when compared to the minimization. After minimization, the charged particle shows more numerous atomic displacements when compared to the neutral NP based on the displacement vector analysis (see Figure 4.5). The atomic displacements of the two types of NP are of comparable amplitudes at this stage. This behaviour is modified when heating where the neutral NP shows surface localized displacements of slightly larger amplitude (but still less numerous). In addition, surface reconstruction within the neutral NP seems anisotropic with more atomic reorganization observed close to the (0001) surfaces especially during the energy minimization.

After heating up to 600 K and quenching down to 5 K, the average potential energy per atom is -6.237 eV/atom for the charged 7 nm NP while it is reduced to -6.251 eV/atom in the case of the neutral system (ΔE=0.014 eV/atom). The per atom ΔE decreases

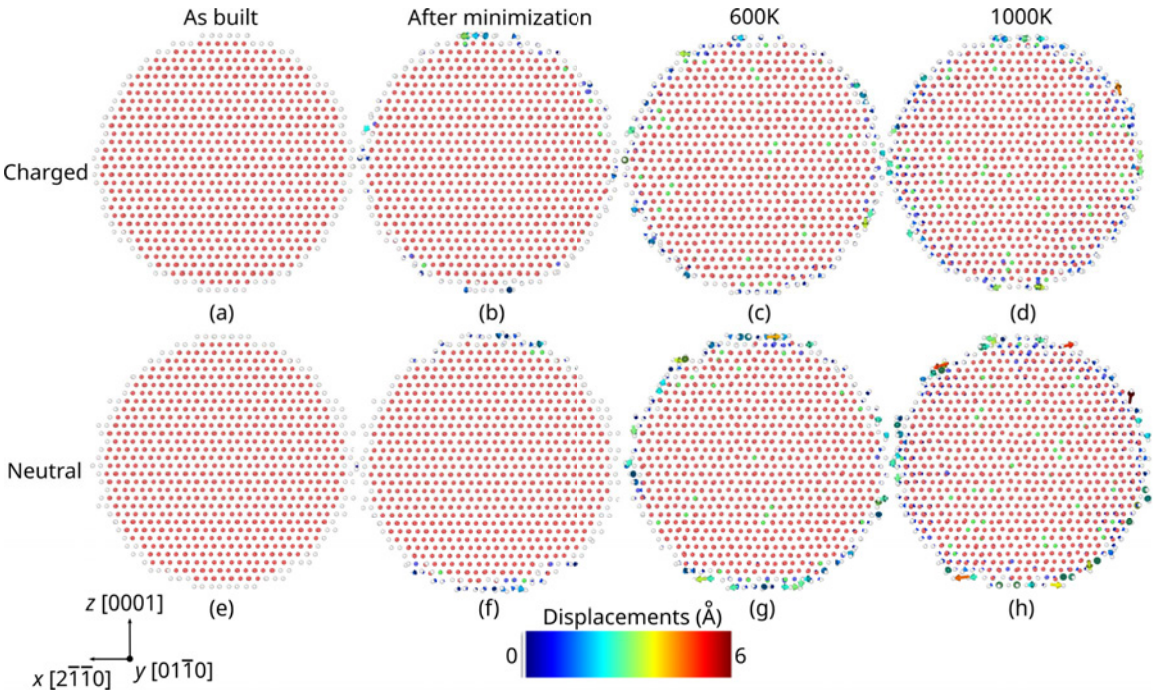

Figure 4.5: Surface reconstruction of α-Al_2O_3 7 nm diameter NP (a,e) as built neutral and charged NPs, (b,f) after energy minimization, (c,g) after equilibration at 600 K and (d,h) after equilibration at 1000 K. Only the O sublattice is shown for a sake of clarity. Atoms colored in light-grey, blue and green refer to defective local structures while red one refer to the original HCP structure of the O sublattice as given by the Ackland-Jones algorithm of OVITO. Colored arrows refer to atomic displacements with the as build configuration taken as a reference.

increasing the sample size (ΔE=0.003 eV/atom for the 15.1 nm diameter NPs) but the absolute energy variation still increases. One can note that the equilibration process increases this energy difference that was originally of 0.01 eV/atom only (in the 7 nm NP) after the first minimization what confirms the importance of the high-temperature equilibration processes when applied to atomistic fabrication of α-Al_2O_3 NPs. Figure 4.6 shows surface distribution of potential energy per atom for 7 nm charged and neutral α-Al_2O_3 NPs. Overall, results show that the local potential energy is larger at the surface than inside the NP. On the other side, the surface energy pattern of the charged NP is strongly heterogeneous (when compared to the neutral one) at the beginning of the minimization. After equilibration, heterogeneities are reduced but still persist leading to a slightly more elevated energy of the charged NP.

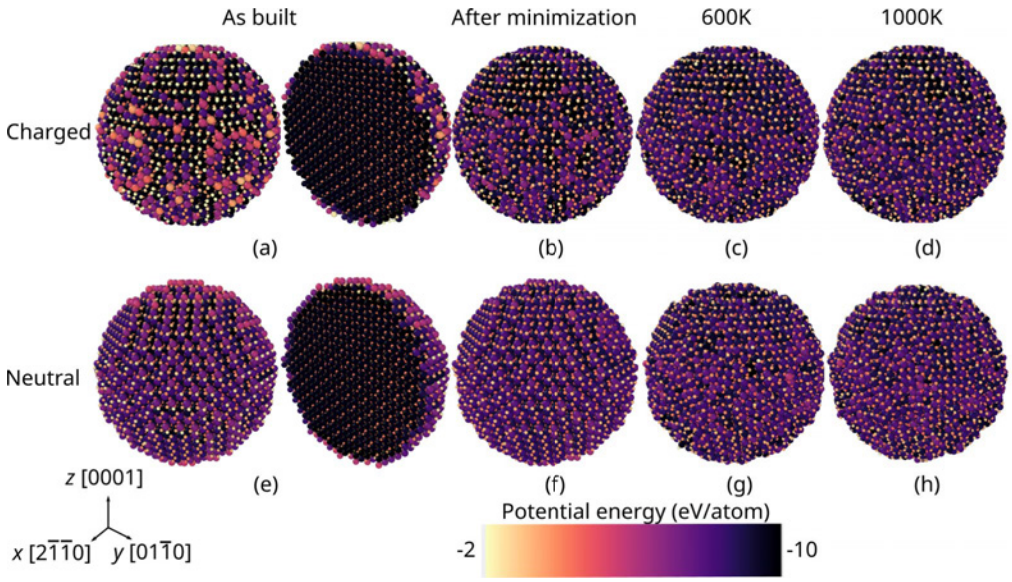

Figure 4.6: Local potential energy distribution for 7 nm diameter charged and neutral α-Al_2O_3 NPs. (a,e) as built neutral and charged samples (starting minimization), (b,f) after minimization, (c,g) after equilibration at 600 K and (d,h) after equilibration at 1000 K.

4.2.2 Bonds analysis

The RDF $g(r)$ provides the probability density to find neighbor atoms in the vicinity of a reference atom [WAR 34]. In case of binary alloys, the partial RDF $g_{ij}(r)$ can be defined as,

$$g_{ij}(r) = \frac{n_{ij}(r, r + \Delta r)}{4\pi r^2 \Delta r \rho c_j} \tag{4.5}$$

where i and j rely the two atom species, $n_{ij}(r, r + \Delta r)$ is the average number of atom j surrounding an atom i which is at a distance between r and $r + \Delta r$. ρ is the material density and c_j is the concentration of j particles.

The figure 4.7 describes partial RDFs for the 7 nm diameter neutral NP before and after equilibration. At LT, RDFs exhibit a series of sharp and discrete peaks at specific interatomic spacings in agreement with the crystalline structure. As expected, the peaks progressively broaden when heating at 600 K and then at 1000 K due to atomic vibration. In particular, one can recognize after minimization the a_0=4.72 Å, the first Al-Al distance of about 2.55 Å and the first Al-O distance *c.a.*, 1.89 Å which are typical of the α-Al_2O_3 crystal structure. For the Al-Al pair in the "as build" configuration, the first peak in $g_{AlAl}(r)$ occurs at 2.79±0.01 Å, which corresponds to the Al–Al bond length. While after minimization, the first peak is around 2.55±0.01 Å. For equilibration at 600 K and 1000 K, the first peak is observed at 2.79±0.01 Å again. The O-O pair relax slightly differently with the first peak shifted from 2.49±0.01 Å to 2.55±0.01 Å after minimization (2.73±0.01

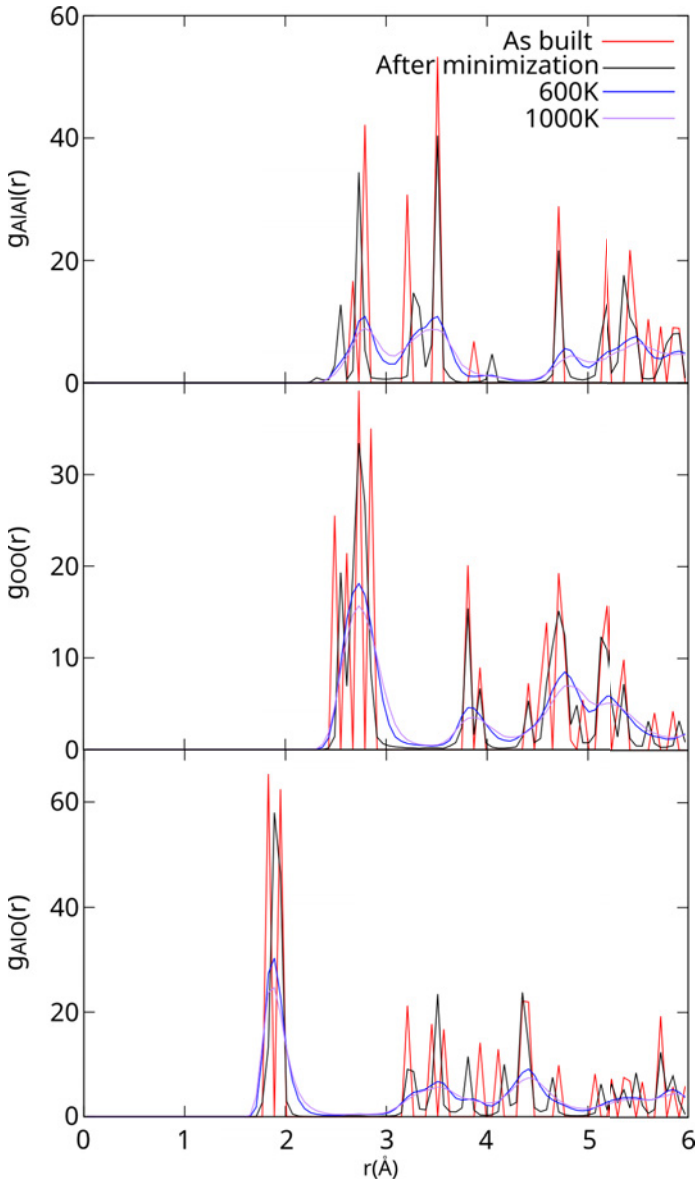

Figure 4.7: RDF for Al-Al, O-O and Al-O pairs computed in the α-Al_2O_3 7 nm neutral. As built, after minimization and after equilibration at 600 K and 1000 K data are shown.

Å after heating). Finally, Al-O pairs in the "as build" configuration shows a first peak at 1.83±0.01 Å which corresponds to the Al-O bond length, 1.89±0.01 Å after minimization and 1.89±0.01 Å again after heating. Finally, as the temperature increases, discrete peaks vanish and only few peaks can be recognized for the the three pairs of bonds with the first neighbor Al-O distance being the shorter bond whatever the temperature.

In the next chapter, neutral samples of various sizes will be used to investigate the mechanical properties and elementary deformation processes of α-Al_2O_3 under compression.

Chapter IV summary:

In this chapter, we first introduced the two methods we used to model α-Al_2O_3 nanospheres: (i) the classical cutting-block method that consists in slicing an original block of atoms using cutting planes. While being easy to used, this method generally leads to charged alumina nanospheres, (ii) the newly-developed pattern-based method that allows to build neutral NPs based on molecular motives replicated on a periodic canvas. Then, the equilibration process for the both types of nanospheres is presented and the samples are characterized. Energy analysis shows the higher stability of the neutral NPs for which a bond analysis is also presented.

Chapter 5

Nanocompression of α-Al_2O_3 nanoparticles

In contrast with bulk materials, NPs can bear extremely high stresses (in the GPa range) and exhibit a significant ductility due to their original lack of defects as discussed in Chapter 1. As a reminder, Gerberich and coworkers show that 20–50 nm silicon nanospheres are characterized by a hardness ranging from 20 to 50 GPa [GER 03]. Also, an impressive 34 GPa compression strength was obtained for 210 nm Ni NPs [SHA 18]. Another interesting observation is the increase of the fracture toughness while NP size decreases [BEA 11]. It is worth to mention that these particular behaviours appear in materials such as silicon and oxide ceramics, generally considered as brittle at the macro-scale, that can deform plastically without cracking when in the form of NPs [MOO 07, GER 12, ISS 15]. This original nanoscale behaviour is attributed to a new kind of plasticity based on the dislocation nucleation process.
In this chapter, we focus on the modeling of α-Al_2O_3 nanospheres under compression using MD simulations with emphasis on the elementary deformation processes. Both elastic and plastic properties during nanocompression are investigated. The MD outcomes are discussed in the light of recent nanomechanical experiments and pioneer studies conducted on bulk alumina.

5.1 Methods

We perform MD simulations to investigate the deformation of α-Al_2O_3 NPs under compression using the open-source code LAMMPS [PLI 95]. All MD calculations are carried out using the 2/3-body Vashishta potential [VAS 08] that is able to reproduce α-Al_2O_3 properties such as lattice, surface, stacking fault and dislocations properties with good accuracy when compared to DFT and experiments (see Chapter 3). These properties are of

primary importance when looking for interatomic potential transferability to nanomechanics. For these simulations, a cut-off parameter of 6 Å is used for short-range interactions as in previous simulations (see Chapter Chapter 3). Neutral α-Al_2O_3 nanospheres (see fabrication method in Chapter Chapter 4) with diameters ranging from 7.2 to 15.2 nm are investigated using CA normal to the basal plane, prismatic a and m planes as well as a rhombohedral plane.
The MD compression simulations are performed using the procedure developed by Amodeo and collaborators (see *e.g.,* [ISS 15, AMO 17]). After the NPs equilibration (see fabrication method in Chapter Chapter 4), the nanocompression test is performed using two infinite top and bottom force fields which behave respectively as a flat punch and a substrate. Initial minimum and maximum atomic positions along CA are used to set the initial force field positions and reduce the rebound of the NP after contact (ping-pong effect). Then, the top indenter is displaced at a constant rate equivalent to an engineering strain rate of 10^8 s^{-1} for all particle sizes, while the bottom indenter is kept fixed and sustain the sample as shown in Figure 5.1.

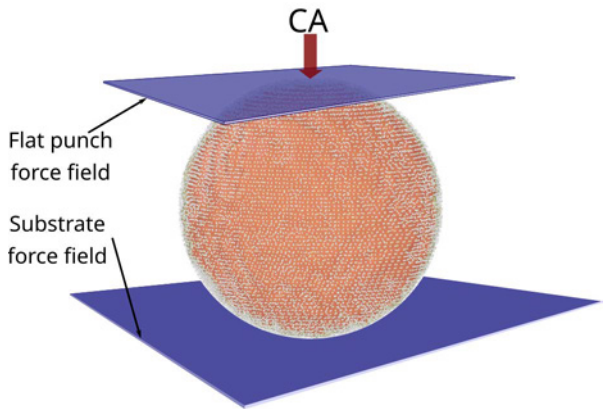

Figure 5.1: MD nanocompression setup showing the two planar force fields surrounding an α-Al_2O_3 NP. CA refers to the compression axis.

The position of the top indenter as function of time $P(t)$ is computed as,

$$P(t) = P_0(1 - \dot{\varepsilon}.n.dt) \tag{5.1}$$

Where P_0 is the starting position of the indenter, $\dot{\varepsilon}$ is the (engineering) strain rate, dt the timestep (1 fs) and n the number of elapsed simulation step. In this study, the engineering strain $\varepsilon = \Delta L/L_0$ is defined as the ratio between the NP size variation along CA and its original diameter. Compression simulations are carried out at 5 and 1000 K constant temperatures using a Nosé-Hoover thermostat. Both indenters are planar and axis-aligned. They behave as infinitely-extent walls exerting the same force on the system. The force f exerted by the indenter on the atoms is defined by Equation (5.2),

$$f = -K \sum_{j=1}^{N} (r_j - R)^2 \tag{5.2}$$

where K is the specified force constant set to 1000 nN·Å^{-2}, $r_J - R$ is the distance from the atom j to the indenter. Within the LAMMPS procedure, the moving indenter squeezes the NP and f applies to the N atoms positioned over the indenter *i.e.,* the force is repulsive and $F(r) = 0$ for $r > R$.

As already mentioned, we have investigated the mechanical response of α-Al_2O_3 nanospheres for various CA orientations. But whatever CA, the mechanical response can be divided into two stages including an elastic and a plastic regime.
Due to the spherical shape of the NPs, we only use the contact force f to characterize the mechanical response in the following (see discussions in Refs. [AMO 17, AMO 21] for more details). In addition, f can be modeled using the Hertz contact theory within the elastic regime [JOH 87],

$$f(\delta) = \frac{4}{3} E^* R^{\frac{1}{2}} \delta^{\frac{3}{2}} \tag{5.3}$$

where E^* is an effective Young's modulus, R is the nanosphere radius and δ the cumulative displacement.

Both force *vs.* displacements and force *vs.* strain curves are discussed in the following. As already observed in other kinds of NPs, the transition between both deformation regimes is attributed to the nucleation of defects from the surface of the NPs that further propagate and interact inside the sample. Elementary deformation mechanisms as function of orientation is described with care in the following using the Lee and Lagerlof orientation table [LEE 85] adapted in Figure 5.2. The Lee and Lagerlof table allows to identify the angle θ between low-index planes in α-Al_2O_3 as *e.g.,* between CA and possible slip planes. θ can be computed using the three-index Miller notation (u, v, w) (rather than the four-index Miller-Bravais system) using the following equation,

$$cos(\theta) = \frac{a_0^2((u_1u_2 + v_1v_2) - 1/2(v_1u_2 + v_1u_2)) + c_0^2 w_1 w_2}{\sqrt{a_0^2(u_1^2 - v_1u_1 + v_1^2) + c_0^2 w_1^2}\sqrt{a_0^2(u_2^2 - v_2u_2 + v_2^2) + c_0^2 w_2^2}} \tag{5.4}$$

with the two crystallographic planes of interest defined by $(u_1, v_1, (t_1), w_1)$ and $(u_2, v_2, (t_2), w_2)$.

OVITO's crystallography and dislocation analysis are complementary used. For this purpose, the α-Al_2O_3 atomic structure is generally reduced removing the Al sublattice for the analysis. Doing so, OVITO interprets the O sublattice as a monoatomic HCP material allowing various analysis in a similar way than in HCP metals.

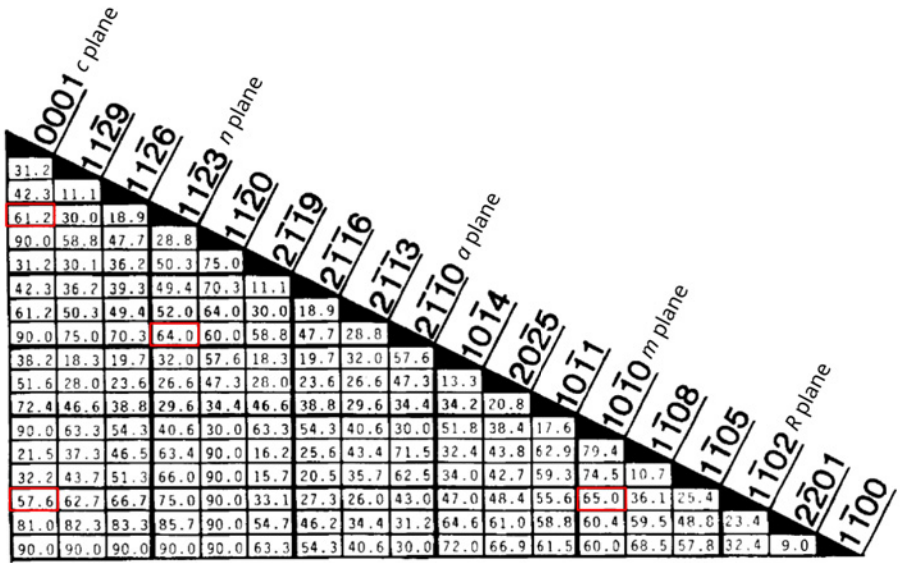

Figure 5.2: Angles between low-index planes in α-Al_2O_3. Orientations characterized in our nanocompression simulations are emphasized in red. Adapted from Ref. [LEE 85].

5.2 5K compression simulations

Here we present a set of compression simulations performed at low temperature *c.a.,* 5K. Three sample with diameters of 7.2, 10.1 and 15.2 nm are investigated for different orientations. All NPs are deformed at least up to 25% strain without any sign of fracture. Changing size allows for repeatability checks. Similar deformation processes are observed whatever the NP size for a given orientation *i.e.,* changing size only influences the load-displacement mechanical response. Thus, only elementary deformation processes associated with the largest sample are described in the following.

5.2.1 Compression normal to the c plane (0001)

Mechanical response

The first samples we investigate here are oriented with CA perpendicular to the c plane. Figure 5.3 shows force *vs.* displacement and strain curves for the three investigated NP sizes. In the elastic regime, the loading force increases linearly with strain after a short period of accommodation between samples and indenters while a non-linear behaviour is observed when plotting force *vs.* displacement. According to the Hertz model, the effective Young's modulus E^* are about 167, 190 and 191 GPa respectively for the 7.2, 10.1 and 15.2 nm NPs. The boundaries used for the Hertz fit are set to 3.5 and 12.5% for the 7.2 nm NP, 3.5 and 13.0% for the 10.1 nm NP and 5.0 and 17.8% for the 15.2 nm NP, respectively. It is worth noticing that E^* values should not be compared to bulk-alumina

Young's modulus due to the nanosphere stress state (see Ref. [AMO 21] for a detailed discussion) but one can emphasize that they are already four times larger than those computed in Al nanosphere of comparable size (10 nm, E^*=45.9 GPa) [BIA 13]. At the onset of plasticity, critical strains are about 12.4, 12.6 and 17.8% while the yield force is F_y= 505, 950 and 2186 nN increasing the size of the sample. These mark the beginning of the plastic regime that is characterized by multiple load drops and elastic reload, as shown on the mechanical response (see Figure 5.3).

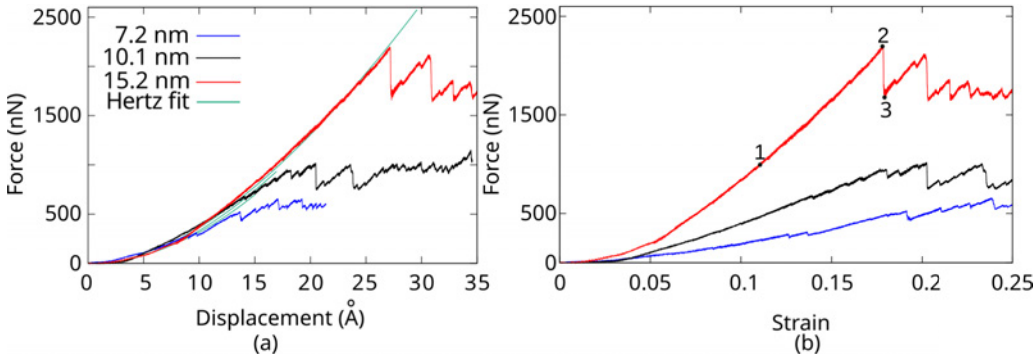

Figure 5.3: Mechanical response of 7.2, 10.1 and 15.2 nm α-Al_2O_3 nanospheres for CA normal to the c plane at 5 K. (a) Force *vs.* displacement curves. The green curves rely on Hertz adjustments. (b) Force *vs* strain curves.

Elementary deformation processes

For the largest sample, the first nucleation event occurs at $\varepsilon = 11.5\%$ (Figure 5.3b, label 1) and a loading force of $F = 1000$ nN where a nanotwin is observed. A close analysis of the slip plane orientation shows a deviation of the slip plane of about 58° from CA what promotes a rhombohedral $\{01\bar{1}2\}$ slip plane as a possible candidate to host the twin when referring to the Lee and Lagerlof table. This angle value (i) is confirmed when applying Equation 5.4 to the $(01\bar{1}2)$ plane and using Vashishta lattice parameters and (ii) is very close to the 57.6° computed by Lee and Lagerlof, what confirms the nucleation of the classical rhombohedral twin [GEI 94, LAG 02]. The DXA analysis of OVITO suggests a Burgers vector of type $[0\bar{1}11]$. The twin nucleates from the contact region between the substrate and the NP as shown in Figure 5.4a. In contrast to the classical twin growth scheme depicted by Kuksin in α-Al_2O_3 [KUK 12], here we did not observe the prior nucleation of a partial dislocation (further growing into a twin) but directly an already-shaped *volumic* defect. After nucleation, the nanotwin propagates a little within the sample but quickly stops explaining the continuous increase of the force recorded *i.e.,* no force drop is observed on the mechanical response at this stage.
Then, the elastic load continue until 17.8% strain (Figure 5.3b, label 2) where the effective beginning of the plastic deformation regime is emphasized by force drop on the curve. At

this stage, a second rhombohedral twin is nucleated within the same slip plane but with opposite gliding direction from the top indenter contact region as shown in Figure 5.4b. This new nanotwin quickly travels through the entire particle forming new TB that reach the NP surface for the first time. The two parallel R twins are spaced from each other and twin growth is observed thanks to successive nucleation and glide events on neighboring $(01\bar{1}2)$ planes leading to the TB migration. At $\varepsilon = 17.9\%$ (Figure 5.3, label 3), a third rhombohedral twin suddenly forms in the $(1\bar{1}02)$ slip plane and intersects with the first two parallel twins (Figures 5.4c). Increasing compression, the third twin creates junctions between existing TBs and the NP surfaces.

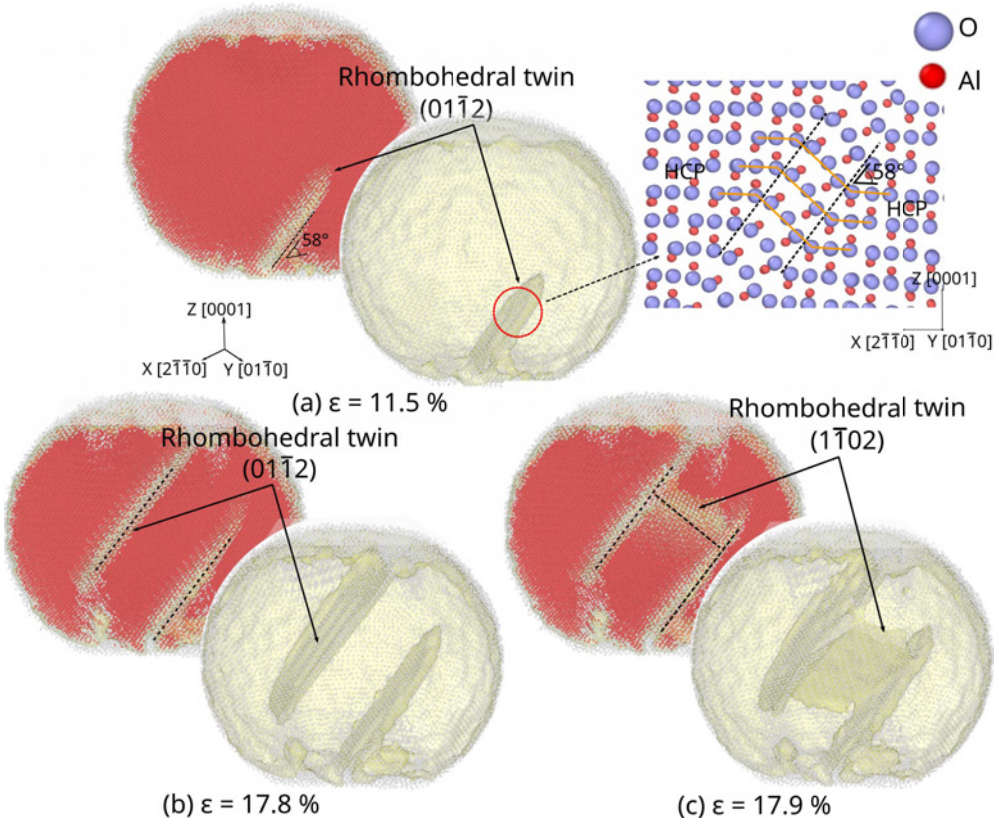

Figure 5.4: Compression of α-Al_2O_3 NPs normal to the c plane at T=5K. The nucleation of rhombohedral twins is shown at (a) 11.5%, (b) 17.8 % and (c) 17.9% strain. Only O atoms (in red when HCP environment, light-grey for defective regions) are shown for a sake of clarity. In addition to the O sublattice images, additional insets are shown. These allow to identify the twins using either a full-atom classical description or interface characterization (colored in yellow).

5.2.2 Compression normal to the a plane $\{1\bar{2}10\}$

Mechanical response

Figure 5.5 shows force *vs.* displacement and strain curves for the three investigated size NPs with CA along the $[1\bar{2}10]$ direction. The effective Young's modulus E^* is about 237, 220 and 239 GPa respectively for the 7.0, 10.0 and 15.1 nm NPs. The boundaries of the Hertz fit range from 2.5 to 7.0% for the 7.0 nm NP, from 1.5 to 7.0% for the 10.0 nm NP and from 1.0 to 9.0% for the 15.1 nm NP. The end of the elastic regime is characterized by F_y=413, 766 and 975 nN, respectively.

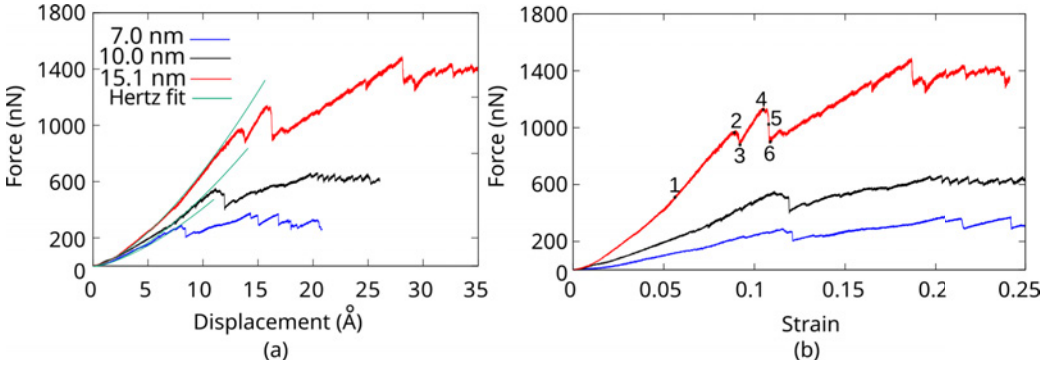

Figure 5.5: Mechanical response of 7.2, 10.1 and 15.1 nm α-Al_2O_3 nanospheres for CA normal to a prism a plane at 5 K. (a) Force *vs.* displacement curves. The green curves rely on Hertz adjustments. (b) Force *vs.* strain curves.

Elementary deformation processes

For the 15.1 nm sample, the first dislocation nucleation event happens at $\varepsilon = 6.0\%$ strain (Figure 5.5b, label 1) and for a loading force F about 550 nN. At this stage, a perfect dislocation nucleates from the top contacting region as shown Figure 5.6a. The dislocation propagates within a slip plane oriented at 64° from CA in agreement with the $(11\bar{2}3)$ pyramidal n plane following Lee and Lagerlof table 5.2. Here again the dislocation quickly stops gliding after nucleation what explains the lack of force drop on the mechanical response as in the case of the basal compression test. The atomic configuration in the vicinity of the pyramidal dislocation core is highly disordered as also observed by Zhang *et al.* using the same interatomic potential [ZHA 08].

Between $\varepsilon = 9.0\%$ and 9.5% (Figure 5.5b,c, labels 2 and 3), two $(11\bar{2}3)$ and $(1\bar{2}13)$ pyramidal dislocations nucleate from the NP bottom region making a triangular dislocation structure (Figure 5.6b), in a similar manner than the pyramidal dislocation structure observed in FCC metals [BIA 13, SAL 18, GOR 19]. While the compression proceeds, a second force drop of larger amplitude is observed at $\varepsilon = 10.6\%$ (Figure 5.5b, labels 4,5 and 6) and is attributed to the propagation of a new pyramidal dislocations from the hillock of the triangle structure (Figure 5.6d). These dislocations are of different type with respect to the perfect one of Figure 5.6a,b,c. Indeed, they are partial dislocations followed

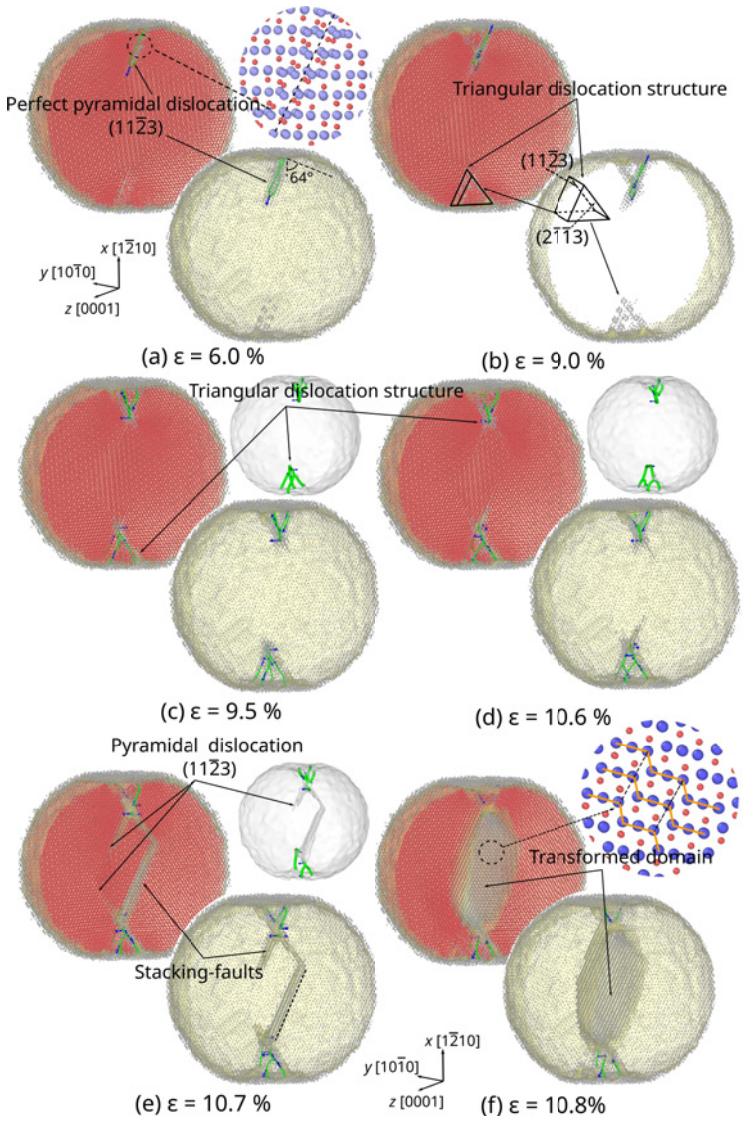

Figure 5.6: Compression of α-Al_2O_3 NPs normal to the prism a plane at T=5K. Only O atoms (in red when HCP environment, light-grey for defective regions) are shown for a sake of clarity. Perfect dislocations are shown in green curves. (a,c) The first nucleation events are characterized by the nucleation and propagation of $(11\bar{2}3)$ and $(1\bar{2}13)$ perfect dislocations forming a triangular dislocation structure. (d,e) The triangular dislocation structure fails at ε=10.6% where partial dislocation multiply within same pyramidal slip planes (staking-faults are emphasized using yellow interfaces, partial dislocations are not emphasized). (f) The accumulation of closed stacking-faults in the pyramidal planes lead to structural change between the lateral and the central domain of the NP. In addition to the O sublattice images, additional insets are shown. These allow to identify the defective regions either using the full-atom classical description or interface characterization (colored in yellow).

by stacking-faults which are recognized by OVITO. The triangular structures definitely breaks at $\varepsilon = 10.7\%$ Figure 5.5b, label 5) where multiple partial dislocations propagate in close and parallel slip planes. Finally, the propagation of the pyramidal partial dislocations leads to a structural change between the lateral and central domains of the NP as

shown Figure 5.5e,f.

5.2.3 Compression normal to the m plane $\{10\bar{1}0\}$

Mechanical response

The third sample set is compressed with CA normal to a prism m plane. Figure 5.7 shows the mechanical response. According to the Hertz model, the effective Young's modulus E^* is about 189, 195 and 203 GPa respectively for the 7.3, 10.1 and 15.2 nm NPs. The limits of the Hertz fit are 5.0 to 9.0% for the 7.2 nm NP, from 6.0 to 11.0% for the 10.1 nm, from 5.0 to 8.5% for the 15.2 nm NP. Critical strains and yield force are about 13.0, 12.1 and 13.1% and F_y=339, 637 and 1542 nN respectively.

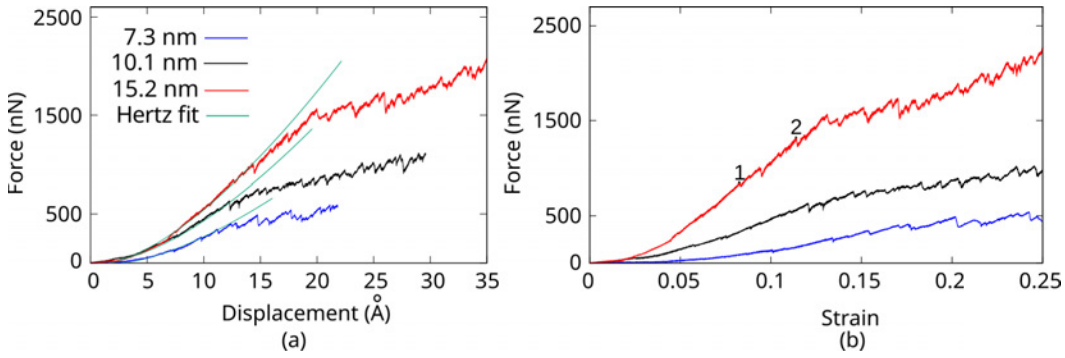

Figure 5.7: Mechanical response of 7.2, 10.1 and 15.2 nm α-Al_2O_3 nanospheres for CA normal to a m plane at 5 K. (a) Force *vs.* displacement curves. The green curves rely on Hertz adjustments. (b) Force *vs* strain curves.

Elementary deformation processes

The first nucleation event happens at $\varepsilon = 8.5\%$ (Figure 5.7b, label 1) and at a loading force about F=810 nN. Few partial dislocations with Burgers vectors of type $\frac{1}{3}[10\bar{1}0]$ (as emphasized by OVITO) nucleate and propagate in the c plane that is 3° off from CA (Figure 5.8a to c). One can note that (i) originally, the c plane is supposed to be perpendicular to CA (leading the a null Schmid factor) but basal slip is here activated due to a slight rotation of the NP happening at the beginning of the compression (see Figure 5.8a and b) and (ii) OVITO is able here to recognize the exact Burgers vector as being a classical one of HCP monoatomic metals. This event starts from the two contact regions and is extremely localized as shown Figure 5.8c and d *i.e.,* several partial dislocations nucleate in planes separated of 2 or 4 interplanar distances (without making twin). In this case, no clear force drop is noticed on the mechanical response but only low amplitude hints leading to a global hardening behaviour. These are attributed to further nucleation events that

contradict the basal dislocations propagation which is already impeded by the low-Schmid factor orientation. Indeed, as shown Figure 5.8d, one can notice plastic activity in an other slip plane starting from $\varepsilon = 11.5\%$ (Figure 5.7, label 2) including several dislocation nucleation events that happen in a similar manner that aforementioned partial basal dislocations (in close planes). The activated slip plane makes an angle of 65° with CA which is suggests R plane following Lee and Lagerlof method and owing the initial rotation of the NP. Between 11.5 % and 25 %, both slip system activities compete together with plasticity strictly localized in the close-to-the-indent regions. No expansion of the dislocations is observed in the central domain of the NP assuming (i) an orientation particularly not suitable for plastic deformation and (ii) a larger elastic contribution specific to this orientation.

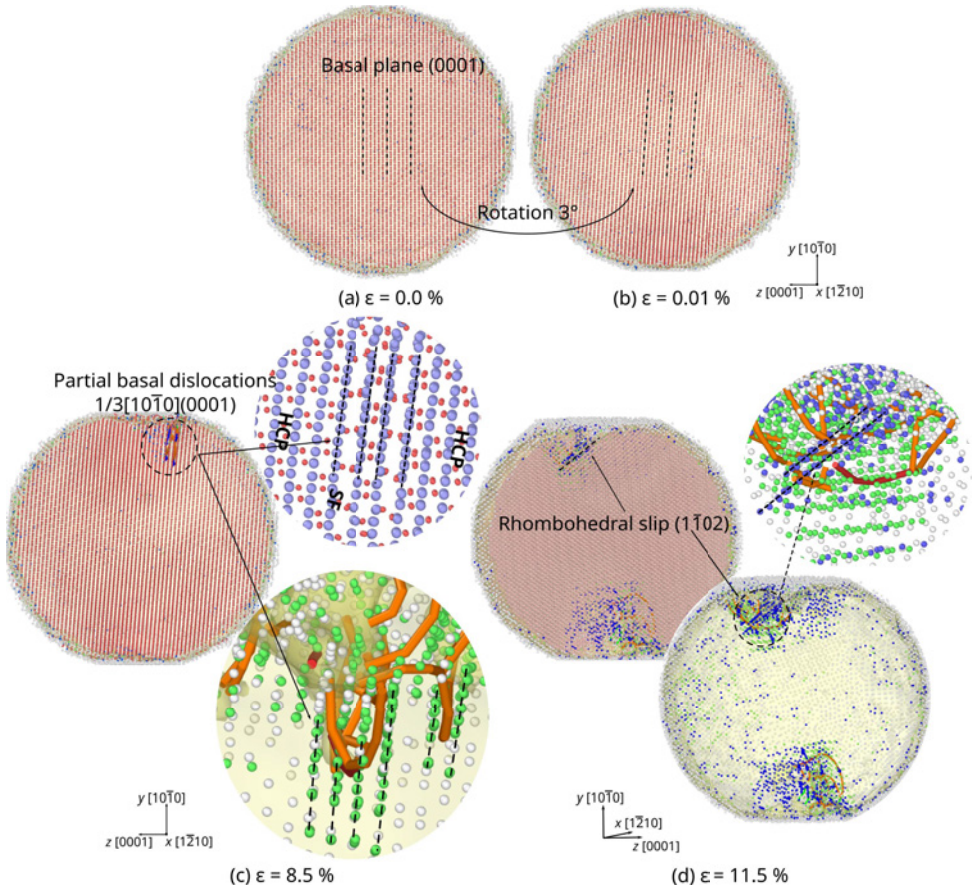

Figure 5.8: Compression of α-Al_2O_3 NPs normal to the prism m plane at T=5K. Only O atoms are shown for a sake of clarity. (a:b) Illustration of 3° angle tilt observed during compression accommodation as shown using the basal plane orientation. (c) ϵ=8.5%, partial basal dislocations nucleate from the contact region with the indenter. Dislocations colored in orange refer to $\frac{1}{3}[10\bar{1}0]$ dislocations (atoms colored in green rely to the stacking-faults). (d) ϵ=11,5%, Rhombohedral slip is identified (atoms colored in blue refer to stacking-fault) interfering with basal dislocations.

5.2.4 Compression normal to the R plane $\{10\bar{1}2\}$

Mechanical response

Figure 5.9 shows force *vs.* displacement and strain curves for the three investigated size NPs compressed with CA perpendicular to an R plane. The effective Young's modulus E^* is about 258, 247 and 248 GPa respectively for the 7.0, 9.5 and 15.1 nm NPs. The boundaries of the Hertz fit are located between 1.5 and 7.5% for the 7.0 nm NP, between 1.0 and 8.0% for the 9.5 nm NP and between 0.5 and 7.8% for the 15.1 nm NP. The yield force is characterized at F_y=249, 397 and 806 nN increasing the system size.

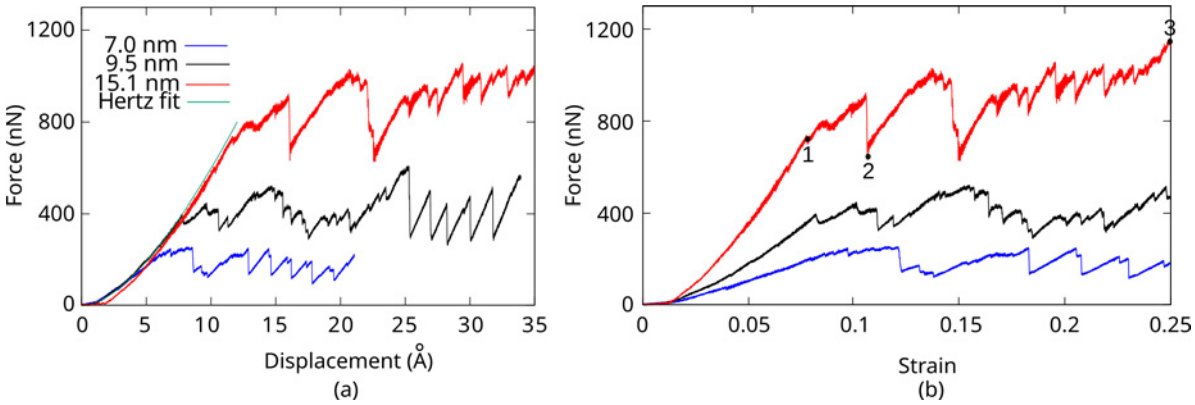

Figure 5.9: Mechanical response of 7.2, 9.5 and 15.1 nm α-Al_2O_3 nanospheres for CA normal to an R plane at 5 K. (a) Force *vs.* displacement curves. The green curves rely on Hertz adjustements. (b) Force *vs* strain curves.

Elementary deformation processes

The first nucleation event in the 15.1 nm NP occurs at ε=7.8% (Figure 5.9b, label 1). At this stage, a dissociated $\frac{1}{3}[1\bar{2}10](0001)$ dislocations nucleates from the contact region between the substrate and the NP as shown Figure 5.10a,b. Figure 5.10a shows that the dislocation is dissociated into two $\frac{1}{3}\langle 01\bar{1}0\rangle$ partial dislocations separated by a stacking-fault. In this case, the gliding plane is positioned between two puckered Al layers as in the Bilde-Sørensen model for basal edge dislocation [BIL 96]. After ε=7.8%, several paralleled basal dislocations with similar Burger vectors nucleate from the contact regions of the NP with the indenter and the substrate. Those dislocations often cross-slip towards adjacent basal planes. Few $(11\bar{2}3)$ pyramidal (perfect) dislocations are also observed (Figure 5.10c). They are always connected to a basal dislocation and are generated by the cross-slip of a screw segment. At larger strain (Figure 5.10d), structural changes associated to the glide of multiple pyramidal partial dislocations are observed similarly to the case when compressing along prism a (Figure 5.6).

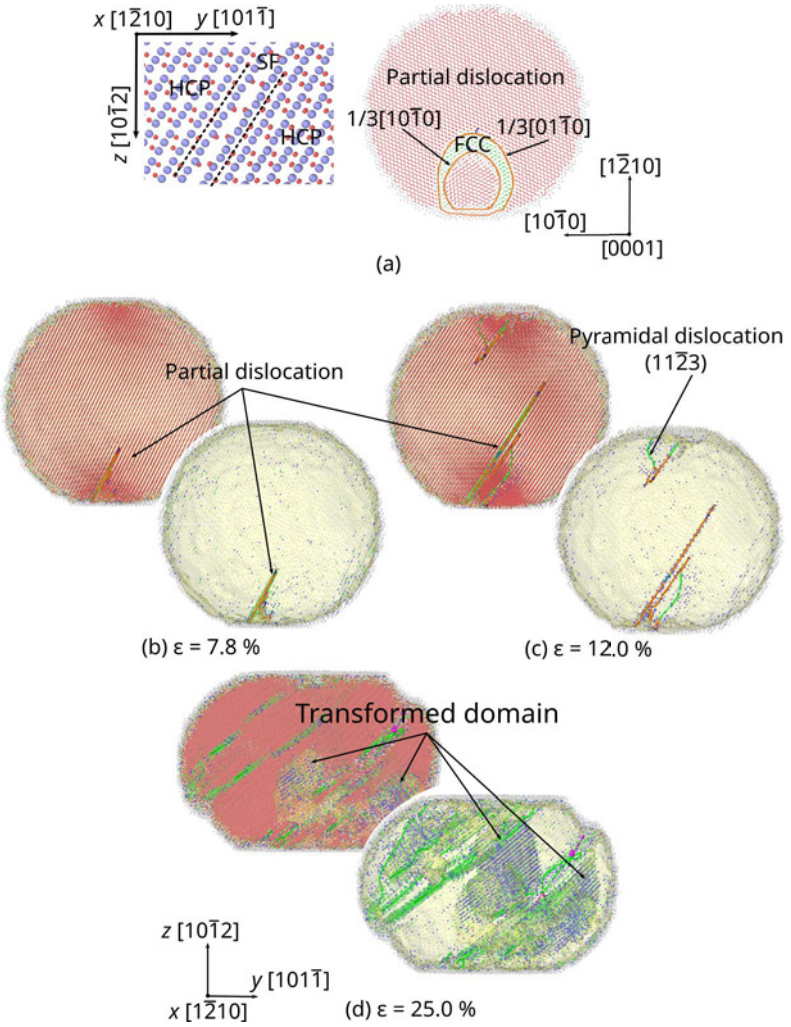

Figure 5.10: Compression of α-Al_2O_3 NP with CA normal to a rhombohedral R plane at T=5K. Only O atoms are shown in red for a sake of clarity. Surfaces and defective regions as GBs are shown by atoms colored in light-grey and yellow area (interfaces). (a,b) Nucleation of $\frac{1}{3}\langle 01\bar{1}0\rangle$ partial dislocations between 7.8% and 12% strain (dislocation colored in orange, stacking fault atoms in green). (c) Basal and pyramidal (colored in green) dislocations nucleating and propagating at 12% strain. (d) Basal partial dislocations gliding in close planes close to transformed domains associated to the propagation of pyramidal n partial dislocations (stacking-fault atoms colored in blue).

As described in the previous subsections, the deformation of α-Al_2O_3 NPs strongly depends on CA orientation. For each CA, Table 5.1 resumes the effective Young's modulus $\langle E^* \rangle$ (size average), the yield force F_y of the largest NP and the plastic deformation mechanisms observed. The largest value of $\langle E^* \rangle$ is noticed for CA normal to R plane that does not corresponds to the largest F_y orientation *i.e.,* [0001]. Various deformation mechanisms were observed including rhombohedral twinning and pyramidal slip for CA normal to c and a planes, basal (0001) and rhombohedral dislocations for CA normal to

m plane and finally basal and pyramidal slip for CA normal to the R plane. One can note that basal and pyramidal slips often lead to highly-deformed domains related to the adjacency of their respective stacking-faults.

CA	$\langle E^* \rangle$ [GPa]	F_y [nN]	Plasticity process
c	183	2186	R twinning
a	232	975	Pyramidal slip (perfects + partials)
m	196	1542	c and R slip (partials)
R	251	806	c and pyramidal slip (partials)

Table 5.1: Effective Young's modulus $\langle E^* \rangle$ (size averaged), yield force F_y (for largest size NPs 15.2 nm) and elementary plasticity processes as function of CA observed in α-Al_2O_3 NPs compressed at T=5K.

5.3 1000K compression simulations

In this section, we present a set of compression simulations performed on same samples (size and orientation) but at higher temperature T=1000K. This temperature is about half the melting temperature of alumina and can be associated to an early-stage of sintering temperature in the experimental conditions. For a sake of convenience, only the mechanical response of the 15.2 nm diameter sample is discussed and compared to the LT tests. Force *vs.* strain curves are shown and adjusted using the Hertz model (Equation (5.3)) in which the displacement δ is replaced by $\varepsilon.d_0$, where d_0 is the original diameter size of the NP. In addition to the raw data, a Bezier fit is also shown as reducing the mechanical response fluctuations associated to high temperature atomic vibrations.

5.3.1 Compression normal to the c plane (0001)

Mechanical response

First we investigate compression performed with CA normal to the c plane. Figure 5.11 shows force *vs.* strain curves for the 15.2 nm size NP as compared to the LT test. The effective Young's modulus E^* is about 127 GPa using the Hertz fit boundaries at 1.0 and 9.4% strains. The end of the elastic regime is characterized by F_y=1020 nN.

Elementary deformation processes

The first dislocation is observed at ε = 5.4% (Figure 5.11, label 1) and at a loading force about F=400 nN. As in the LT case, the plastic deformation process of α-Al_2 O_3 NPs compressed along the c direction at T=1000 is rhombohedral twinning (Figure 5.12).

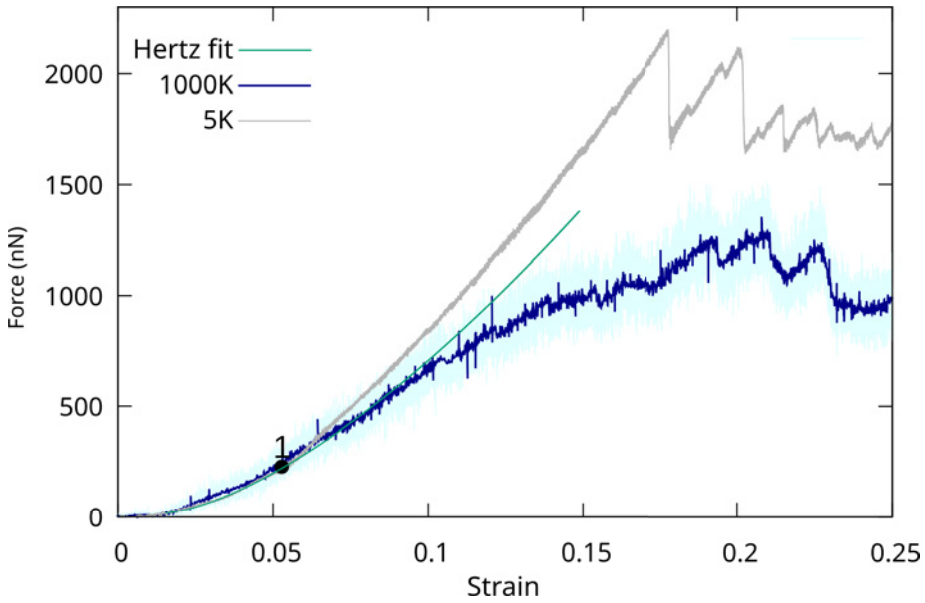

Figure 5.11: Force *vs.* strain response of a 15.1 nm diameter α-Al_2O_3 nanosphere for CA normal to the c plane at T=1000 K. The light-blue curve refers to the raw data while the dark-blue one is a Bezier fit. Elastic Hertz fit is shown in green. Data computed at T=5K (grey curve) are shown for comparison.

As the twin nucleate and propagate in a similar manner than in the T=5K case, the reader can refer to section 5.2.1 fore more details the slip process.

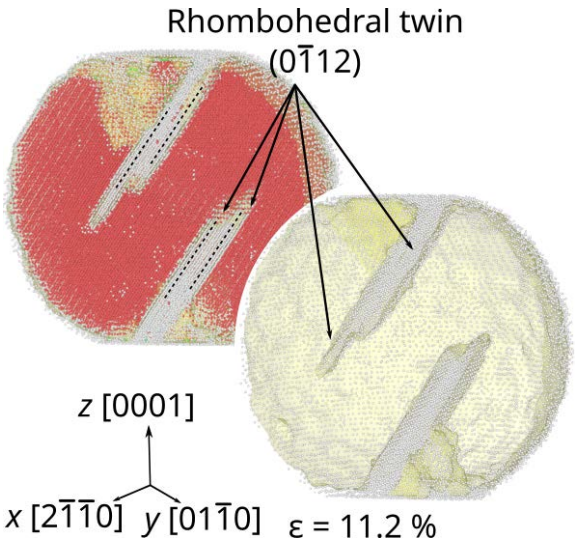

Figure 5.12: Rhombohedral twin nucleation during the nanocompression of α-Al_2O_3 NPs for CA normal to the c plane at T=1000K. Only O atoms (in red when HCP environment, light-grey for defective regions) are shown for a sake of clarity. An additional insets emphasize the nanotwins (colored in yellow) using interface characterization.

5.3.2 Compression normal to the a plane $\{1\bar{2}10\}$

Mechanical response

Figure 5.13 shows the force *vs.* strain response computed at T=1000K with CA normal to a prism a plane as compared to the LT respective test. Both curves show very similar behaviours but a lower load for the HT test. The effective Young's modulus E^* is about 154 GPa using boundaries of the Hertz fit between 0.5% and 8.0% strains. The beginning of the plastic regime is characterized by F_y=849 nN.

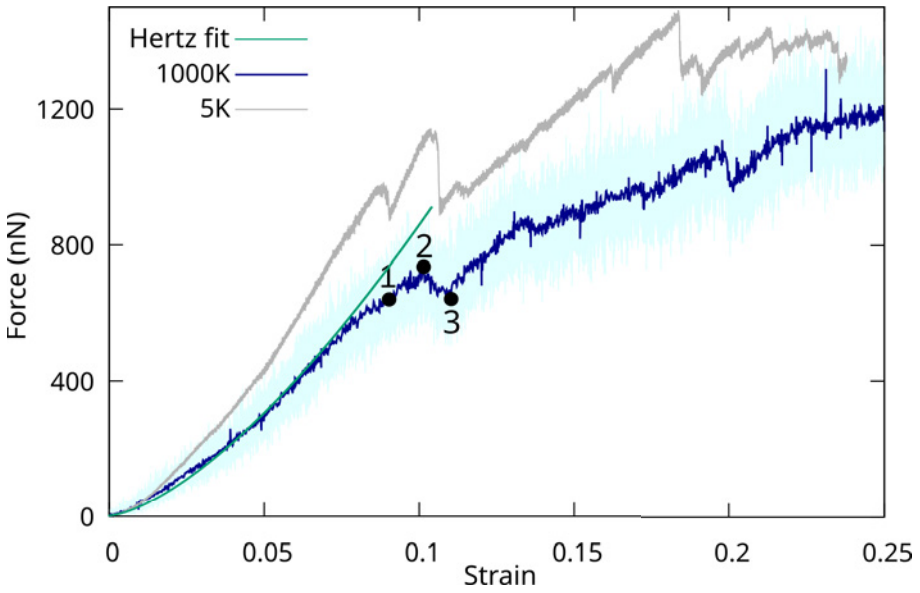

Figure 5.13: Force *vs.* strain response of a 15.1 nm diameter α-Al_2O_3 nanosphere under compression at T=1000 K with CA normal to a prismatic a plane. The light-blue curve refers to the raw data while the dark-blue one is a Bezier fit. Data computed at T=5K (grey curve) are shown for comparison.

Elementary deformation processes

As shown Figure 5.14, the first nucleation occurs at $\varepsilon = 9.3\%$ (Figure 5.13, label 1) and a loading force about F=600 nN where a perfect $(11\bar{2}3)$ pyramidal n dislocation grows from the bottom region of the nanosphere (Figure 5.6a). The dislocation propagate within the $(11\bar{2}3)$ pyramidal plane at 64° from CA and does not generate force drop on the mechanical response. Then a second pyramidal perfect dislocation nucleates from the top indenter region leading to the force drop observed at $\varepsilon = 10.7\%$ (Figure 5.13, label 2). One portion of the dislocation temporarily cross-slip in a basal slip plane (Figure 5.14b). The dislocations glide along the edge direction extending long screw segments. At $\varepsilon = 11.5\%$ (Figure 5.13, label 3), the second pyramidal dislocation entirely slips through the nanosphere. Two long screw segments are easily identifiable (Figure 5.14c). Finally, the

screw arms starts to dissociate locally within the basal plane. One can notice than both the triangular dislocation structure as well as the pseudo-structure induced by the stacking of pyramidal partial dislocations observed in the LT case (see Figure 5.6) are lacking when running higher temperature simulations with CA normal to the prism a plane.

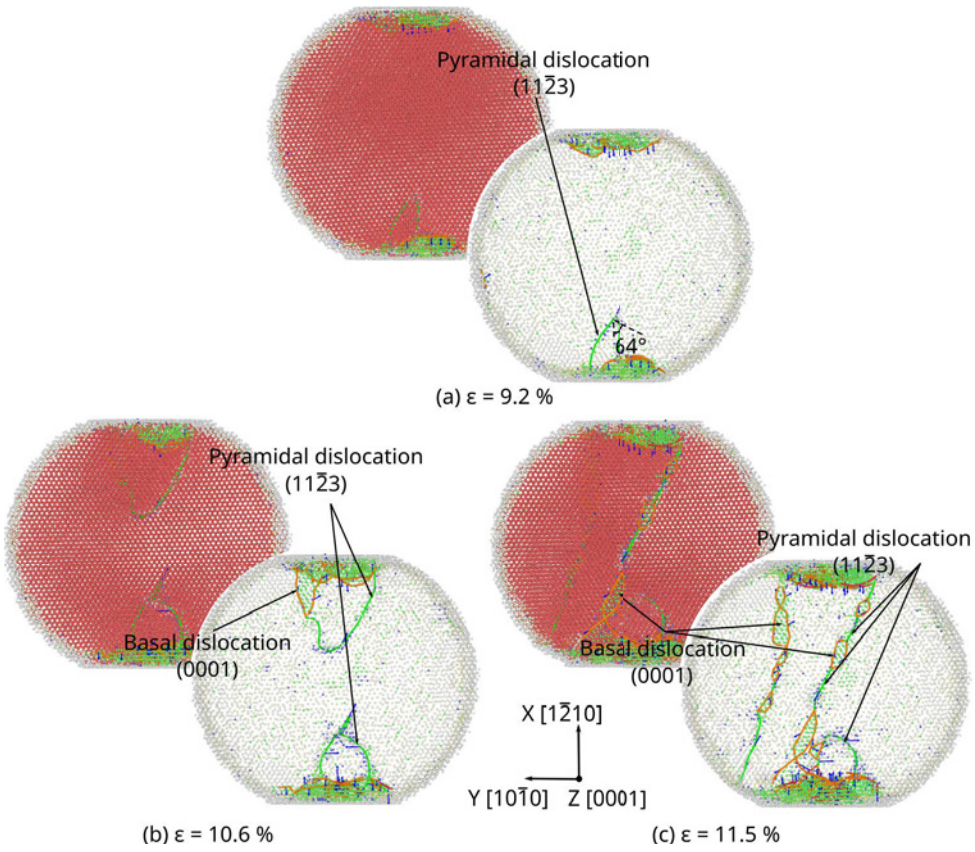

Figure 5.14: Compression of α-Al_2O_3 NPs for CA normal to a prism a plane at T=1000 K. Only O atoms (in red when HCP environment, light-grey for defective regions) are shown for a sake of clarity. Perfect dislocations are illustrated using OVITO (green curves). (a) ϵ=9.2%, first nucleation event characterized by the nucleation and propagation of a perfect dislocation within the pyramidal $(11\bar{2}3)$ slip plane. (b) ϵ=10.6%, subsequent nucleation events in the bottom region of the NP. (c) ϵ=11.5%, the first pyramidal dislocation reaches the opposite surface of NP. Two long screw dislocation arms remain in the NP.

5.3.3 Compression normal to the m plane $\{10\bar{1}0\}$

Mechanical response

Here we investigate nanocompressions with CA normal to a m plane at T=1000K. Figure 5.15 shows force vs. strain curve including an effective Young's modulus E^* about 157 GPa for Hertz fit boundaries of 2.0% and 11.0% strains, respectively. The end of the elastic regime is characterized by a yield point F_y=760 nN.

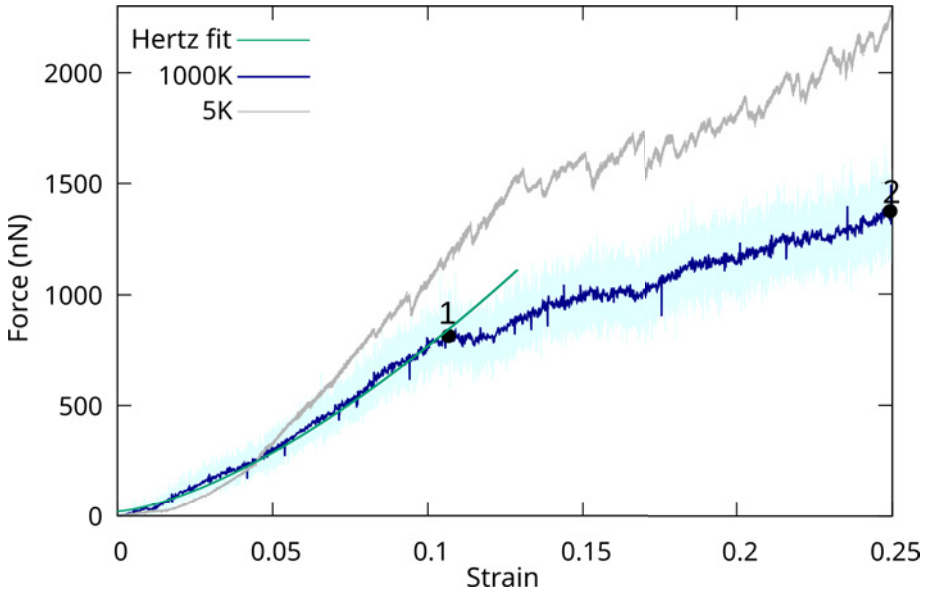

Figure 5.15: Force *vs.* strain response of a 15.1 nm diameter α-Al_2O_3 nanosphere under compression at T=1000 K with CA normal to the prism m plane. The light-blue curve refers to the raw data while the dark-blue one is a Bezier fit. Elastic Hertz fit is shown in green. Data computed at T=5K (grey curve) are shown for comparison.

Elementary deformation processes

The first plastic event occurs at $\varepsilon = 10.7\%$ (Figure 5.15, label 1) and a loading force F=820 nN. At this stage, several (0001) basal dislocations nucleate from the top indenter and the substrate contacting regions but in a less symmetric manner than in previously discussed cases, see Figure 5.16a. This asymmetry is attributed to a rotation of the sample during early contact with the indenter. As a consequence, the basal dislocations stack at side contacts and do not glide towards the center of the NP. Up to 25% strain (Figure 5.15, label 2), the slip activity does not satisfy the imposed strain-rate and the force continue to increase *i.e.,* only few plastic activity localized on the side contact regions between the NP and the indents is noticed during the whole nanocompression run (Figure 5.16b).

5.3.4 Compression normal to the R plane $\{10\bar{1}2\}$

The last simulation to be discussed concerns the nanocompression of 15.1 nm diameter α-alumina NP at T=1000 K with CA normal to an R plane. Figure 5.17 shows force *vs.* strain curves for the 15.1 nm size NP as compared to the LT test. The effective Young's modulus E^* is about 111 GPa for boundaries of the Hertz fit between 3.0 and 9.7% strains. F_y=722 nN characterizes the starting of the plastic regime.

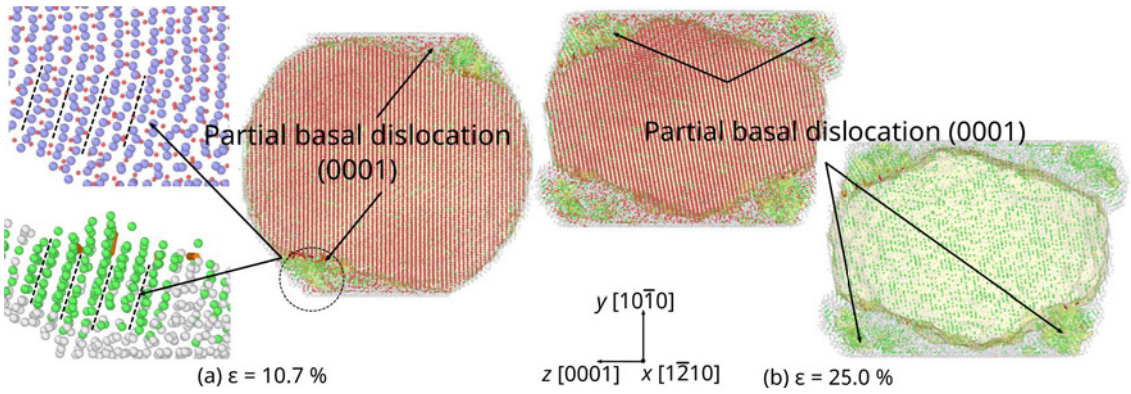

Figure 5.16: Compression of α-Al_2O_3 NPs for CA normal to the prism m plane at T=1000K. Only O atoms are shown for a sake of clarity. (a)ϵ=10.7%, partial dislocations in the basal slip system are identified as the main plastic deformation process (dislocation colored in orange, atoms in the stacking-fault colored in green). They nucleate at asymmetrically, from one side of each contact regions with the indenter and the substrate. (b) ϵ=25%, more dislocations accumulate on the side of the contact but no defect are identified in the central part of the NP.

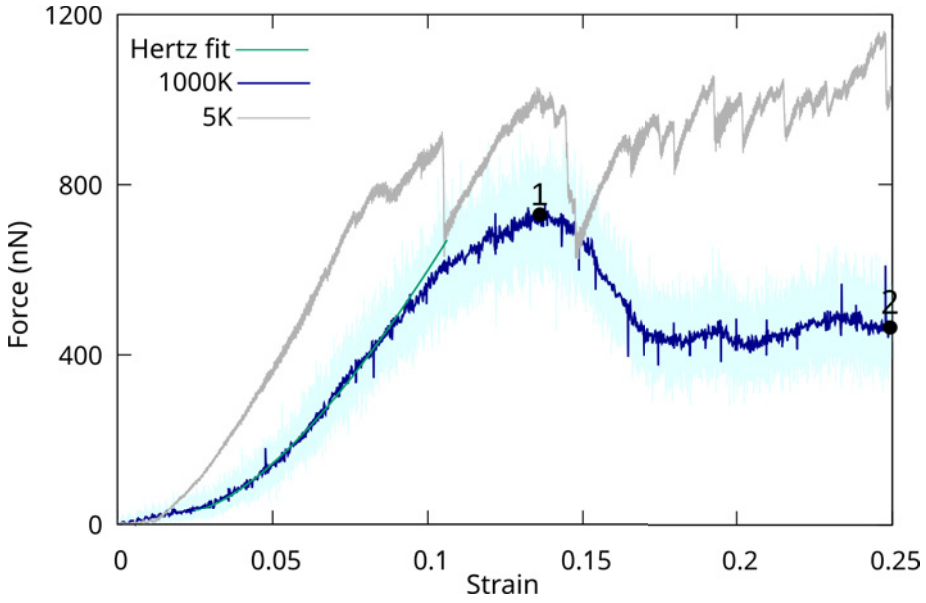

Figure 5.17: Force *vs.* strain response of a 15.1 nm diameter α-Al_2O_3 nanosphere under compression at T=1000 K with CA normal to a R plane. The light-blue curve refers to the raw data while the dark-blue one is a Bezier fit. Elastic Hertz fit is shown in green. Data computed at T=5K (grey curve) are shown for comparison.

Elementary deformation processes

The beginning of plasticity deformation is characterized by a significant force drop at ε = 13.7% (Figure 5.17, label 1). Several (0001) basal dislocations emit from the top

indenter and the substrate contacting regions, see Figure 5.18a. Between $\varepsilon = 13.7\%$ and $\varepsilon = 25.0\%$ (Figure 5.17, label 2), several partial dislocations in the basal slip systems are observable propagating from the centre of the NP to the lateral surfaces (Figure 5.18b). The shape of the NP changes and no crack is observed.

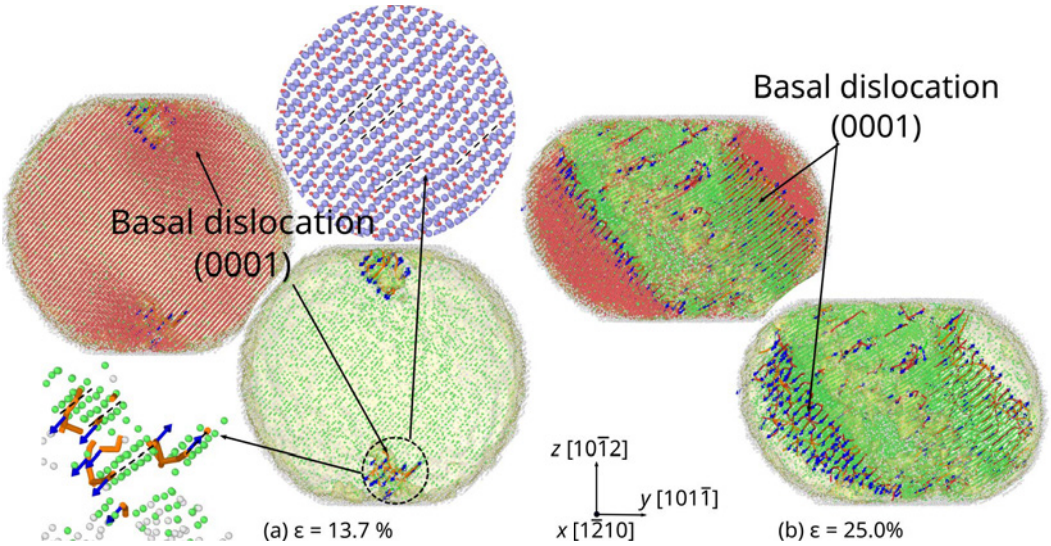

Figure 5.18: Compression of α-Al_2O_3 NPs for CA normal to the Rhombohedral R plane at T=1000K. Only O atoms are shown for a sake of clarity. (a)ϵ=13.7%, partial dislocations in the basal slip system are identified as the main plastic deformation process (dislocation colored in orange, atoms in the stacking-fault colored in green). They nucleate from contact regions with the indenter and the substrate. (b) ϵ=25%, more dislocations accumulate and gather in the central part of the NP.

For each CA, Table 5.2 resumes the effective Young's modulus $\langle E^* \rangle$, the yield force F_y of the largest NP and the plastic deformations mechanisms observed. The largest value of $\langle E^* \rangle$ is noticed for CA normal to the m plane that does not corresponds to the orientation of the largest F_y *i.e.,* CA normal to the c plane.

CA	$\langle E^* \rangle$ [GPa]	F_y [nN]	Plasticity process
c	127	1020	R twinning
a	154	849	Pyramidal slip (perfect)* + c slip
m	157	760	c slip (partials)
R	111	722	c slip (partials)

Table 5.2: Effective Young's modulus $\langle E^* \rangle$, yield force F_y (for largest size NPs 15.2 nm) and elementary plasticity processes as function of CA observed in α-Al_2O_3 NPs compressed at T=1000K. *: in this case, basal dislocations were also observed but only after screw dislocations (originally gliding in a pyramidal slip plane) remain in the sample (see Figure 5.14).

5.4 Discussion

In this section, we discuss the outcomes of the nanocompression simulations. In particular, the changes observed in the elementary deformation processes are discussed in the light of the current experimental and numerical literature.

5.4.1 Influence of orientation

Simulation results show that the slip system activity in α-Al_2O_3 strongly depends on the CA orientation and temperature with significant consequences on the yield strength. Table 5.1 and 5.2 show that the largest yield force F_y is obtained when CA normal to the c plane. This result is in good agreement with the study of Montagne *et al.* that performed *in situ* SEM tests on alumina micropillars at RT [MON 14]. For CA normal to c and m planes, Montagne and colleagues characterized R slip which is confirmed by our LT MD simulations for which (i) R twinning is observed for CA normal to the c plane and (ii) R slip in addition to c slip are shown for CA normal to the m plane. Both studies show pyramidal slip when CA normal to an a plane but in different slip planes *i.e.,* the s $\{1\bar{1}01\}$ for Montagne *et al.* while the n $\{2\bar{1}\bar{1}3\}$ in our case. Finally, Montagne *et al.* did not observed plasticity when compressing micropillars with CA axis-aligned with the R normal while MD simulations show c and pyramidal slip at LT. We believe that this could be attributed to a size-effects *i.e.,* nanoscale samples are less prone to cracking when compared to larger micropillars. Overall, this comparison again confirms the robustness of the Vashishta interatomic potentials to model the various deformation processes happening in α-alumina.

In the following, the slip activity observed in our simulations is discussed based on Schmid factor and SFE models. The Schmid factor M is commonly used to translate an applied compressive stress σ into a shear stress $\tau = M.\sigma$. M is defined as follow,

$$M = cos(\phi).cos(\lambda) \tag{5.5}$$

where ϕ and λ are the angles between the load direction and (i) the slip plane normal and (ii) the Burgers vector direction, as shown Figure 5.19.
As described by *e.g.*, Zhang *et al.* [ZHA 17] the normal $\vec{n}$ of slip plane using the 3-index notation is given by,

$$\vec{n} = \left[2h + k, h + 2k, \frac{3l}{2}\left(\frac{a_0}{c_0}\right)^2\right] \tag{5.6}$$

While shear or compression directions [h, k, m, l] can be described as,

$$\vec{s} = [h - m, k - m, l] \tag{5.7}$$

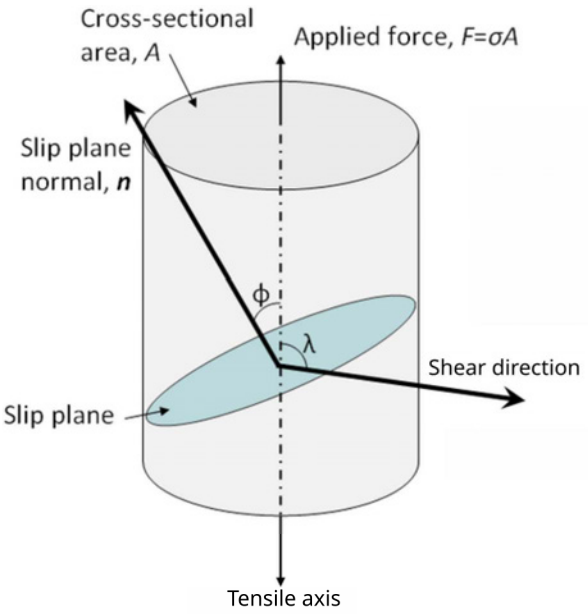

Figure 5.19: Schmid factor definition. Adapted from Bernard [ENN 16].

Assuming $[u_2\ v_2\ w_2]$ is the loading direction, $\cos(\phi)$ and $\cos(\lambda)$ can be expressed as,

$$\frac{\left[u_1u_2 + v_1v_2 - \frac{1}{2}(u_1v_2 + u_2v_1) + \left(\frac{c_0}{a_0}\right)^2 w_1w_2\right]}{\left[(u_1^2 + v_1^2 - u_1v_1 + \left(\frac{c_0}{a_0}\right)^2 w_1^2)\left(u_2^2 + v_2^2 - u_2v_2 + \left(\frac{c_0}{a_0}\right)^2 w_2^2\right)\right]^{\frac{1}{2}}} \tag{5.8}$$

where $[u_1\ v_1\ w_1]$ is the 3-index notation for $\overrightarrow{n}$ if $\cos(\phi)$ or $\overrightarrow{b}$ if $\cos(\lambda)$, respectively. In the following, we use literature (experiments and theoretical predictions) as well as γ-surface outcomes to define possible perfect and partial dislocation directions for each slip system (see Table 5.3).

Owing the large amount of available slip systems in HCP α-alumina (about 30 without considering partial dislocation slip systems), only slip systems of interest including those observed in our nanocompression simulations and referenced studies will be discussed in the following. Specific slip planes and Burgers vectors are resumed in Table 5.3. In addition, representative γ-lines as computed using the Vashishta interatomic potentials are recalled Figure 5.20.

Compression normal to the c plane (0001)

Slip plane		Burgers vector $\overrightarrow{b}$	$\overrightarrow{b_p}$
Basal c	(0001)	$\frac{1}{3}\langle 1\bar{2}10\rangle$	$\frac{1}{3}\langle 1\bar{1}00\rangle$
Prismatic a	$\{1\bar{2}10\}$	$\langle 10\bar{1}0\rangle$	$\frac{1}{3}\langle 10\bar{1}0\rangle$
Prismatic m	$\{10\bar{1}0\}$	$\frac{1}{3}\langle 1\bar{2}10\rangle$	
Rhombohedral R	$\{0\bar{1}12\}$	$\frac{1}{3}\langle 0\bar{1}11\rangle$	$\frac{1}{6}\langle\bar{2}021\rangle$
Pyramidal n	$\{11\bar{2}3\}$	$\frac{1}{3}\langle\bar{1}101\rangle$,$\langle 10\bar{1}0\rangle$	
Pyramidal s	$\{1\bar{1}01\}$	$\frac{1}{3}\langle 1\bar{1}01\rangle$, $\langle 01\bar{1}0\rangle$	

Table 5.3: Slip plane and possible Burgers vectors of α-Al_2O_3 used in our Schmid model. $\overrightarrow{b}$ relies to perfect Burgers vectors, $\overrightarrow{b_p}$ is for partial (leading or trailing) dislocations, respectively.

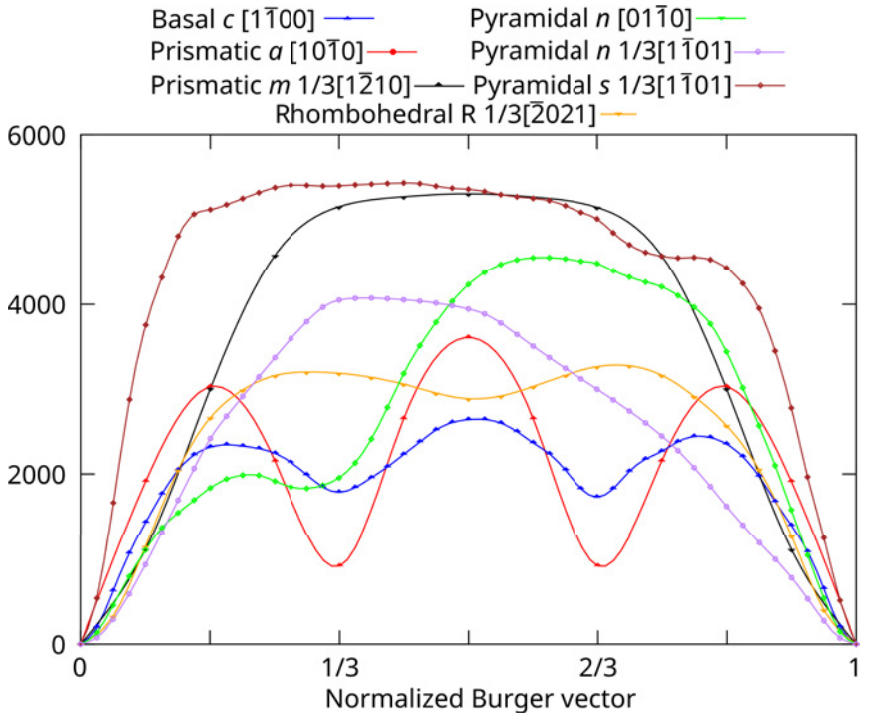

Figure 5.20: γ-lines for c, a, m, n, s and R slip planes computed using the Vashishta interatomic potentials. Respective translation directions are provided in the key.

Table 5.4 shows Schmid factors as computed using Equation 5.8 for R, n and s slip systems. In particular for this geometry, Schmid factors for c, m and a slip systems (partial and perfect) are null. Thus, this orientation is particularly suited for rhombohedral and pyramidal slip. Indeed, the rhombohedral slip planes $(01\bar{1}2)$ and $(1\bar{1}02)$ show a high Schmid factor for the perfect dislocation slip system M=0.45 and a slightly lower one for partial slip system M_p=0.33 (for both the leading and the trailing partial dislocation). Owing the high-energy barriers for full-Burgers vector translation in the R slip system (see Figure 5.20) and the length of respective Burgers vectors, partial slip or twinning

in the R plane might be favoured at elevated stress for this specific orientation. Based on the γ-surface analysis (see Chapter 3, Figure 3.18), pyramidal n slip systems rely on perfect $\frac{1}{3}\langle\bar{1}101\rangle$ and $\langle 01\bar{1}0\rangle$ perfect (or partial) Burgers vectors (dissociation in n slip system has however never been discussed in the literature). While Schmid factor is null in the latter for CA along the c axis, the γ-line for $\langle\bar{1}101\rangle$ shows single-hump profile with elevated energy. Same high-energy barrier is noticed of the s slip systems including lower Schmid factor values (M=0.25). These analysis justify the elementary deformation processes observed in our nanocompression simulations along c *i.e.,* R twinning, as well as the outcomes of Sarobol *et al.* [SAR 16] MD compression simulations. However, one can note that only R perfect dislocations (no twin) were characterized by Montagne *et al.* in *in situ* SEM micropillar experiments but this can be justified by the lower stress reached in the experiment induced by larger-sized pillars (size-effect). Finally, the occurrence of R twins for CA along [0001] is also in agreement with compression experiments performed in bulk α-Al_2O_3 at 800°C by Lagerlof *et al.* [LAG 94].

Slip plane		Schmid factor	
		M	M_p
Rhombohdral R	$(01\bar{1}2)$	0.45	0.33, 0.33
	$(\bar{1}012)$	0.45	0.33, 0.33
	$(1\bar{1}02)$	0.45	0.33, 0.33
Pyramidal n	$(2\bar{1}\bar{1}3)$	0.40, 0.00	
	$(11\bar{2}3)$	0.40, 0.00	
Pyramidal s	$(1\bar{1}01)$	0.25	

Table 5.4: Schmid factors in R, n and s slip systems for CA normal to the c plane.

Compression normal to the a plane $\{1\bar{2}10\}$

Schmid factors for the various c and a slip systems (including partial slip systems) as well as those relying on the $(10\bar{1}2)$ R plane are null when compressing perpendicularly to the a plane. Nevertheless, several slip systems remain available including m, R and presumably pyramidal n slip systems. The case of partial R dislocations (or twinning) is quite tedious for this orientation as only one of the two partial slip systems has a non-zero Schmid factors within the $(01\bar{1}2)$ and $(1\bar{1}02)$ slip planes what might not favour R partial slip or twinning. On the other hand, prism m has high Schmid factor (M=0.43) but a very unlikely energy profile as shown Figure 5.20. Nanocompression simulations along a direction show dislocation nucleation in symmetric pyramidal n planes $(11\bar{2}3)$ and $(2\bar{1}\bar{1}3)$ that further dissociate (see Figure 5.6). This agrees with moderate Schmid values and sSFE profiles computed for the two representative Burgers vectors in the n slip system. While the competition between pyramidal n and rhombohedra R slip is ovious in this

case, the absence of a slip is surprising as the sSFE for the a slip is supposed to be quite low. Here, we assume that this absence is justified by the length of the a slip Burgers vector which is larger than 8 Å when compared to the shorter one in R and pyramidal n slip systems [SNO 73]. Finally, these observations are in good agreement with Kim *et al.* MD nanoindentation simulation normal to the a plane that shows n slip systems activated [KIM 18]. However, It is worthy to point out that while pyramidal slip was also characterized in Montagne *et al.* micropillar experiments for this orientation, only pyramidal s that shows unfavorable energy profile in Figure 5.20 was concerned and not pyramidal n.

Slip plane		Schmid factor M	M_p
Prismatic a	$(\bar{2}110)$	0.43	
	$(11\bar{2}0)$	0.43	
Prismatic m	$(01\bar{1}0)$	0.43	
	$(\bar{1}100)$	0.43	
Rhombohdral R	$(01\bar{1}2)$	0.34	0.00, 0.50
	$(1\bar{1}02)$	0.34	0.00, 0.50
Pyramidal n	$(2\bar{1}\bar{1}3)$	0.20, 0.38	
	$(11\bar{2}3)$	0.20, 0.38	

Table 5.5: Schmid factors in a, m, R and n slip systems for CA normal to the a plane.

Compression normal to the m plane $\{10\bar{1}0\}$

Slip plane		Schmid factor M	M_p
Prismatic a	$(\bar{2}110)$	0.43	
	$(11\bar{2}0)$	0.43	
Prismatic m	$(01\bar{1}0)$	0.43	
	$(\bar{1}100)$	0.43	
Rhombohdral R	$(10\bar{1}2)$	0.45	0.33, 0.33
Pyramidal n	$(2\bar{1}\bar{1}3)$	0.20, 0.38	
	$(11\bar{2}3)$	0.20, 0.38	

Table 5.6: Schmid factors in a, m, R and n slip systems for CA normal to the m plane.

Table 5.6 shows Schmid factors for the various slip systems with CA along the $[10\bar{1}0]$ direction. Perfect $[0\bar{1}10](\bar{2}110)$ and $[\bar{1}100](11\bar{2}0)$ prism a as well as the $[10\bar{1}1](10\bar{1}2)$ R slip systems exhibit particularly high Schmid factors with M=0.43, 0.43 and 0.38, respectively. Other R slip systems exhibit lower values while the remaining m slip system has a null Schmid factor for the tested CA. Two configurations are noticed for partial R

slip systems including (i) M_p=0.33 and 0.17 alternatively, respectively for leading and/or trailing partial dislocations and (ii) M_p=0.43 and 0.33 for the leading and trailing partial dislocations, respectively. Only dissociation in the $(10\bar{1}2)$ slip plane leads to the second configuration. In the LT simulation, we observe partial dislocations in the R slip system in agreement with the Schmid hypothesis in addition to basal slip which is associated to a rotation of the NP in the initial stage of the compression. Kim *et al.* also observed R slip for this orientation in MD simulation [KIM 18] as well as Montagne *et al.* in their alumina micropillar compression test. Finally, the occurrence of R partial dislocation and twins is also in agreement with observations performed in bulk when compressed along $[10\bar{1}0]$ [LAG 94, HE 02].

Compression normal to the R plane $\{10\bar{1}2\}$

Slip plane		Schmid factor	
		M	M_p
basal c	(0001)	0.25	0.28, 0.14
Rhombohdral R	$(01\bar{1}2)$	0.46	0.23, 0.45
	$(1\bar{1}02)$	0.46	0.23, 0.45
Pyramidal n	$(2\bar{1}\bar{1}3)$	0.50, 0.10	
	$(11\bar{2}3)$	0.50, 0.03	

Table 5.7: Schmid factors in c, R and n slip systems for CA normal to the R plane.

Table 5.7 shows Schmid factors for the various slip systems with CA normal to a $\{10\bar{1}2\}$ plane. The R case is the one leading to the more widespread Schmid factor distribution including possible slip in various perfect and partial slip systems. Indeed, c (perfect and partial), R (perfect and partial) and pyramidal n slip systems might be activated while all m and a slip systems show nearly zero Schmid factor (M<0.1). More precisely, the two $[11\bar{2}0](0001)$ and $[\bar{2}110](0001)$ perfect c slip systems have M=0.25 (the last one being null), while respective partial slip systems show M_p=0.28 and 0.14 (or 0.14 and 0.28), the third dissociated slip systems is characterized by lower Schmid values (M_p=0.14 for both leading and trailing partial dislocations) while its perfect counterpart has a null Schmid factor. Assuming the low-energy of the basal GSF profile, basal slip might be favoured in this case. However, R and n slip systems also show high-Schmid factors. Two over three R planes are characterized by M=0.46 and M_p=0.23, 0.45 while the last one is characterized by M=0.24 and M_p=0.18 for both partial dislocations. Finally, both pyramidal n slip systems are characterized by M=0.50 and M_p=0.10, 0.03 respectively for Burgers vector along $\langle\bar{1}101\rangle$ and $\langle10\bar{1}0\rangle$ directions, respectively.
Again, the Schmid and GSFE analyses explain the observations made out of the simulation. Indeed, c slip is observed whatever the temperature due to its particularly low GSFE

while pyramidal n is also observed (especially at LT), probably due to a particularly high Schmid factor. Same slip systems were observed in Kim *et al.* MD nanoindentation simulations [KIM 18]. However, it can be noticed that only cracks (no slips) were characterized by Montagne *et al.* in *in situ* SEM compression micropillar [MON 14] and Roberts *et al* [ROB 93] tensile experiments. This is again certainly related to the size of the samples tested by Montagne *et al.* and to the type of loading for Roberts *et al.*

5.4.2 On the effect of temperature

Temperature influences the mechanical behaviour and activated slip systems in α-Al_2O_3 NPs. Force *vs.* displacement curves computed at HT show more noise due to the increase of atomic vibrations and their consequences on the indenter force calculation. They are also soften in both the elastic and plastic regimes (see Figure 5.11). Tables 5.1 and 5.2 show that both the yield force F_y and effective Young's modulus drop down when increasing T. This behaviour is in good agreement with what is known from bulk alumina (Figure 5.21). Maximum $\langle E^* \rangle$ is noticed for the $[10\bar{1}2]$ orientation at 5K while it is $[10\bar{1}0]$ at 1000K, in addition to other relative variations of E^* it presumes a anisotropic effect of the temperature on the elastic properties. A similar trend applies for F_y for which relative variations with temperature are strongly related to orientation. In the plastic regime, load drops are also slightly softer as marked by lower-amplitude force variations that are attributed to more spread nucleation events assisted by temperature.

CA	5K	1000K
c	R twinning	R twinning
a	Pyramidal n slip (perfects + partials)	Pyramidal n slip (perfect)* + c slip
m	c and R slip (partials)	c slip (partials)
R	c and pyramidal slip (partials)	c slip (partials)

Table 5.8: The elementary plasticity processes as function of CA is observed in α-Al_2O_3 NPs compression tests at T=5 and 1000K.

Temperature also influences the elementary deformation processes. In general, decreasing the temperature leads to higher yield strength. In FCC metals, it is known that such stress increases at LT enhance dislocation dissociation and twinning [ELD 99, OGA 05]. A similar trend is observed in our simulations. Indeed, nanocompression normal to the $\{1\bar{2}10\}$ plane show partial dislocations in a pyramidal slip plane at 5K while only perfect one in the same slip plane are noticed at 1000 K. Furthermore, c and R slip are observed for CA normal to $(10\bar{1}0)$ plane as well as basal c and pyramidal slip for CA normal to $(10\bar{1}2)$ at 5K while only c slip is shown at 1000K for both orientations, see Table 5.8. This effect of temperature on the plastic deformation of alumina is very similar to what

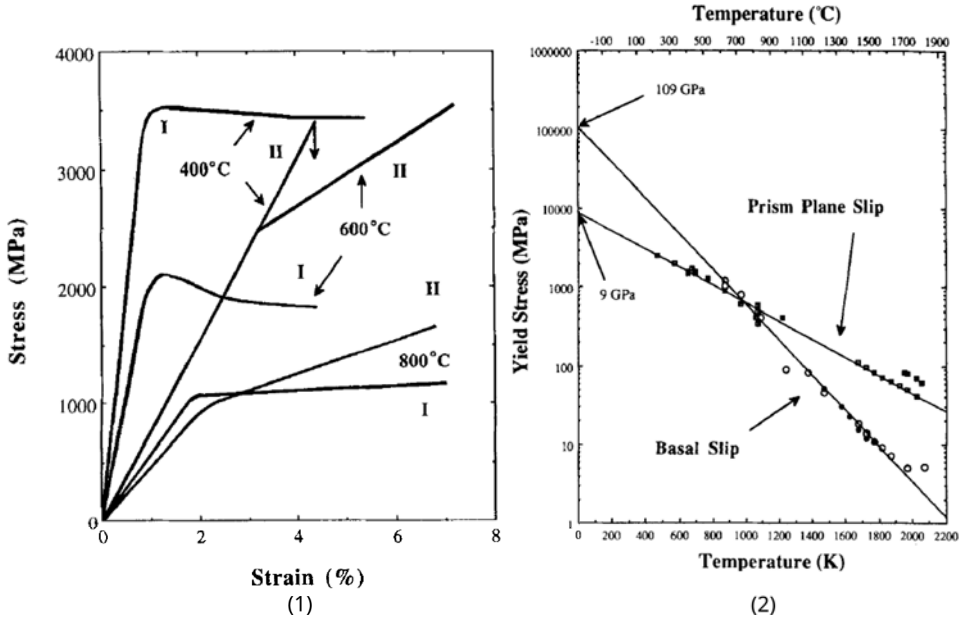

Figure 5.21: Mechanical behaviour of bulk alumina as function of temperature. (a) stress strain curves, (b) yield stress *vs.* temperature for basal and prism a slip. Adapted from ref [LAG 94].

is know in the case of bulk alumina [CAS 81a, LAG 94, HEU 98, CAS 04]. This is illustrated Figure 5.21b where we observe the effect of T on the critical resolve shear stress that becomes more favourable to basal slip at HT in a similar way that what is observed in our simulations.

Overall, MD nanocompression simulations performed using the Vashishta interatomic potentials allow to provide a detailed description of the influence of orientation and temperature on the mechanical properties and elementary deformation processes that control the plastic deformation of α-alumina at small-scale. These simulations when applied to α-Al_2O_3 NPs are particularly coherent with micro and bulk experiments and will provide solid foundations to interpret future nanomechanical experiments as those performed *in situ* inside the TEM or in the SEM.

Chapter V summary:

This chapter focuses on modeling the mechanical behaviour of α-Al_2O_3 NPs under compression as function of orientation and temperature. Simulations are performed using the interatomic potential that was shown to be the more transferable to nanomechanics *i.e.*, the Vashishta potential. Four directions were investigated with CA normal to c, m, a and R planes. The mechanical response as well as the main deformation processes were investigated at 5 and 1000 K temperature and a particular influence of the orientation was noticed especially on c, R and pyramidal n slip. Twinning was also observed in the R slip mode. While the temperature softens the material in an isotropic manner, the c slip is favoured at HT as in the bulk. All results were discussed in the lights of recent micropillar experiments and original deformation tests performed in bulk conditions with a fair agreement.

Conclusion and Perspectives

In this PhD thesis we have investigated α-Al_2O_3 properties at small-scale using atomistic simulations. The study was mainly divided into two parts: 1) compute relevant material properties of bulk α-Al_2O_3 and test the transferability of various force fields to nanomechanics and 2) modeling the compression of α-Al_2O_3 NPs including a detailed analysis of the plastic deformation processes as function of orientation and temperature.

Which potential formalism to use to model α-Al_2O_3 nanomechanics?

Three types of interatomic potentials were investigated including the RI formalism [BUS 94, GAL 92, LEW 85, MAT 94, SUN 06], the 2/3-body interaction potentials [BLO 96, VAS 08] and the variable charge SMTB-Q potential [SAL 16].
Lattice properties and elastic constants were tested and compared to DFT and experimental rests. 2/3-body Vashishta, the SMTB-Q as well as the RI Gale potentials have shown a particularly fair agreement with the literature. The calculation of the basal surface energy was less precise for the RI potential. In this case, the ability of the Vashishta potential to reproduce the complex Al-double layer surface reconstruction in a similar manner than the variable charge SMTB-Q potential reinforced the transferability of the potential to surface properties albeit its simple formulation. In the future, additional surfaces might be computed to reinforce the choice of one or the other potential. As a critical ingredient required to describe dislocation plasticity, stacking fault energy were also computed in various planes of the α-alumina structure *i.e.*, the basal, prism a and m, the rhombohedral slip system R as well as the various pyramidal slip systems. Once again, Vashishita and SMTBQ potentials have shown particularly close results reinforcing the transferability of the first one to dislocation properties. Finally, both Al/O-terminated and Al/Al-terminated basal dislocations were modeled using the Vashishta and the variable charge SMTB-Q potentials and we have investigated topological configurations and relative energy trends. Results confirmed the ability of the Vashishta potential to capture most of the main ingredients of the basal edge dislocation when compared to more sophisticated and CPU 'costly' variable charge potentials. As for surfaces, additional studies dedicated to the various types of dislocations in alumina might be helpful to better understand small-scale properties of this material.

By computing several material properties related to lattice, surface and dislocations using various interatomic potentials we verified that the Vashishta potential was the most suitable in terms of precision *vs.* cpu costs for applications in the field of nanomechanics. In the future, additional interatomic potentials might be investigated including *e.g.,* the Streitz potential [STR 94].

Mechanical properties and elementary deformation processes of α-Al_2O_3 nanoparticles

After fabrication of α-Al_2O_3 neutral particles, we use MD to model nanocompression tests and investigate the deformation of alumina nanospheres as function of orientations and temperatures. Four directions were investigated with compression axis normal to c, m, a and R planes. The mechanical response is characterized by elastic and plastic behaviours without failure during loading. The transition point from elastic to inelastic response is marked by the yield force F_y. The highest yield strength was noticed for CA normal to the c plane. At HT, both yield forces F_y and effective Young's modulus drop down whatever CA. The main deformation processes were investigated and a particular influence of the orientation was noticed including various dislocation and twinning processes when changing CA. At LT, c, R and pyramidal n slips were particularly observed, as well R twinning. Preliminary tests performed at higher temperature were also performed showing more favourable c slip and an anisotropic influence of the temeprature on the elastic response of the NPs. All the results were discussed in the lights of recent micropillar experiments and original deformation tests performed in bulk conditions with a particularly fair agreement. Those simulations could be used to better interpret TEM or SEM compression experiments applied to NPs as they provide direct evidences of slip activity as function of orientations and temperatures.

Perspectives

The outcomes of this PhD shed new lights on alumina ceramic NPs deformation processes and plasticity that are important to better understand compaction processes of ceramic powders. These might open in the future new routes to shape ceramics at low or moderate temperature to increase their density before sintering, while preserving nanoscale grains. Still, several ideas deserve attention.

— Concerning the mechanical response of α-alumina NPs, several other directions might be used to provide (i) a better description of NPs response for *e.g.*, upscaling modeling applications and (ii) investigate less-known slip systems: for example, a slip was not observed in our entire MD study whereas it is known to exist in the experiments [LAG 94]. Same conclusion allows for basal twinning.

— Additional studies on dislocations (core structure, critical resolved shear stresses, mobility) are required to get a better understanding of small-scale plasticity processes in alumina.
— For some orientations, structural changes were noticed when related to pyramidal slip. Those might be further investigated in the future as connected to possible phase transformations.
— The study of phase transformation of nanometersized transition alumina NPs under pressure (see *e.g.*, [ISS 18]) using MD is crucial to better asses compaction and sintering modeling of alumina. Indeed, alumina powders are generally made out of 2 or 3 alumina polymorphses that are not enough investigated from a modeling point of view. For this purpose, the transferability of two additional interatomic potentials *i.e.*, the Alvarez [ALV 94, ALV 95, LAU 20] and the Streitz [STR 94] interatomic potentials that are already known for their ability to model alumina polymorphs with correct relative energies would have to be tested.
— Once modeled, these new phases will have to be investigated in terms of mechanical properties and plastic deformation processes.
— The thermal sintering process itself when applied to alumina nanopowder could then be modeled using either MD and the methodology proposed in Refs. [ZHU 96, LAN 16, YAN 18] or multi-scale approaches as the discrete-element method that could integrate yield forces F_y computed in this thesis as inputs.

References

[ABU 19] Abuin M., Kim Y. Y., Runge H., Kulkarni S., Maier S., Dzhigaev D., Lazarev S., Gelisio L., Seitz c., Richard M.-I. et al.
Coherent X-ray imaging of CO-adsorption-induced structural changes in Pt nanoparticles: implications for catalysis. *ACS Applied Nano Materials*, vol. 2, n° 8, 2019, p. 4818–4824, ACS Publications.

[ACK 06] Ackland G., Jones A.
Applications of local crystal structure measures in experiment and simulation. *Physical Review B*, vol. 73, n° 5, 2006, Page 054104, APS.

[AGE 09] Agena A. S.
A study of flow characteristics of nanostructured Al_{6082} alloy produced by ECAP under upsetting test. *Journal of Materials Processing Technology*, vol. 209, n° 2, 2009, p. 856–863, Elsevier.

[ALS 14] Al-Sanabani F. A., Madfa A. A., Al-Qudaimi N. H.
Alumina ceramic for dental applications: a review article. *American Journal of Materials Research*, vol. 1, n° 1, 2014, p. 26–34.

[ALV 94] Alvarez L. J., Leon L. E., Sanz J. F., Capitán M. J., Odriozola J. A.
Surface structure of cubic aluminum oxide. *Physical Review B*, vol. 50, n° 4, 1994, Page 2561, APS.

[ALV 95] Alvarez L. J., Leon L. E., Sanz J. F., Capitan M. J., Odriozola J. A.
Computer simulation of.γ-Al_2O_3 microcrystal. *The Journal of Physical Chemistry*, vol. 99, n° 51, 1995, p. 17872–17876, ACS Publications.

[AMO 17] Amodeo J., Lizoul K.
Mechanical properties and dislocation nucleation in nanocrystals with blunt edges. *Materials and Design*, vol. 135, 2017, p. 223–231, Elsevier.

[AMO 18] Amodeo J., Merkel S., Tromas C., Carrez P., Korte-Kerzel S., Cordier P., Chevalier J.
Dislocations and plastic deformation in MgO crystals: a review. *Crystals*, vol. 8, n° 6, 2018, Page 240, Multidisciplinary Digital Publishing Institute.

[AMO 21] Amodeo J., Pizzagalli L.
Modeling the mechanical properties of nanoparticles: a review. *Comptes Rendus. Physique*, vol. 22, n° S3, 2021, p. 1–32.

[AND 80] Andersen H. C.
Molecular dynamics simulations at constant pressure and/or temperature. *The Journal of Chemical Physics*, vol. 72, n° 4, 1980, p. 2384–2393, American Institute of Physics.

[ARE 19] Arena A., Prete F., Rambaldi E., Bignozzi M. c., Monaco C., Di Fiore A., Chevalier J.
Nanostructured zirconia-based ceramics and composites in dentistry: A state-of-the-art review. *Nanomaterials*, vol. 9, n° 10, 2019, Page 1393, Multidisciplinary Digital Publishing Institute.

[BEA 11] Beaber A., Nowak J., Ugurlu O., Mook W., Girshick S., Ballarini R., Gerberich W.
Smaller is tougher. *Philosophical Magazine*, vol. 91, n° 7-9, 2011, p. 1179–1189, Taylor & Francis.

[BEL 17] Belkin A., Bezryadin A., Hendren L., Hubler A.
Recovery of alumina nanocapacitors after high voltage breakdown. *Scientific Reports*, vol. 7, n° 1, 2017, p. 1–7, Nature Publishing Group.

[BER 63] Bernstein B.
Elastic constants of synthetic sapphire at 27°C. *Journal of Applied Physics*, vol. 34, n° 1, 1963, p. 169–172, American Institute of Physics.

[BER 84] Berendsen H. J., Postma J. v., van Gunsteren W. F., DiNola A., Haak J. R.
Molecular dynamics with coupling to an external bath. *The Journal of Chemical Physics*, vol. 81, n° 8, 1984, p. 3684–3690, American Institute of Physics.

[BIA 13] Bian J.-J., Wang G.-F.
Atomistic deformation mechanisms in copper nanoparticles. *Journal of Computational and Theoretical Nanoscience*, vol. 10, n° 9, 2013, p. 2299–2303, American Scientific Publishers.

[BIL 96] Bilde-Sørensen J., Lawlor B., Geipel T., Pirouz P., Heuer A., Lagerlöf K. et al.
On basal slip and basal twinning in sapphire (α-Al_2O_3)—I. Basal slip revisited. *Acta Materialia*, vol. 44, n° 5, 1996, p. 2145–2152, Elsevier.

[BIS 85] Biswas R., Hamann D.
Classical Two and Three-Body Interatomic Potentials for Silicon Simulations. *MRS Online Proceedings Library Archive*, vol. 63, 1985, Cambridge University Press.

[BIS 12] Biswas A., Park H., Sigmund W. M.
Flexible ceramic nanofibermat electrospun from TiO_2–SiO_2 aqueous sol. *Ceramics International*, vol. 38, n° 1, 2012, p. 883–886, Elsevier.

[BIT 06] Bitzek E., Koskinen P., Gähler F., Moseler M., Gumbsch P.
Structural relaxation made simple. *Physical Review Letters*, vol. 97, n° 17, 2006, Page 170201, APS.

[BLO 96] Blonski S., Garofalini S. H.
Molecular dynamics study of silica-alumina interfaces. *The Journal of Physical Chemistry*, vol. 100, n° 6, 1996, p. 2201–2205, ACS Publications.

[BOC 10] Bocanegra-Bernal M., Matovic B.
Mechanical properties of silicon nitride-based ceramics and its use in structural applications at high temperatures. *Materials Science and Engineering: A*, vol. 527, n° 6, 2010, p. 1314–1338, Elsevier.

[BOD 05] Bodur C., chang J., Argon A.
Molecular dynamics simulations of basal and pyramidal system edge dislocations in sapphire. *Journal of the European ceramic Society*, vol. 25, n° 8, 2005, p. 1431–1439, Elsevier.

[BOU 77] Boutin P.
L'arthroplastie totale de la hanche par prothèse en alumine. *International Orthopaedics*, vol. 1, n° 2, 1977, p. 87–94, Springer.

[BOU 88] Boutin P., Christel P., Dorlot J.-M., Meunier A., De Roquancourt A., Blanquaert D., Herman S., Sedel L., Witvoet J.
The use of dense alumina–alumina ceramic combination in total hip replacement. *Journal of Biomedical Materials Research*, vol. 22, n° 12, 1988, p. 1203–1232, Wiley Online Library.

[BRA 09] Branicio P. S., Rino J. P., Gan C. K., Tsuzuki H.
Interaction potential for indium phosphide: a molecular dynamics and first-principles study of the elastic constants, generalized stacking fault and surface energies. *Journal of Physics: Condensed Matter*, vol. 21, n° 9, 2009, Page 095002, IOP Publishing.

[BUC 38] Buckingham R. A.
The classical equation of state of gaseous helium, neon and argon. *Proceedings of the Royal Society of London. Series A. Mathematical and Physical Sciences*, vol. 168, n° 933, 1938, p. 264–283, The Royal Society London.

[BUS 94] Bush T., Gale J., Catlow C., Battle P.
Self-consitent interatomic potentials for the simulation of binary and ternary oxides. *Journal of Materials Chemistry*, vol. 4, n° 11, 1994.

[BYE 10] Byer C. M., Li B., Cao B., Ramesh K.
Microcompression of single-crystal magnesium. *Scripta Materialia*, vol. 62, n° 8, 2010, p. 536–539, Elsevier.

[CAL 12] Calvié E., Joly-Pottuz L., Esnouf C., Clément P., Garnier V., Chevalier J., Jorand Y., Malchère A., Epicier T., Masenelli-Varlot K.

Real time TEM observation of alumina ceramic nano-particles during compression. *Journal of the European Ceramic Society*, vol. 32, n° 10, 2012, p. 2067–2071, Elsevier.

[CAL 14] Calvié E., Réthoré J., Joly-Pottuz L., Meille S., Chevalier J., Garnier V., Jorand Y., Esnouf C., Epicier T., Quirk J. et al.
Mechanical behavior law of ceramic nanoparticles from transmission electron microscopy in situ nano-compression tests. *Materials Letters*, vol. 119, 2014, p. 107–110, Elsevier.

[CAR 21] Carnis J., Gao L., Fernández S., Chahine G., Schülli T. U., Labat S., Hensen E. J., Thomas O., Hofmann J. P., Richard M.-I.
Facet-dependent strain determination in electrochemically synthetized platinum model catalytic nanoparticles. *Small*, vol. 17, n° 18, 2021, Page 2007702, Wiley Online Library.

[CAS 81a] Castaing J., Cadoz J., Kirby S.
Deformation of Al_2O_3 single crystals between 25°C and 1800°C: basal and prismatic slip. *Le Journal de Physique Colloques*, vol. 42, n° C3, 1981, p. C3–43, EDP Sciences.

[CAS 81b] Castaing J., Veyssiere P., Kubin L., Rabier J.
The plastic deformation of silicon between 300°C and 600°C. *Philosophical Magazine A*, vol. 44, n° 6, 1981, p. 1407–1413, Taylor & Francis.

[CAS 97] Castaing J., Munoz A., Garcia D. G., Rodriguez A. D.
Basal slip in sapphire (α-Al_2O_3). *Materials Science and Engineering: A*, vol. 233, n° 1-2, 1997, p. 121–125, Elsevier.

[CAS 04] Castaing J., He A., Lagerlöf K., Heuer A.
Deformation of sapphire (α-Al_2O_3) by basal slip and basal twinning below 700°C. *Philosophical Magazine*, vol. 84, n° 11, 2004, p. 1113–1125, Taylor & Francis.

[CAT 77] Catlow C. R. A.
Point defect and electronic properties of uranium dioxide. *Proceedings of the Royal Society of London. A. Mathematical and Physical Sciences*, vol. 353, n° 1675, 1977, p. 533–561, The Royal Society London.

[CHE 03] Chen M., Ma E., Hemker K. J., Sheng H., Wang Y., Cheng X.
Deformation twinning in nanocrystalline aluminum. *Science*, vol. 300, n° 5623, 2003, p. 1275–1277, American Association for the Advancement of Science.

[CHE 06] Chevalier J.
What future for zirconia as a biomaterial? *Biomaterials*, vol. 27, n° 4, 2006, p. 535–543, Elsevier.

[CHE 07] Chevalier J., Gremillard L., Deville S.
Low-temperature degradation of zirconia and implications for biomedical implants. *Annual Review of Materials Research*, vol. 37, 2007, p. 1–32, Annual Reviews.

[CHE 09] Chevalier J., Gremillard L.
Ceramics for medical applications: A picture for the next 20 years. *Journal of the European Ceramic Society*, vol. 29, n° 7, 2009, p. 1245–1255, Elsevier.

[CHE 15] Cheng G., Miao c., Qin Q., Li J., Xu F., Haftbaradaran H., Dickey E. C., Gao H., Zhu Y.
Large anelasticity and associated energy dissipation in single-crystalline nanowires. *Nature NanoTechnology*, vol. 10, n° 8, 2015, p. 687–691, Nature Publishing Group.

[CHE 17] Cheng J., Wu J., Gong Y., Wen X., Wen Q.
Grinding forces in micro slot-grinding (MSG) of single crystal sapphire. *International Journal of Machine Tools and Manufacture*, vol. 112, 2017, p. 7–20, Elsevier.

[CHO 89] Chokshi A., Rosen A., Karch J., Gleiter H.
On the validity of the Hall-Petch relationship in nanocrystalline materials. *Scripta Metallurgica*, vol. 23, n° 10, 1989, p. 1679–1683, Elsevier.

[CHO 06] Chou C.-C., Chen C.-S., Lin I.-N., Yang W.-c., Cheng H.-F.
Development of X_7R type base-metal-electroded $BaTiO_3$ capacitor materials by co-doping of MgO/Y_2O_3 additives. *Ferroelectrics*, vol. 332, n° 1, 2006, p. 35–39, Taylor & Francis.

[CHO 15] Choudhary K., Liang T., Chernatynskiy A., Phillpot S. R., Sinnott S. B.
Charge optimized many-body (COMB) potential for Al_2O_3 materials, interfaces, and nanostructures. *Journal of Physics: Condensed Matter*, vol. 27, n° 30, 2015, Page 305004, IOP Publishing.

[CHR 08] Chraska T., Neufuss K., Dubsky J., Ctibor P., Klementova M.
Fabrication of bulk nanocrystalline ceramic materials. *Journal of Thermal Spray Technology*, vol. 17, n° 5-6, 2008, Page 872, Springer.

[CLO 09] Clouet E., Ventelon L., Willaime F.
Dislocation core energies and core fields from first principles. *Physical Review Letters*, vol. 102, n° 5, 2009, Page 055502, APS.

[DAL 07] Dalla Pria P.
Evolution and new application of the alumina ceramics in joint replacement. *European Journal of Orthopaedic Surgery Traumatology*, vol. 17, n° 3, 2007, p. 253–256, Springer.

[DAL 12] Dalal A., Pawar V., McAllister K., Weaver C., Hallab N. J.
Orthopedic implant cobalt-alloy particles produce greater toxicity and inflammatory cytokines than titanium alloy and zirconium alloy-based particles in vitro, in human osteoblasts, fibroblasts, and macrophages. *Journal of Biomedical Materials Research Part A*, vol. 100, n° 8, 2012, p. 2147–2158, Wiley Online Library.

[DAW 84] Daw M. S., Baskes M. I.
Embedded-atom method: Derivation and application to impurities, surfaces, and other defects in metals. *Physical Review B*, vol. 29, n° 12, 1984, Page 6443, APS.

[DEA 02] De Aza A., Chevalier J., Fantozzi G., Schehl M., Torrecillas R.
Crack growth resistance of alumina, zirconia and zirconia toughened alumina ceramics for joint prostheses. *Biomaterials*, vol. 23, n° 3, 2002, p. 937–945, Elsevier.

[DEN 10] Denry I., Holloway J. A.
Ceramics for dental applications: a review. *Materials*, vol. 3, n° 1, 2010, p. 351–368, Molecular Diversity Preservation International.

[DIC 58] Dick Jr B., Overhauser A.
Theory of the dielectric constants of alkali halide crystals. *Physical Review*, vol. 112, n° 1, 1958, Page 90, APS.

[DU 15] Du Z., Zeng X. M., Liu Q., Lai A., Amini S., Miserez A., Sceuh c. A., Gan c. L.
Size effects and shape memory properties in ZrO_2 ceramic micro- and nano-pillars. *Scripta Materialia*, vol. 101, 2015, p. 40–43, Elsevier.

[EHR 08] Ehre D., Chaim R.
Abnormal Hall–Petch behavior in nanocrystalline MgO ceramic. *Journal of Materials Science*, vol. 43, n° 18, 2008, p. 6139–6143, Springer.

[ELD 99] El-Danaf E., Kalidindi S. R., Doherty R. D.
Influence of grain size and stacking-fault energy on deformation twinning in fcc metals. *Metallurgical and Materials Transactions A*, vol. 30, n° 5, 1999, p. 1223–1233, Springer.

[ENN 16] Ennis B.
A review of the effects of chemical and phase segregation on the mechanical behaviour of multi-phase steels. *Condensed Matter Physics Materials Science*, , 2016.

[EWA 21] Ewald P. P.
Die Berechnung optischer und elektrostatischer Gitterpotentiale. *Annalen der Physik*, vol. 369, n° 3, 1921, p. 253–287, Wiley Online Library.

[FAH 17] Fahrenholtz W. G., Hilmas G. E.
Ultra-high temperature ceramics: materials for extreme environments. *Scripta Materialia*, vol. 129, 2017, p. 94–99, Elsevier.

[FAN 05] Fan G., Choo H., Liaw P., Lavernia E.
A model for the inverse Hall–Petch relation of nanocrystalline materials. *Materials Science and Engineering: A*, vol. 409, n° 1-2, 2005, p. 243–248, Elsevier.

[FER 16] Feruz Y., Mordehai D.
Towards a universal size-dependent strength of face-centered cubic nanoparticles. *Acta Materialia*, vol. 103, 2016, p. 433–441, Elsevier.

[FER 18] Fernández-González D., Ruiz-Bustinza I., González-Gasca C., Noval J. P., Moceón-Castaños J., Sancho-Gorostiaga J., Verdeja L. F.
Concentrated solar energy applications in materials science and metallurgy. *Solar Energy*, vol. 170, 2018, p. 520–540, Elsevier.

[FIR 76] Firestone R., Heuer A.
Creep deformation of 0° sapphire. *Journal of the American Ceramic Society*, vol. 59, n° 1-2, 1976, p. 24–29, Wiley Online Library.

[FUJ 00] Fujishima S.
The history of ceramic filters. *IEEE Transactions on Ultrasonics, Ferroelectrics, and Frequency Control*, vol. 47, n° 1, 2000, p. 1–7, IEEE.

[GAL 92] Gale J., Catlow C., Mackrodt W.
Periodic *ab initio* determination of interatomic potentials for alumina. *Modelling and Simulation in Materials Science and Engineering*, vol. 1, n° 1, 1992, Page 73, IOP Publishing.

[GAL 97] Gale J. D.
GULP: A computer program for the symmetry-adapted simulation of solids. *Journal of the Chemical Society, Faraday Transactions*, vol. 93, n° 4, 1997, p. 629–637, Royal Society of chemistry.

[GEI 94] Geipel T., Lagerlöf K., Pirouz P., Heuer A.
A zonal dislocation mechanism for rhombohedral twinning in sapphire (α-Al_2O_3). *Acta Metallurgica et Materialia*, vol. 42, n° 4, 1994, p. 1367–1372, Elsevier.

[GER 03] Gerberich W. W., Mook W., Perrey C., Carter C., Baskes M., Mukherjee R., Gidwani A., Heberlein J., McMurry P. H., Girshick S. L.
Superhard silicon nanospheres. *Journal of the Mechanics and Physics of Solids*, vol. 51, n° 6, 2003, p. 979–992, Elsevier.

[GER 12] Gerberich W. W., Stauffer D. D., Beaber A. R., Tymiak N. I.
A brittleness transition in silicon due to scale. *Journal of Materials Research*, vol. 27, n° 3, 2012, p. 552–561, Cambridge University Press.

[GIA 06] Gianola D., Van Petegem S., Legros M., Brandstetter S., Van Swygenhoven H., Hemker K.
Stress-assisted discontinuous grain growth and its effect on the deformation behavior of nanocrystalline aluminum thin films. *Acta Materialia*, vol. 54, n° 8, 2006, p. 2253–2263, Elsevier.

[GIE 68] Gieske J., Barsch G.
Pressure dependence of the elastic constants of single crystalline aluminum oxide. *Physica Status Solidi (b)*, vol. 29, n° 1, 1968, p. 121–131, Wiley Online Library.

[GON 94] Goniakowski J., Noguera C.
Electronic structure of clean insulating oxide surfaces I. A numerical approach. *Surface Science*, vol. 319, n° 1-2, 1994, p. 68–80, Elsevier.

[GOO 72] Gooch D., Groves G.
Prismatic slip in sapphire. *Journal of the American Ceramic Society*, vol. 55, n° 2, 1972, p. 105–105, Wiley Online Library.

[GOO 73] Gooch D., Groves G.
The creep of sapphire filament with orientations close to the *c*-axis. *Journal of Materials Science*, vol. 8, n° 9, 1973, p. 1238–1246, Springer.

[GOR 15] Goryaeva A. M., Carrez P., Cordier P.
Modeling defects and plasticity in $MgSiO_3$ post-perovskite: Part 1—generalized stacking faults. *Physics and Chemistry of Minerals*, vol. 42, n° 10, 2015, p. 781–792, Springer.

[GOR 19] Goryaeva A. M., Fusco C., Bugnet M., Amodeo J.
Influence of an amorphous surface layer on the mechanical properties of metallic nanoparticles under compression. *Physical Review Materials*, vol. 3, n° 3, 2019, Page 033606, APS.

[GRE 82] Green D. J.
Critical microstructures for microcracking in Al_2O_3-ZrO_2 composites. *Journal of the American Ceramic Society*, vol. 65, n° 12, 1982, p. 610–614, Wiley Online Library.

[GRE 11] Greer J. R., De Hosson J. T. M.
Plasticity in small-sized metallic systems: Intrinsic versus extrinsic size effect. *Progress in Materials Science*, vol. 56, n° 6, 2011, p. 654–724, Elsevier.

[GUA 04] Guazzato M., Albakry M., Ringer S. P., Swain M. V.
Strength, fracture toughness and microstructure of a selection of all-ceramic materials. Part I. Pressable and alumina glass-infiltrated ceramics. *Dental Materials*, vol. 20, n° 5, 2004, p. 441–448, Elsevier.

[GUE 98] Guenard P., Renaud G., Barbier A., Gautier-Soyer M.
Determination of the α-Al_2O_3 (0001) surface relaxation and termination by measurements of crystal truncation rods. *Surface Review and Letters*, vol. 5, n° 01, 1998, p. 321–324, World Scientific.

[GUÉ 20] Guénolé J., Nöhring W. G., Vaid A., Houllé F., Xie Z., Prakash A., Bitzek E.
Assessment and optimization of the fast inertial relaxation engine (fire) for energy minimization in atomistic simulations and its implementation in lammps. *Computational Materials Science*, vol. 175, 2020, Page 109584, Elsevier.

[GUO 18] Guo D., Song S., Luo R., Goddard III W. A., Chen M., Reddy K. M., An Q.
Grain boundary sliding and amorphization are responsible for the reverse Hall-Petch relation in superhard nanocrystalline boron carbide. *Physical Review Letters*, vol. 121, n° 14, 2018, Page 145504, APS.

[HAL 51] Hall E.
The deformation and ageing of mild steel: III discussion of results. *Proceedings of the Physical Society. Section B*, vol. 64, n° 9, 1951, Page 747, IOP Publishing.

[HAR 06] Hardy D. J.
Multilevel summation for the fast evaluation of forces for the simulation of biomolecules. University of Illinois at Urbana-Champaign, 2006.

[HAR 09] Hardy D. J., Stone J. E., Sceulten K.
Multilevel summation of electrostatic potentials using graphics processing units. *Parallel Computing*, vol. 35, n° 3, 2009, p. 164–177, Elsevier.

[HAR 13] Hardwicke C. U., Lau Y.-c.
Advances in thermal spray coatings for gas turbines and energy generation: a review. *Journal of Thermal Spray Technology*, vol. 22, n° 5, 2013, p. 564–576, Springer.

[HE 02] He Z.-M., Hu X.-Q., Zhou Z.-X.
Considerations on indications for surgery in patients with polypoid lesion of the gallbladder. *Academic Journal of the First Medical College of PLA*, vol. 22, n° 10, 2002, p. 951–952.

[HE 03] He G., Eckert J., Löser W., Schultz L.
Novel Ti-base nanostructure–dendrite composite with enhanced plasticity. *Nature Materials*, vol. 2, n° 1, 2003, p. 33–37, Nature Publishing Group.

[HE 14] He L., Tan Y., Wang X., Xu T., Hong X.
Microstructure and wear properties of Al_2O_3-CeO_2/Ni-base alloy composite coatings on aluminum alloys by plasma spray. *Applied Surface Science*, vol. 314, 2014, p. 760–767, Elsevier.

[HEN 71] Hench L. L., Splinter R. J., Allen W., Greenlee T.
Bonding mechanisms at the interface of ceramic prosthetic materials. *Journal of Biomedical Materials Research*, vol. 5, n° 6, 1971, p. 117–141, Wiley Online Library.

[HEU 66] Heuer A.
Deformation twinning in corundum. *The Philosophical Magazine: A Journal of Theoretical Experimental and Applied Physics*, vol. 13, n° 122, 1966, p. 379–393, Taylor & Francis.

[HEU 98] Heuer A., Lagerlöf K., Castaing J.
Slip and twinning dislocations in sapphire (α-Al_2O_3). *Philosophical Magazine A*, vol. 78, n° 3, 1998, p. 747–763, Taylor & Francis.

[HEU 10] Heuer A., Jia C., Lagerlöf K.
The core structure of basal dislocations in deformed sapphire (α-Al_2O_3). *Science*, vol. 330, n° 6008, 2010, p. 1227–1231, American Association for the Advancement of Science.

[HIR 82] Hirth J. P., Lothe J.
Theory of dislocations. John Willey and Sons John Willey and Sons, 01 1982.

[HIR 15] Hirel P.
Atomsk: A tool for manipulating and converting atomic data files. *Computer Physics Communications*, vol. 197, 2015, p. 212–219, Elsevier.

[HOC 75] Hockey B.
Pyramidal Slip on $\langle\bar{1}100\rangle\{11\bar{2}3\}$ and Basal Twinning in Al_2O_3. , 1975, p. 167–179, Springer.

[HOO 96] Hoover W. G., Holian B. L.
Kinetic moments method for the canonical ensemble distribution. *Physics Letters A*, vol. 211, n° 5, 1996, p. 253–257, Elsevier.

[HOW 16] Howard M. P., Anderson J. A., Nikoubashman A., Glotzer S. C., Panagiotopoulos A. Z.
Efficient neighbor list calculation for molecular simulation of colloidal systems using graphics processing units. *Computer Physics Communications*, vol. 203, 2016, p. 45–52, Elsevier.

[HUA 10] Huang L., Zhang Z., Zhao Y., Yao W., Mukherjee A. K., Schoenung J. M.
Scratch-induced deformation in fine- and ultrafine-grained bulk alumina. *Scripta Materialia*, vol. 63, n° 5, 2010, p. 528–531, Elsevier.

[HUA 20] Huang Z., Yong P., Zhou H., Li Y.
Grain size effect on deformation mechanisms and mechanical properties of titanium. *Materials Science and Engineering: A*, vol. 773, 2020, Page 138721, Elsevier.

[HUL 93] Hulbert S.
The use of alumina and zirconia in surgical implants. *Advanced Series in Ceramics*, vol. 1, 1993, p. 25–40, World Scientific Publishing.

[IMO 07] Imori M., Kanada Y.
Low voltage power supply incorporating ceramic transformer. *Topical Workshop on Electronics for Particle Physics (Former LECC Workshop), Prague, Czech Republic*, 2007, p. 03–07.

[ISH 80] Ishizawa N., Miyata T., Minato I., Marumo F., Iwai S.
A structural investigation of α-Al_2O_3 at 2170K. *Acta Crystallographica Section B: Structural Crystallography and Crystal Chemistry*, vol. 36, n° 2, 1980, p. 228–230, International Union of Crystallography.

[ISS 15] Issa I., Amodeo J., Réthoré J., Joly-Pottuz L., Esnouf C., Morthomas J., Perez M., Chevalier J., Masenelli-Varlot K.
In situ investigation of MgO nanocube deformation at room temperature. *Acta Materialia*, vol. 86, 2015, p. 295–304, Elsevier.

[ISS 18] Issa I., Joly-Pottuz L., Réthoré J., Esnouf C., Douillard T., Garnier V., Chevalier J., Le Floch S., Machon D., Masenelli-Varlot K.
Room temperature plasticity and phase transformation of nanometer-sized transition alumina nanoparticles under pressure. *Acta Materialia*, vol. 150, 2018, p. 308–316, Elsevier.

[ISS 21] Issa I., Joly-Pottuz L., Amodeo J., Dunstan D. J., Esnouf C., Réthoré J., Garnier V., Chevalier J., Masenelli-Varlot K.
From dislocation nucleation to dislocation multiplication in ceramic nanoparticle. *Materials Research Letters*, vol. 9, n° 6, 2021, p. 278–283, Taylor & Francis.

[JAH 06] Jahn S., Madden P. A., Wilson M.
Transferable interaction model for Al_2O_3. *Physical Review B*, vol. 74, n° 2, 2006, Page 024112, APS.

[JAN 12] Jang D., Li X., Gao H., Greer J. R.
Deformation mechanisms in nanotwinned metal nanopillars. *Nature Nanotechnology*, vol. 7, n° 9, 2012, Page 594, Nature Publishing Group.

[JIA 18] Jia W., Hou Y., Zheng M., Xu Y., Zhu M., Yang K., Cheng H., Sun S., Xing J.
Advances in lead-free high-temperature dielectric materials for ceramic capacitor application. *IET Nanodielectrics*, vol. 1, n° 1, 2018, p. 3–16, IET.

[JOH 87] Johnson K. L., Johnson K. L.
Contact Mechanics. Cambridge university press, 1987.

[KAL 07] Kalita S. J., Bhardwaj A., Bhatt H. A.
Nanocrystalline calcium phosphate ceramics in biomedical engineering. *Materials Science and Engineering: C*, vol. 27, n° 3, 2007, p. 441–449, Elsevier.

[KE 95] Ke M., Hackney S., Milligan W., Aifantis E.
Observation and measurement of grain rotation and plastic strain in nanostructured metal thin films. *Nanostructured Materials*, vol. 5, n° 6, 1995, p. 689–697, Elsevier.

[KEA 03] Keane M.
Ceramics for catalysis. *Journal of Materials Science*, vol. 38, n° 23, 2003, p. 4661–4675, Springer.

[KIE 08] Kiener D., Grosinger W., Dehm G., Pippan R.
A further step towards an understanding of size-dependent crystal plasticity: In situ tension experiments of miniaturized single-crystal copper samples. *Acta Materialia*, vol. 56, n° 3, 2008, p. 580–592, Elsevier.

[KIL 18] Kilymis D., Gérard C., Amodeo J., Waghmare U., Pizzagalli L.
Uniaxial compression of silicon nanoparticles: an atomistic study on the shape and size effects. *Acta Materialia*, vol. 158, 2018, p. 155–166, Elsevier.

[KIM 07] Kim H., Priya S., Stephanou H., Uchino K.
Consideration of impedance matching techniques for efficient piezoelectric energy harvesting. *IEEE Transactions on Ultrasonics, Ferroelectrics, and Frequency Control*, vol. 54, n° 9, 2007, p. 1851–1859, IEEE.

[KIM 18] Kim H. T.
High thermal conductivity ceramics and their composites for thermal management of

integrated electronic packaging. *Heat Transfer-Models, Methods and Applications*, , 2018, p. 333–359.

[KIM 19] Kim W. K., Xi D., Kim B. H.
Nanoscale indentation and scratching tests of single crystal sapphire using molecular dynamics simulation. *Computational Materials Science*, vol. 170, 2019, Page 109195, Elsevier.

[KNÖ 78] Knözinger H., Ratnasamy P.
Catalytic aluminas: surface models and characterization of surface sites. *Catalysis Reviews Science and Engineering*, vol. 17, n° 1, 1978, p. 31–70, Taylor & Francis.

[KON 21] Konstantiniuk F., Tkadletz M., Kainz C., Czettl C., Schalk N.
Mechanical properties of single and polycrystalline α-Al_2O_3 coatings grown by chemical vapor deposition. *Surface and Coatings Technology*, vol. 410, 2021, Page 126959, Elsevier.

[KOR 11a] Korte S., Clegg W.
Discussion of the dependence of the effect of size on the yield stress in hard materials studied by microcompression of MgO. *Philosophical Magazine*, vol. 91, n° 7-9, 2011, p. 1150–1162, Taylor & Francis.

[KOR 11b] Korte S., Ritter M., Jiao c., Midgley P., Clegg W.
Three-dimensional electron backscattered diffraction analysis of deformation in MgO micropillars. *Acta Materialia*, vol. 59, n° 19, 2011, p. 7241–7254, Elsevier.

[KOT 82] Kotchick D., Busovne B., Tressler R., Barber D.
Dynamics of flow of c-axis sapphire. *Journal of Materials Science*, vol. 17, n° 7, 1982, p. 1977–1987, Springer.

[KOU 14] Kou H., Lu J., Li Y.
High-strength and high-ductility nanostructured and amorphous metallic materials. *Advanced Materials*, vol. 26, n° 31, 2014, p. 5518–5524, Wiley Online Library.

[KOV 96] Kovar D., Readey M. J.
Grain size distributions and strength variability of high-purity alumina. *Journal of the American Ceramic Society*, vol. 79, n° 2, 1996, p. 305–312, Wiley Online Library.

[KOV 00] Kovar D., Bennison S. J., Readey M. J.
Crack stability and strength variability in alumina ceramics with rising toughness-curve behavior. *Acta Materialia*, vol. 48, n° 2, 2000, p. 565–578, Elsevier.

[KRO 57] Kronberg M.
Plastic deformation of single crystals of sapphire: basal slip and twinning. *Acta Metallurgica*, vol. 5, n° 9, 1957, p. 507–524, Elsevier.

[KUK 12] Kuksin A. Y., Yanilkin A.
Formation of twins in sapphire under shock wave loading: atomistic simulations. *Journal of Applied Physics*, vol. 111, n° 3, 2012, Page 033513, American Institute of Physics.

[KUM 03] Kumar K., Van Swygenhoven H., Suresh S.
Mechanical behavior of nanocrystalline metals and alloys. *Acta Materialia*, vol. 51, n° 19, 2003, p. 5743–5774, Elsevier.

[KUR 10] Kurita T., Uchida K., Oshiyama A.
Atomic and electronic structures of α-Al_2O_3 surfaces. *Physical Review B*, vol. 82, n° 15, 2010, Page 155319, APS.

[KUR 20] Kuroyanagi S., Shinoda K., Yumoto A., Akedo J.
Size-dependent quasi Brittle–Ductile transition of single crystalline alpha-alumina particles during microcompression tests. *Acta Materialia*, vol. 195, 2020, p. 588–596, Elsevier.

[KWA 06] Kwak J. H., Kim D. H., Szailer T., Peden c. H., Szanyi J.
NO_x uptake mechanism on $Pt/BaO/Al_2O_3$ catalysts. *Catalysis Letters*, vol. 111, n° 3, 2006, p. 119–126, Springer.

[LAG 83] Lagerlöf K. P. D., Pletka B., Mitchell T., Heuer A.
Deformation and diffusion in sapphire (α-Al_2O_3). *Radiation Effects*, vol. 74, n° 1-4, 1983, p. 87–107, Taylor & Francis.

[LAG 94] Lagerlöf K. P. D., Heuer A. H., Castaing J., Rivière J. P., Mitchell T. E.
Slip and twinning in sapphire (α-Al_2O_3). *Journal of the American Ceramic Society*, vol. 77, n° 2, 1994, p. 385–397, Wiley Online Library.

[LAG 02] Lagerlöf K., Castaing J., Pirouz P., Heuer A.
Nucleation and growth of deformation twins: a perspective based on the double-cross-slip mechanism of deformation twinning. *Philosophical Magazine A*, vol. 82, n° 15, 2002, p. 2841–2854, Taylor & Francis.

[LAN 16] Lange A., Samanta A., Majidi H., Mahajan S., Ging J., Olson T., van Benthem K., Elhadj S.
Dislocation mediated alignment during metal nanoparticle coalescence. *Acta Materialia*, vol. 120, 2016, p. 364–378, Elsevier.

[LAU 20] Laurens G., Amans D., Lam J., Allouche A.-R.
Comparison of aluminum oxide empirical potentials from cluster to nanoparticle. *Physical Review B*, vol. 101, n° 4, 2020, Page 045427, APS.

[LEE 85] Lee W., Lagerlöf K.
Structural and electron diffraction data for sapphire (α-Al_2O_3). *Journal of Electron Microscopy Technique*, vol. 2, n° 3, 1985, p. 247–258, Wiley Online Library.

[LEG 08] Legros M., Gianola D. S., Hemker K. J.
In situ TEM observations of fast grain-boundary motion in stressed nanocrystalline aluminum films. *Acta Materialia*, vol. 56, n° 14, 2008, p. 3380–3393, Elsevier.

[LEI 13] Lei Y., Gong Y., Duan Z., Wang G.
Density functional calculation of activation energies for lattice and grain boundary diffusion in alumina. *Physical Review B*, vol. 87, n° 21, 2013, Page 214105, APS.

[LEW 82] Lewis J., Schwarzenbace D., Flack H.
Electric field gradients and charge density in corundum, α-Al_2O_3. *Acta Crystallographica Section A: Crystal Physics, Diffraction, Theoretical and General Crystallography*, vol. 38, n° 5, 1982, p. 733–739, International Union of Crystallography.

[LEW 85] Lewis G., Catlow C.
Potential models for ionic oxides. *Journal of Physics C: Solid State Physics*, vol. 18, n° 6, 1985, Page 1149, IOP Publishing.

[LI 14] Li R. W. K., Chow T. W., Matinlinna J. P.
Ceramic dental biomaterials and CAD/CAM technology: state of the art. *Journal of Prosthodontic Research*, vol. 58, n° 4, 2014, p. 208–216, Japan Prosthodontic Society.

[LIA 14] Liang T., cheng Y.-T., Nie X., Luo W., Asthagiri A., Janik M. J., Andrews E., Flake J., Sinnott S. B.
Molecular dynamics simulations of CO_2 reduction on Cu (111) and Cu/ZnO ($10\bar{1}0$) using charge optimized many body potentials. *Catalysis Communications*, vol. 52, 2014, p. 84–87, Elsevier.

[LIL 10] Lilleodden E.
Microcompression study of Mg (0001) single crystal. *Scripta Materialia*, vol. 62, n° 8, 2010, p. 532–535, Elsevier.

[LIU 20] Liu D., Jiang P., Li X., Liu J., Zhou L., Wang X., Zhou F.
3D printing of metal-organic frameworks decorated hierarchical porous ceramics for high-efficiency catalytic degradation. *Chemical Engineering Journal*, vol. 397, 2020, Page 125392, Elsevier.

[LUK 17] Lukianova O., Novikov V. Y., Parkhomenko A., Sirota V., Krasilnikov V.
Microstructure of spark plasma-sintered silicon nitride ceramics. *Nanoscale Research Letters*, vol. 12, n° 1, 2017, p. 1–6, Springer.

[MA 20] Ma Y., Cao L., Hang W., Zhang T., Yuan J.
Crystallographic orientation effect on the incipient plasticity and its stochastic behavior of a sapphire single crystal by spherical nanoindentation. *Ceramics International*, vol. 46, n° 10, 2020, p. 15554–15564, Elsevier.

[MAN 02] Manasilp A., Gulari E.
Selective CO oxidation over Pt/alumina catalysts for fuel cell applications. *Applied Catalysis B: Environmental*, vol. 37, n° 1, 2002, p. 17–25, Elsevier.

[MAO 11] Mao W., Shen Y., Lu C.
Nanoscale elastic–plastic deformation and stress distributions of the C plane of sapphire

single crystal during nanoindentation. *Journal of the European Ceramic Society*, vol. 31, n° 10, 2011, p. 1865–1871, Elsevier.

[MAR 01] Marinopoulos A., Elsässer C.
Density-functional and shell-model calculations of the energetics of basal-plane stacking faults in sapphire. *Philosophical Magazine Letters*, vol. 81, n° 5, 2001, p. 329–338, Taylor & Francis.

[MAR 04] Marmier A., Parker S. C.
Ab initio morphology and surface thermodynamics of α-Al_2O_3 surfaces. *Physical Review B*, vol. 69, n° 11, 2004, Page 115409, APS.

[MAR 08] Mara N., Bhattacharyya D., Dickerson P., Hoagland R., Misra A.
Deformability of ultrahigh strength 5 nm Cu/Nb nanolayered composites. *Applied Physics Letters*, vol. 92, n° 23, 2008, Page 231901, American Institute of Physics.

[MAR 10] Martens J. et al.
Deep learning via hessian-free optimization. *ICML*, vol. 27, 2010, p. 735–742.

[MAR 11] Marinopoulos A., Grüning M.
Local-field and excitonic effects in the optical response of α-alumina. *Physical Review B*, vol. 83, n° 19, 2011, Page 195129, APS.

[MAS 14] Massin P., Lopes R., Masson B., Mainard D., Hip F.
Does Biolox® Delta ceramic reduce the rate of component fractures in total hip replacement? *Orthopaedics and Traumatology: Surgery and Research*, vol. 100, n° 6, 2014, p. S317–S321, Elsevier.

[MAT 94] Matsui M.
A transferable interatomic potential model for crystals and melts in the system CaO-MgO-Al_2O_3-SiO_2. *Mineralogical Magazine*, vol. 58, n° 2, 1994, p. 571–572.

[MAT 96] Matsui M.
Molecular dynamics study of the structures and bulk moduli of crystals in the system CaO-MgO-Al_2O_3-SiO_2. *Physics and Chemistry of Minerals*, vol. 23, n° 6, 1996, p. 345–353, Springer.

[MAY 60] Mayer W. G., Hiedemann E.
Corrected values of the elastic moduli of sapphire. *The Journal of the Acoustical Society of America*, vol. 32, n° 12, 1960, p. 1699–1700, Acoustical Society of America.

[MBO 19] Mbongo D., Tétot R., Ducher R., Dubourg R., Salles N.
Improved SMTB−Q model applied to oxygen migration and pressure phase transitions in UO_2. *Journal of Physics: Condensed Matter*, vol. 32, n° 9, 2019, Page 095701, IOP Publishing.

[MEN 07] Mendelev M. I., Ackland G. J.
Development of an interatomic potential for the simulation of phase transformations in zirconium. *Philosophical Magazine Letters*, vol. 87, n° 5, 2007, p. 349–359, Taylor & Francis.

[MEN 08] Mendelev M., Kramer M., Becker C. A., Asta M.
Analysis of semi-empirical interatomic potentials appropriate for simulation of crystalline and liquid Al and Cu. *Philosophical Magazine*, vol. 88, n° 12, 2008, p. 1723–1750, Taylor & Francis.

[MES 98] Mesa A. D. S., Quesne C., Smirnov Y. F.
Generalized Morse potential: symmetry and satellite potentials. *Journal of Physics A: Mathematical and General*, vol. 31, n° 1, 1998, Page 321, IOP Publishing.

[MIA 19] Miao B., Kondo S., Tochigi E., Wei J., Feng B., Shibata N., Ikuhara Y.
The core structure of 60° mixed basal dislocation in alumina (α-Al_2O_3) introduced by in situ TEM nanoindentation. *Scripta Materialia*, vol. 163, 2019, p. 157–162, Elsevier.

[MIS 01] Mishin Y., Mehl M., Papaconstantopoulos D., Voter A., Kress J.
Structural stability and lattice defects in copper: Ab initio, tight-binding, and embedded-atom calculations. *Physical Review B*, vol. 63, n° 22, 2001, Page 224106, APS.

[MIT 93] Mitchell P., Fincham D.
Shell model simulations by adiabatic dynamics. *Journal of Physics: Condensed Matter*, vol. 5, n° 8, 1993, Page 1031, IOP Publishing.

[MIT 95] Mitomo M., Petzow G.
Recent progress in silicon nitride and silicon carbide ceramics. *MRS Bulletin*, vol. 20, n° 2, 1995, p. 19–22, Cambridge University Press.

[MON 14] Montagne A., Pathak S., Maeder X., Michler J.
Plasticity and fracture of sapphire at room temperature: load-controlled microcompression of four different orientations. *Ceramics International*, vol. 40, n° 1, 2014, p. 2083–2090, Elsevier.

[MOO 07] Mook W., Nowak J., Perrey C., Carter C., Mukherjee R., Girshick S., McMurry P., Gerberich W.
Compressive stress effects on nanoparticle modulus and fracture. *Physical Review B*, vol. 75, n° 21, 2007, Page 214112, APS.

[MOR 01] Morris Jr J.
The influence of grain size on the mechanical properties of steel. *Powered by the California Digital Library University of California*, , 2001.

[MOR 11] Mordehai D., Lee S.-W., Backes B., Srolovitz D. J., Nix W. D., Rabkin E.
Size effect in compression of single-crystal gold microparticles. *Acta Materialia*, vol. 59, n° 13, 2011, p. 5202–5215, Elsevier.

[MOR 18] Mordehai D., David O., Kositski R.
Nucleation-Controlled Plasticity of Metallic Nanowires and Nanoparticles. *Advanced Materials*, vol. 30, n° 41, 2018, Page 1706710, Wiley Online Library.

[MUN 97] Munro M.
Evaluated material properties for a sintered alpha-alumina. *Journal of the American Ceramic Society*, vol. 80, n° 8, 1997, p. 1919–1928, Wiley Online Library.

[MUR 20] Murata K., Ohyama J., Yamamoto Y., Arai S., Satsuma A.
Methane Combustion over Pd/Al_2O_3 Catalysts in the presence of water: effects of Pd particle size and alumina crystalline phase. *ACS Catalysis*, vol. 10, n° 15, 2020, p. 8149–8156, ACS Publications.

[MUT 03] Muttamara A., Fukuzawa Y., Mohri N., Tani T.
Probability of precision micro-machining of insulating Si_3N_4 ceramics by EDM. *Journal of Materials Processing Technology*, vol. 140, n° 1-3, 2003, p. 243–247, Elsevier.

[NAB 47] Nabarro F.
Dislocations in a simple cubic lattice. *Proceedings of the Physical Society (1926-1948)*, vol. 59, n° 2, 1947, Page 256, IOP Publishing.

[NAG 13] Naglieri V., Palmero P., Montanaro L., Chevalier J.
Elaboration of alumina-zirconia composites: Role of the zirconia content on the microstructure and mechanical properties. *Materials*, vol. 6, n° 5, 2013, p. 2090–2102, Multidisciplinary Digital Publishing Institute.

[NAS 85] Nash S. G.
Preconditioning of truncated-Newton methods. *SIAM Journal on Scientific and Statistical Computing*, vol. 6, n° 3, 1985, p. 599–616, SIAM.

[NEV 01] Nevelos J., Prudhommeaux F., Hamadouche M., Doyle C., Ingham E., Meunier A., Nevelos A., Sedel L., Fisher J.
Comparative analysis of two different types of alumina-alumina hip prosthesis retrieved for aseptic loosening. *The Journal of Bone and Joint Surgery*, vol. 83, n° 4, 2001, p. 598–603, The British Editorial Society of Bone and Joint Surgery.

[NIE 02] Nie X., Meletis E., Jiang J., Leyland A., Yerokhin A., Matthews A.
Abrasive wear/corrosion properties and TEM analysis of Al_2O_3 coatings fabricated using plasma electrolysis. *Surface and Coatings Technology*, vol. 149, n° 2-3, 2002, p. 245–251, Elsevier.

[NIS 08] Nishimura K., Kalia R. K., Nakano A., Vashishta P.
Nanoindentation hardness anisotropy of alumina crystal: A molecular dynamics study. *Applied Physics Letters*, vol. 92, n° 16, 2008, Page 161904, American Institute of Physics.

[NOS 02] Nosé S. U. I.
A molecular dynamics method for simulations in the canonical ensemble. *Molecular Physics*, vol. 100, n° 1, 2002, p. 191–198, Taylor & Francis.

[OGA 05] Ogata S., Li J., Yip S.
Energy landscape of deformation twinning in bcc and fcc metals. *Physical Review B*, vol. 71, n° 22, 2005, Page 224102, APS.

[OHN 86] Ohno I., Yamamoto S., Anderson O. L., Noda J.
Determination of elastic constants of trigonal crystals by the rectangular parallelepiped resonance method. *Journal of Physics and Chemistry of Solids*, vol. 47, n° 12, 1986, p. 1103–1108, Elsevier.

[OKA 09] Okada A.
Ceramic technologies for automotive industry: Current status and perspectives. *Materials Science and Engineering: B*, vol. 161, n° 1-3, 2009, p. 182–187, Elsevier.

[OLI 92] Oliver W. C., Pharr G. M.
An improved technique for determining hardness and elastic modulus using load and displacement sensing indentation experiments. *Journal of Materials Research*, vol. 7, n° 6, 1992, p. 1564–1583, Cambridge University Press.

[OPI 03] Opila E. J., Robinson R. C., Fox D. S., Wenglarz R. A., Ferber M. K.
Additive effects on Si_3N_4 oxidation/volatilization in water vapor. *Journal of the American Ceramic Society*, vol. 86, n° 8, 2003, p. 1262–1271, Wiley Online Library.

[ORM 03] Ormerod R. M.
Solid oxide fuel cells. *Chemical Society Reviews*, vol. 32, n° 1, 2003, p. 17–28, Royal Society of chemistry.

[PEI 40] Peierls R.
The size of a dislocation. *Proceedings of the Physical Society (1926-1948)*, vol. 52, n° 1, 1940, Page 34, IOP Publishing.

[PIT 03] Piticescu R. M., Piticescu R., Taloi D., Badilita V.
Hydrothermal synthesis of ceramic nanomaterials for functional applications. *Nanotechnology*, vol. 14, n° 2, 2003, Page 312, IOP Publishing.

[PLI 95] Plimpton S.
Fast parallel algorithms for short-range molecular dynamics. *Journal of Computational Physics*, vol. 117, n° 1, 1995, p. 1–19, Elsevier.

[POL 69] Polak E., Ribiere G.
Note sur la convergence de méthodes de directions conjuguées. *ESAIM: Mathematical Modelling and Numerical Analysis-Modélisation Mathématique et Analyse Numérique*, vol. 3, n° R1, 1969, p. 35–43.

[RAP 91] Rappe A. K., Goddard III W. A.
Charge equilibration for molecular dynamics simulations. *The Journal of Physical Chemistry*, vol. 95, n° 8, 1991, p. 3358–3363, ACS Publications.

[RIC 54] Rice W. E., Hirschfelder J. O.
Second virial coefficients of gases obeying a modified Buckingham (exp—six) potential. *The Journal of Chemical Physics*, vol. 22, n° 2, 1954, p. 187–192, American Institute of Physics.

[RIC 74] Rice J. R., Thomson R.
Ductile versus brittle behaviour of crystals. *The Philosophical Magazine: A Journal of Theoretical Experimental and Applied Physics*, vol. 29, n° 1, 1974, p. 73–97, Taylor & Francis.

[RIC 09] Richter G., Hillerice K., Gianola D. S., Monig R., Kraft O., Volkert C. A.
Ultrahigh strength single crystalline nanowhiskers grown by physical vapor deposition. *Nano Letters*, vol. 9, n° 8, 2009, p. 3048–3052, ACS Publications.

[ROB 93] Roberts S., Kim H., Hirsch P.
The brittle-ductile transition and dislocation mobility in silicon and sapphire. *Strength of Metals and Alloys*, vol. 1, 1993, p. 317–317, FREUND PUBLISHING COMPANY.

[ROU 10] Roualdes O., Duclos M.-E., Gutknecet D., Frappart L., Chevalier J., Hartmann D. J.
In vitro and in vivo evaluation of an alumina–zirconia composite for arthroplasty applications. *Biomaterials*, vol. 31, n° 8, 2010, p. 2043–2054, Elsevier.

[RUB 03] Ruberto C., Yourdshahyan Y., Lundqvist B. I.
Surface properties of metastable alumina: A comparative study of κ- and α-Al_2O_3. *Physical Review B*, vol. 67, n° 19, 2003, Page 195412, APS.

[RYO 18] Ryou H., Drazin J. W., Wahl K. J., Qadri S. B., Gorzkowski E. P., Feigelson B. N., Wollmershauser J. A.
Below the Hall–Petch limit in nanocrystalline ceramics. *ACS Nano*, vol. 12, n° 4, 2018, p. 3083–3094, ACS Publications.

[SAL 94] Salem J. A., Li Z., Bradt R. C.
Thermal expansion and elastic anisotropy in single crystal Al_2O_3 and SiC Reinforcements. *Conference: American Society of Mechanical Engineers winter meeting, Anaheim, CA (United States)*, , 1994.

[SAL 16] Salles N., Politano O., Amzallag E., Tétot R.
Molecular dynamics study of high-pressure alumina polymorphs with a tight-binding variable-charge model. *Computational Materials Science*, vol. 111, 2016, p. 181–189, Elsevier.

[SAL 18] Salah S. B. H.
Plasticité des nanoparticules métalliques cubiques à faces centrées. Thèse de doctorat, ISAE-ENSMA Ecole Nationale Supérieure de Mécanique et d'Aérotechique-Poitiers, 2018.

[SAM 13] Samavedi S., Whittington A. R., Goldstein A. S.
Calcium phosphate ceramics in bone tissue engineering: a review of properties and their influence on cell behavior. *Acta Biomaterialia*, vol. 9, n° 9, 2013, p. 8037–8045, Elsevier.

[SAM 21] Samae V., Cordier P., Demouchy S., Bollinger C., Gasc J., Koizumi S., Mussi A., Schryvers D., Idrissi H.
Stress-induced amorphization triggers deformation in the lithospheric mantle. *Nature*, vol. 591, n° 7848, 2021, p. 82–86, Nature Publishing Group.

[SAN 08] Santa Cruz H., Spino J., Grathwohl G.
Nanocrystalline ZrO_2 ceramics with idealized macropores. *Journal of the European Ceramic Society*, vol. 28, n° 9, 2008, p. 1783–1791, Elsevier.

[SAR 13] Sarsam J., Finnis M. W., Tangney P.
Atomistic force field for alumina fit to density functional theory. *The Journal of Chemical physics*, vol. 139, n° 20, 2013, Page 204704, American Institute of Physics.

[SAR 16] Sarobol P., Chandross M., Carroll J. D., Mook W. M., Bufford D. C., Boyce B. L., Hattar K., Kotula P. G., Hall A. C.
Room temperature deformation mechanisms of alumina particles observed from in situ micro-compression and atomistic simulations. *Journal of Thermal Spray Technology*, vol. 25, n° 1-2, 2016, p. 82–93, Springer.

[SCH 66] Schröder U.
A new model for lattice dynamics ("breathing shell model"). *Solid State Communications*, vol. 4, n° 7, 1966, p. 347–349, Elsevier.

[SCH 72] Schneider S. J., Rice R. W.
The Science of ceramic Machining and Surface Finishing: Proceedings... N° 348 US Department of Commerce, 1972.

[SCH 98] Schiøtz J., Di Tolla F. D., Jacobsen K. W.
Softening of nanocrystalline metals at very small grain sizes. *Nature*, vol. 391, n° 6667, 1998, p. 561–563, Nature Publishing Group.

[SCH 09] Schneider A., Kaufmann D., Clark B., Frick C., Gruber P., Mönig R., Kraft O., Arzt E.
Correlation between critical temperature and strength of small-scale bcc pillars. *Physical Review Letters*, vol. 103, n° 10, 2009, Page 105501, APS.

[SCI 13] Sciti D., Silvestroni L., Mercatelli L., Sans J.-L., Sani E.
Suitability of ultra-refractory diboride ceramics as absorbers for solar energy applications. *Solar Energy Materials and Solar Cells*, vol. 109, 2013, p. 8–16, Elsevier.

[SCO 83] Scott W. D., Orr K.
Rhombohedral twinning in alumina. *Journal of the American Ceramic Society*, vol. 66, n° 1, 1983, p. 27–32, Wiley Online Library.

[SED 12] Sedlmayr A., Bitzek E., Gianola D. S., Richter G., Mönig R., Kraft O.
Existence of two twinning-mediated plastic deformation modes in Au nanowhiskers. *Acta Materialia*, vol. 60, n° 9, 2012, p. 3985–3993, Elsevier.

[SHA 09] Sharifi E. M., Karimzadeh F., Enayati M.
A study on mechanochemical behavior of B_2O_3−Al system to produce alumina-based nanocomposite. *Journal of Alloys and Compounds*, vol. 482, n° 1-2, 2009, p. 110–113, Elsevier.

[SHA 10] Shan T.-R., Devine B. D., Kemper T. W., Sinnott S. B., Phillpot S. R. et al.
Charge-optimized many-body potential for the hafnium/hafnium oxide system. *Physical Review B*, vol. 81, n° 12, 2010, Page 125328, APS.

[SHA 18] Sharma A., Hickman J., Gazit N., Rabkin E., Mishin Y.
Nickel nanoparticles set a new record of strength. *Nature Communications*, vol. 9, n° 1, 2018, p. 1–9, Nature Publishing Group.

[SHI 07] Shibata N., Chisholm M., Nakamura A., Pennycook S., Yamamoto T., Ikuhara Y.
Nonstoichiometric dislocation cores in α-alumina. *Science*, vol. 316, n° 5821, 2007, p. 82–85, American Association for the Advancement of Science.

[SHI 10] Shirai T., Watanabe H., Fuji M., Takahashi M. et al.
Structural properties and surface characteristics on aluminum oxide powders. *Annual Report of the Ceramics Research Laboratory Nagoya Institute of Technology*, , 2010.

[SHI 17] Shih P.-H., Wu S. Y.
Growth mechanism studies of ZnO nanowires: Experimental observations and short-circuit diffusion analysis. *Nanomaterials*, vol. 7, n° 7, 2017, Page 188, Multidisciplinary Digital Publishing Institute.

[SIE 02] Siegel D. J., Hector Jr L. G., Adams J. B.
Adhesion, atomic structure, and bonding at the Al (111)/α-Al_2O_3 (0001) interface: A first principles study. *Physical Review B*, vol. 65, n° 8, 2002, Page 085415, APS.

[SNO 73] Snow J., Heuer A.
Slip systems in Al_2O_3. *Journal of the American Ceramic Society*, vol. 56, n° 3, 1973, p. 153–157, Wiley Online Library.

[SOK 17] Sokol M., Halabi M., Mordekovitz Y., Kalabukhov S., Hayun S., Frage N.
An inverse Hall-Petch relation in nanocrystalline $MgAl_2O_4$ spinel consolidated by high pressure spark plasma sintering (HPSPS). *Scripta Materialia*, vol. 139, 2017, p. 159–161, Elsevier.

[SON 05] Song Y. H., Hwang J. H., Han Y. H.
Effects of Y_2O_3 on temperature stability of acceptor-doped $BaTiO_3$. *Japanese Journal of Applied Physics*, vol. 44, n° 3R, 2005, Page 1310, IOP Publishing.

[STI 85] Stillinger F. H., Weber T. A.
Computer simulation of local order in condensed phases of silicon. *Physical Review B*, vol. 31, n° 8, 1985, Page 5262, APS.

[STR 94] Streitz F., Mintmire J.
Electrostatic potentials for metal-oxide surfaces and interfaces. *Physical Review B*, vol. 50, n° 16, 1994, Page 11996, APS.

[STU 09] Stukowski A.
Visualization and analysis of atomistic simulation data with OVITO-the Open Visualization Tool. *Modelling and Simulation in Materials Science and Engineering*, vol. 18, n° 1, 2009, Page 015012, IOP Publishing.

[STU 10] Stukowski A., Albe K.
Extracting dislocations and non-dislocation crystal defects from atomistic simulation data. *Modelling and Simulation in Materials Science and Engineering*, vol. 18, n° 8, 2010, Page 085001, IOP Publishing.

[SUN 06] Sun J., Stirner T., Hagston W., Leyland A., Matthews A.
A simple transferable interatomic potential model for binary oxides applied to bulk α-Al_2O_3 and the (0001) α-Al_2O_3 surface. *Journal of Crystal Growth*, vol. 290, n° 1, 2006, p. 235–240, Elsevier.

[TEF 66] Tefft W. E.
Elastic constants of synthetic single crystal corundum. *Journal of Research of the National Bureau of Standards. Section A, Physics and Chemistry*, vol. 70, n° 4, 1966, Page 277, National Institute of Standards and Technology.

[TEP 00] Tepesch P., Quong A.
First-principles calculations of α-alumina (0001) surfaces energies with and without hydrogen. *Physica Status Solidi (B)*, vol. 217, n° 1, 2000, p. 377–387, Wiley Online Library.

[TÉT 08] Tétot R., Hallil A., Creuze J., Braems I.
Tight-binding variable-charge model for insulating oxides: Application to TiO_2 and ZrO_2 polymorphs. *EPL (Europhysics Letters)*, vol. 83, n° 4, 2008, Page 40001, IOP Publishing.

[TÉT 13] Tétot R., Salles N., Landron S., Amzallag E.
$SrTiO_3$ (001) surface and strained thin films: Atomic simulations using a tight-binding variable-charge model. *Surface Science*, vol. 616, 2013, p. 19–28, Elsevier.

[TON 20] Tong Z., Ji H., Li X., Liu Z.
Microstructure control and optimization of low temperature pressure less sintered silicon nitride-barium aluminosilicate composites. *Journal of the European Ceramic Society*, vol. 40, n° 12, 2020, p. 4177–4183, Elsevier.

[TSU 14] Tsuruta K., Tochigi E., Kezuka Y., Takata K., Shibata N., Nakamura A., Ikuhara Y.
Core structure and dissociation energetics of basal edge dislocation in α-Al_2O_3: A combined atomistic simulation and transmission electron microscopy analysis. *Acta Materialia*, vol. 65, 2014, p. 76–84, Elsevier.

[TUA 02] Tuan W., Chen R., Wang T., Cheng C., Kuo P.
Mechanical properties of Al_2O_3/ZrO_2 composites. *Journal of the European Ceramic Society*, vol. 22, n° 16, 2002, p. 2827–2833, Elsevier.

[UCH 04] Uchic M. D., Dimiduk D. M., Florando J. N., Nix W. D.
Sample dimensions influence strength and crystal plasticity. *Science*, vol. 305, n° 5686, 2004, p. 986–989, American Association for the Advancement of Science.

[ÜNA 94] Ünal Ö., Lagerlöf K. P. D.
Tensile Properties of Alumina Fibers Using Hot-Grips. *Journal of the American Ceramic Society*, vol. 77, n° 10, 1994, p. 2609–2614, Wiley Online Library.

[VAL 02] Valiev R., Alexandrov I., Zhu Y., Lowe T.
Paradox of strength and ductility in metals processed by severe plastic deformation. *Journal of Materials Research*, vol. 17, n° 1, 2002, p. 5–8, Springer.

[VAN 01a] Van Duin A. C., Dasgupta S., Lorant F., Goddard W. A.
ReaxFF: a reactive force field for hydrocarbons. *The Journal of Physical Chemistry A*, vol. 105, n° 41, 2001, p. 9396–9409, ACS Publications.

[VAN 01b] Van Swygenhoven H., Derlet P.
Grain-boundary sliding in nanocrystalline fcc metals. *Physical Review B*, vol. 64, n° 22, 2001, Page 224105, APS.

[VAN 04] Van Swygenhoven H., Derlet P. M., Frøseth A.
Stacking fault energies and slip in nanocrystalline metals. *Nature Materials*, vol. 3, n° 6, 2004, p. 399–403, Nature Publishing Group.

[VAS 90] Vashishta P., Kalia R. K., Rino J. P., Ebbsjö I.
Interaction potential for SiO_2: A molecular-dynamics study of structural correlations. *Physical Review B*, vol. 41, n° 17, 1990, Page 12197, APS.

[VAS 07] Vashishta P., Kalia R. K., Nakano A., Rino J. P.
Interaction potential for silicon carbide: A molecular dynamics study of elastic constants and vibrational density of states for crystalline and amorphous silicon carbide. *Journal of Applied Physics*, vol. 101, n° 10, 2007, Page 103515, American Institute of Physics.

[VAS 08] Vashishta P., Kalia R. K., Nakano A., Rino J. P.
Interaction potentials for alumina and molecular dynamics simulations of amorphous and liquid alumina. *Journal of Applied Physics*, vol. 103, n° 8, 2008, Page 083504, American Institute of Physics.

[VAS 20] Rego de Vasconcelos B., Pham Minh D., Martins E., Germeau A., Sharrock P., Nzihou A.
A comparative study of hydroxyapatite-and alumina-based catalysts in dry reforming of methane. *Chemical Engineering and Technology*, vol. 43, n° 4, 2020, p. 698–704, Wiley Online Library.

[VEN 94] Vendik I. B., Vendik O. G., Gevorgian S. S., Sitnikova M. F., Olsson E.
A CAD model for microstrips on r-cut sapphire substrates. *International Journal of Microwave and Millimeter-Wave Computer-Aided Engineering*, vol. 4, n° 4, 1994, p. 374–383, Wiley Online Library.

[VER 67] Verlet L.
Computer" experiments" on classical fluids. I. Thermodynamical properties of Lennard-Jones molecules. *Physical Review*, vol. 159, n° 1, 1967, Page 98, APS.

[VER 17] Verma V., Kumar B. M.
Synthesis, microstructure and mechanical properties of $Al_2O_3/ZrO_2/CeO_2$ composites with addition of nickel and titania processed by conventional sintering. *Materials Today: Proceedings*, vol. 4, n° 2, 2017, p. 3062–3071, Elsevier.

[VIN 01] Vink R., Barkema G., Van der Weg W., Mousseau N.
Fitting the Stillinger–Weber potential to amorphous silicon. *Journal of Non-crystalline Solids*, vol. 282, n° 2-3, 2001, p. 248–255, Elsevier.

[VIT 68] Vitek V.
Intrinsic stacking faults in body-centred cubic crystals. *Philosophical Magazine*, vol. 18, n° 154, 1968, p. 773–786, Taylor & Francis.

[WAC 54] Wachtman Jr J., Maxwell I.
Plastic Deformation of ceramic-Oxide Single Crystals. *Journal of the American Ceramic Society*, vol. 37, n° 7, 1954, p. 291–299, Wiley Online Library.

[WAC 60] Wachtman Jr J., Tefft W., Lam Jr D., Stinchfield R.
Elastic constants of synthetic single crystal corundum at room temperature. *Journal of Research of the National Bureau of Standards. Section A, Physics and Chemistry*, vol. 64, n° 3, 1960, Page 213, National Institute of Standards and Technology.

[WAD 95] Wadley H. N., Lu Y., Goldman J. A.
Ultrasonic determination of single crystal sapphire fiber modulus. *Journal of Nondestructive Evaluation*, vol. 14, n° 1, 1995, p. 31–38, Springer.

[WAD 11] Wada M., Matsudaira T., Kitaoka S.
Mutual grain-boundary transport of aluminum and oxygen in polycrystalline Al_2O_3 under oxygen potential gradients at high temperatures. *Journal of the Ceramic Society of Japan*, vol. 119, n° 1395, 2011, p. 832–839, The Ceramic Society of Japan.

[WAL 00] Walters C., McCarty K., Soares E., Van Hove M.
The surface structure of α-Al_2O_3 determined by low-energy electron diffraction: aluminum termination and evidence for anomolously large thermal vibrations. *Surface Science*, vol. 464, n° 2-3, 2000, p. L732–L738, Elsevier.

[WAN 00a] Wang X.-G., Chaka A., Scheffler M.
Effect of the Environment on α-Al_2O_3 (0001) Surface Structures. *Physical Review Letters*, vol. 84, n° 16, 2000, Page 3650, APS.

[WAN 00b] Wang Y., Jiang S., Wang M., Wang S., Xiao T. D., Strutt P. R.
Abrasive wear characteristics of plasma sprayed nanostructured alumina/titania coatings. *Wear*, vol. 237, n° 2, 2000, p. 176–185, Elsevier.

[WAN 02] Wang Y., Chen M., Zhou F., Ma E.
High tensile ductility in a nanostructured metal. *Nature*, vol. 419, n° 6910, 2002, p. 912–915, Nature Publishing Group.

[WAN 13a] Wang J., Sansoz F., Huang J., Liu Y., Sun S., Zhang Z., Mao S. X.
Near-ideal theoretical strength in gold nanowires containing angstrom scale twins. *Nature Communications*, vol. 4, n° 1, 2013, p. 1–8, Nature Publishing Group.

[WAN 13b] Wang S., He Y., Huang H., Zou J., Auchterlonie G. J., Hou L., Huang B.
An improved loop test for experimentally approaching the intrinsic strength of alumina nanoscale whiskers. *Nanotechnology*, vol. 24, n° 28, 2013, Page 285703, IOP Publishing.

[WAN 14] Wang Y., Santos A., Kaur G., Evdokiou A., Losic D.
Structurally engineered anodic alumina nanotubes as nano-carriers for delivery of anticancer therapeutics. *Biomaterials*, vol. 35, n° 21, 2014, p. 5517–5526, Elsevier.

[WAR 34] Warren B., Gingrich N.
Fourier integral analysis of X-ray powder patterns. *Physical Review*, vol. 46, n° 5, 1934, Page 368, APS.

[WEB 00] Webster T. J., Ergun C., Doremus R. H., Siegel R. W., Bizios R.
Enhanced functions of osteoblasts on nanophase ceramics. *Biomaterials*, vol. 21, n° 17, 2000, p. 1803–1810, Elsevier.

[WEI 12] Weinberger C. R., Cai W.
Plasticity of metal nanowires. *Journal of Materials Chemistry*, vol. 22, n° 8, 2012, p. 3277–3292, Royal Society of Chemistry.

[WOL 99] Wolf D., Keblinski P., Phillpot S., Eggebrecht J.
Exact method for the simulation of Coulombic systems by spherically truncated, pairwise r^{-1} summation. *The Journal of Chemical Physics*, vol. 110, n° 17, 1999, p. 8254–8282, American Institute of Physics.

[WU 10] Wu X., Wang R., Wang S.
Generalized-stacking-fault energy and surface properties for HCP metals: a first-principles study. *Applied Surface Science*, vol. 256, n° 11, 2010, p. 3409–3412, Elsevier.

[WU 19] Wu D., Cheng F., Yang F., Huang C.
Non-destructive testing for carbon-fiber-reinforced plastic (CFRP) using a novel eddy current probe. *Composites Part B: Engineering*, vol. 177, 2019, Page 107460, Elsevier.

[XIO 18] Xiong B., Chen L., Shi J.
Anion-containing noble-metal-free bifunctional electrocatalysts for overall water splitting. *ACS Catalysis*, vol. 8, n° 4, 2018, p. 3688–3707, ACS Publications.

[YAM 02] Yamakov V., Wolf D., Phillpot S. R., Mukherjee A. K., Gleiter H.
Dislocation processes in the deformation of nanocrystalline aluminium by molecular-dynamics simulation. *Nature Materials*, vol. 1, n° 1, 2002, p. 45–49, Nature Publishing Group.

[YAN 08] Yan Z. Z. G.
SPD Technology for Fabricating Bulk Nanocrystalline Materials. *Materials Review*, vol. 1, 2008.

[YAN 18] Yang S., Kim W., Cho M.
Molecular dynamics study on the coalescence kinetics and mechanical behavior of nanoporous structure formed by thermal sintering of Cu nanoparticles. *International Journal of Engineering Science*, vol. 123, 2018, p. 1–19, Elsevier.

[YIL 07] Yilmaz R., Kurt A. O., Demir A., Tatli Z.
Effects of TiO_2 on the mechanical properties of the Al_2O_3–TiO_2 plasma sprayed coating. *Journal of the European Ceramic Society*, vol. 27, n° 2-3, 2007, p. 1319–1323, Elsevier.

[YIN 05] Yin L., Huang H., Ramesh K., Huang T.
High speed versus conventional grinding in high removal rate machining of alumina and alumina–titania. *International Journal of Machine Tools and Manufacture*, vol. 45, n° 7-8, 2005, p. 897–907, Elsevier.

[YIN 17] Yin B., Wu Z., Curtin W.
Comprehensive first-principles study of stable stacking faults in hcp metals. *Acta Materialia*, vol. 123, 2017, p. 223–234, Elsevier.

[YU 10] Yu Q., Shan Z.-W., Li J., Huang X., Xiao L., Sun J., Ma E.
Strong crystal size effect on deformation twinning. *Nature*, vol. 463, n° 7279, 2010, p. 335–338, Nature Publishing Group.

[ZEN 16] Zeng X. M., Lai A., Gan C. L., Schuh C. A.
Crystal orientation dependence of the stress-induced martensitic transformation in zirconia-based shape memory ceramics. *Acta Materialia*, vol. 116, 2016, p. 124–135, Elsevier.

[ZHA 07] Zhang C., Kalia R. K., Nakano A., Vashishta P.
Hypervelocity impact induced deformation modes in α-alumina. *Applied Physics Letters*, vol. 91, n° 7, 2007, Page 071906, American Institute of Physics.

[ZHA 08] Zhang C., Kalia R. K., Nakano A., Vashishta P., Branicio P. S.
Deformation mechanisms and damage in α-alumina under hypervelocity impact loading. *Journal of Applied Physics*, vol. 103, n° 8, 2008, Page 083508, American Institute of Physics.

[ZHA 10] Zhang H., Chen X., Cao F., Wang G., Dong X., Hu Z., Du T.
Charge–discharge properties of an antiferroelectric ceramics capacitor under different electric fields. *Journal of the American Ceramic Society*, vol. 93, n° 12, 2010, p. 4015–4017, Wiley Online Library.

[ZHA 17] Zhang W., Gao Y., Xia Y., Bei H.
Indentation Schmid factor and incipient plasticity by nanoindentation pop-in tests in hexagonal close-packed single crystals. *Acta Materialia*, vol. 134, 2017, p. 53–65, Elsevier.

[ZHO 17] Zhou W., Long L., Xiao P., Li Y., Luo H., Yin R.-m. et al.
Silicon carbide nano-fibers in-situ grown on carbon fibers for enhanced microwave absorption properties. *Ceramics International*, vol. 43, n° 7, 2017, p. 5628–5634, Elsevier.

[ZHU 96] Zhu H.
Sintering processes of two nanoparticles: a study by molecular dynamics simulations. *Philosophical Magazine Letters*, vol. 73, n° 1, 1996, p. 27–33, Taylor & Francis.

[ZHU 18] Zhu Y., Peng L., Fang Z., Yan c., Zhang X., Yu G.
Structural engineering of 2D nanomaterials for energy storage and catalysis. *Advanced Materials*, vol. 30, n° 15, 2018, Page 1706347, Wiley Online Library.

[ZU 15] Zu Q., Guo Y.-F., Tang X.-Z.
Analysis on dissociation of pyramidal I dislocation in magnesium by generalized-stacking-fault energy. *Acta Metallurgica Sinica (English Letters)*, vol. 28, n° 7, 2015, p. 876–882, Springer.

FOLIO ADMINISTRATIF

THESE DE L'UNIVERSITE DE LYON OPEREE AU SEIN DE L'INSA LYON

NOM : Xu DATE de SOUTENANCE : le 14 Décembre 2021

Prénoms : Qinqin

TITRE : Dislocations and nanomechanics in Alumina using atomistic simulations

NATURE : Doctorat Numéro d'ordre : 2021LYSEI091

École doctorale : ED 34 Matériaux de Lyon

Spécialité : Science des Matériaux

RÉSUMÉ :Les nano-objets sont particulièrement intéressants pour leurs excellentes propriétés mécaniques. Alors que les nanocristaux métalliques sont généralement caractérisés par unelimite d'élasticité accrue, une contrainte à la rupture augmentée tout comme par un accroissement global de leur ductilité en compression, très peu de choses sont connues pourles autres classes de matériaux comme les nanocristaux céramiques. Il a récemment étémontré que des nanoparticules d'oxides de magnesium et d'aluminium pouvaient être dé-formées plastiquement à forte contrainte sans signe de rupture ce qui pourrait avoir desimplications importantes dans le domaine de l'élaboration des matériaux céramiques (no-tamment lors de leur compaction). Néanmoins, les mécanismes de déformation ont ététrès peu caractérisés dans ces nanoparticules, notamment dans le cas des nanocristauxd'Al_2O_3.
Dans cette étude, nous proposons d'étudier les propriétés mécaniques et les mécanismesde déformation de nanoparticules d'alumineαpar dynamique moléculaire. Tout d'abord, plusieurs propriétés du matériau massif sont calculées, étudiées et comparées à la littérature existante. Entre autres, les paramètres de maille, constantes élastiques, énergies defaute d'empilement et de surface ainsi que les caractéristiques de la dislocation coin dansle système de glissement basal sont simulées afin d'étuder la transférabilité de plusieursformalismes de potentiels interatomiques. Parmi les potentiels testés, le potentiel à troiscorps de Vashishta a montré les meilleures aptitudes pour les applications visées dans lasuite de l'étude. Ensuite, nous avons simulé en dynamique moléculaire des tests de compression sur des nanoparticules d'alumine en fonction de l'orientation de la sollication et dela température. Une analyse détaillée du comportement mécanique et des mécanismes dedéformation a été réalisée pour plusieurs tailles de nanoparticules. Les résultats sont discutés au regard d'expériences de nanomécaniques récentes et de travaux pionniers réalisés dans l'alumine massive.

MOTS-CLÉS : Alumine, dynamique moléculaire, mécanismes, compression

Laboratoire (s) de recherche :MATEIS – UMR CNRS 5510

Directeur de thèse : Jerome Chevalier INSA Lyon
Jonathan Amodeo INSA Lyon

Composition du jury :
Rapporteur : Laurent Pizzagalli, Univ. Poitiers
Rapporteur : Philippe Carrez, Univ. Lille
Examinateur : Karine Masenelli-Varlot, INSA-Lyon
Examinateur : Marie-Ingrid Richard, CEA Grenoble
Invité : Tristan Albaret, Univ. Lyon